Title
Optimizing Porous Materials for Electrochemical Applications

Author
Olivera, Edgar

Publication Date
2023

Peer reviewed|Thesis/dissertation

UNIVERSITY OF CALIFORNIA

Los Angeles

Optimizing Porous Materials for Electrochemical Applications

A dissertation submitted in partial satisfaction of the requirements for the degree of Doctor of Philosophy in Materials Science and Engineering

by

Edgar Olivera

2023

ABSTRACT OF THE DISSERTATION

Optimizing Porous Materials for Electrochemical Applications

by

Edgar Olivera

Doctor of Philosophy in Materials Science and Engineering

University of California, Los Angeles, 2023

Professor Sarah H. Tolbert, Chair

With the continued demand for sustainable alternative energy fuels to replace limited fossil fuels, it is essential to explore new material properties to attain a zero-carbon emission economy. Porous metallic materials possess attractive properties for electrochemical storage and energy conversion such as superior surface area, high conductivity and large open volume, facilitating the mass transport of guest molecules.

Among the different electrochemical energy storage applications, lithium metal batteries have been a competitive candidate for the next-generation of batteries. Despite its popularity, stability issues of lithium metal anode in the liquid electrolyte and the formation of lithium whiskers have kept it from practical use. Furthermore, finding scalable catalyst materials to electrochemically reduce carbon dioxide (CO_2R) to multi-carbon products such as ethylene and ethanol is key for a promising pathway to a carbon-neutral economy.

The objective of this thesis is to utilize porous metallic copper for electrochemical applications including (1) macroporous Cu as current collectors for Li metal batteries and (2) mesoporous Cu as a catalyst for higher-reduced products for CO_2 reduction.

The first part of this thesis proposes three-dimensional (3D) macroporous Cu current collectors as an effective method to mitigate whisker growth during the Li deposition process in a lithium metal battery (LMB). Three key parameters of the 3D current collectors, namely, the surface area, the tortuosity factor, and the surface chemistry are quantitatively studied to optimize the performance of these current collectors for LMB applications. Four types of porous copper networks with different sizes of well-structured microchannels are synthesized and electrochemically tested. It is found that a moderate surface area that can lower the current density of Li deposition while minimizing the formation of SEI is ideal to suppress lithium whisker growth and optimize performance. Furthermore, tortuosity should be kept at minimum in order to facilitate Li diffusion and lead to a more uniform Li morphology. In considering these parameters, it was determined that the 20Arc Cu sample (~14um average pore size) with a balance of moderate surface area and reasonable pore size had the best performance of all Cu samples tested. Lastly, a lithiophilic Zn layer is coated on the best and worst performing current collectors (~14μm and ~30μm average pore sizes, respectively). It is shown that Zn coating can improve the Li morphology and the coulombic efficiency from 99.16% to 99.56% for a low surface area 3D current collector.

Chapter 3 is a follow-up study of Chapter 2 with a focus on strategies to increase the lifetime cycling of the current collectors via asymmetric lithiophilic Ag coating. For this purpose, 3D porous Cu frameworks of 10 μm (30-Cu) and 14 μm (20-Cu) average pore sizes were used. Unfortunately, Li deposition on these structures is generally top-favored, increasing the chances for dendrite formation. To overcome this issue, a lithiophilic Ag coating with gradient composition, gradually decreasing from the bottom to the top of the framework, was utilized on these 3D Cu structures to favor Li deposition at the bottom of the porous network. By comparing the coulombic efficiency (CE), stability, and lifetime of these asymmetrically against both uncoated and symmetrically coated samples, it was found that the lifetime and CE of the current collectors can be increased. Particularly, the 20-Cu sample improved its lifetime by 30% and 10% at $2mA/cm^2$ ($10mAh/cm^2$) and $4mA/cm^2$ ($10mAh/cm^2$) current rates, respectively.

This was corroborated with post-cycling SEM images that showed a more 'bottom-favored' deposition and denser Li morphology on the asymmetrically coated samples.

The last part of the thesis focuses on the development of scalable mesoporous Cu catalyst materials to electrochemically reduce carbon dioxide (CO_2R) to multi-carbon products such as ethylene and ethanol. This work utilizes a scalable method of making powdered mesoporous Cu samples with dilute amounts of Al via dealloying of Cu-Al alloys with different compositions (10-22 at. % Cu). Dealloying produced mesoporous-macroporous Cu powdered structures with composition-dependent microstructure. These samples were electrochemically tested as catalysts for CO_2 reduction in a membrane electrode assembly. Tuning the catalyst pore size distribution increased overall CO_2R current density and C_{2+} selectivities. Tandem catalytic enhancement was also observed through dilute amounts of secondary metal coating, with the presence of a silver coating increasing C_{2+} reaction rates by up to 23.3%, and combined ethylene/ethanol production by up to 14.8% at a 500mV lower potential.

Through the results in this work, we hope to contribute to the strategies for design and optimization of porous materials for current collectors in lithium metal batteries as well as the importance of synergistic optimization of catalyst pore architecture and chemical composition in CO_2R catalyst design to enhance the production valuable products.

This dissertation of Edgar Olivera in approved.

Jane Chang

Xiangfeng Duan

Bruce Dunn

Sarah H. Tolbert, Committee Chair

University of California, Los Angeles, 2023

To my beloved family and friends, especially my mother, Luzmila Huete, and father, Fausto Olivera, as well as my brother, Diego Olivera, and uncle, Serafin Huete, who have always been there to support me

TABLE OF CONTENTS

LIST OF FIGURES

Chapter 2: Quantitatively Designing Porous Copper Current Collectors for Lithium Metal Anodes

Chapter 3: Increasing the lifetime of thick porous Cu current collectors for Lithium Metal Batteries via asymmetric lithiophilic coating

ACKNOWLEDGEMENTS

These past few years as a PhD student have been challenging and rewarding. I was fortunate enough to have a great research group like the Tolbert Group where I found constant academic and emotional support from my grad student colleagues and especially from my PhD advisor, Prof. Sarah Tolbert. I am fondly appreciative of the opportunity Prof. Tolbert gave me to be part of her group and the flexibility she gave me to explore different research areas and satisfy my insatiable curiosity. I also want to express my gratitude to my committee members including Prof. Bruce Dunn, Prof. Xiangfeng Duan, Prof. Jane Chang and Prof. Chong Liu (who was part of my qualifying exam) for their time and advise given towards the completion of this work.

Within our group, I want to thank Dr. Andrew Dawson and Charlene Salamat, for the fruitful discussions as well as the XPS characterization. I also would like to acknowledge the indispensable assistance of Spencer Hamilton and Dr. Lisa Pangilinan (from the Kaner Group) in the metal alloy synthesis using the arc melting technique. Furthermore, I am thankful for my collaborators within UCLA including my good friend Shiqi Zheng, Narayanan Murali and their advisor Prof. Xiaochun Li for the discussions on metal synthesis, letting me use their machining and polishing equipment and their assistance in making metal alloys using their furnace equipment. Lastly, I am appreciative of Patricia McNeil from the Dunn group who helped me take the last few sets of N_2 porosimetry measurements to complete the project in Chapter 4. Outside of UCLA, I had two key collaborators, Bingyu Lu from the Meng group at UC San Diego who worked with me on Chapter 2 and 3 of my thesis and Kabir Abiose from the Jaramillo group at Stanford University who was essential in the completion of Chapter 4.

I would like to acknowledge the different collaborators involved in the work presented in this thesis:

Chapter 2 is the published work of Bingyu Lu, Edgar Olivera, Jonathan Scharf, Mehdi Chouchane, Chengcheng Fang, Miguel Ceja, Lisa Pangilinan, Shiqi Zheng, Andrew Dawson, Diyi Cheng, Wurigumula Bao, Oier Arcelus, Alejandro A. Franco, Xiaochun Li and Sarah H. Tolbert and Ying Shirley Meng's manuscript entitled "Quantitatively Designing Porous Copper Current Collectors for Lithium Metal Anodes."

Bingyu and myself are the lead authors of this work and we both contributed equally. Bingyu led the electrochemical and post-electrochemical characterization, while I carried out the materials synthesis, electrochemical coating and characterization. Additionally, a group of researchers from UC San Diego including Jonathan Scharf, Mehdi Chouchane, Miguel Ceja, Diyi Cheng, Wurigumula Bao, Oier Arcelus and Alejandro A. Franco contributed in the simulations and the micro-CT analysis. Shiqi Zheng's help in the furnace melting of metals and Lisa Pangilinan's assistance in the arc melting synthesis of metals were invaluable in the materials synthesis process.

Chapter 3 is an unpublished work entitled "Increasing the lifetime of thick porous Cu current collectors for Lithium Metal Batteries via asymmetric lithiophilic coating." Dr. Lisa Pangilinan and Spencer Hamilton helped to make the metals used via the arc melting technique. Bingyu Lu assisted in the preparation of the electrolyte used keeping it with at a high level of purity. Additionally, Dr. Andrew Dawson took the XPS measurements.

Chapter 4 entitled "Mesoporous, Dealloyed Copper Catalysts for the Electrochemical Reduction of Carbon Dioxide" is the result of a collaborative work with the Jaramillo group at Stanford University. Kabir Abiose and myself contributed equally to this work. Kabir worked on the electrochemical tests and post-electrochemical characterization. I worked on the materials design and synthesis as well as the characterization of samples. Charlene Salamat took the XPS data and analysis. Finally, Patricia McNeil partially helped with the N_2 porosimetry measurements.

The research in this dissertation was guided by Prof. Sarah Tolbert. My work was funded by the Eugene V. Cota-Robles Fellowship.

VITA

Honors and Awards

Nov. 2009: Robotics Regional VEX Competition (1st place)

Sep. 2009: AP Scholar with Distinction

Jun. 2009: Rube Goldberg Contest (1st place)

Aug. 2012: International Institute for Nanotechnology Certificate

Sept. 2012-Sept 2018: Hispanic Scholarship Fund Award

Jun. 2013: Qualcom Award Recipient

Sept. 2014: 2nd Best Poster chosen by Audience at BERC EXPO

Sep. 2016-Sept 2020: Cota-Robles Fellowship Awardee

Publications

[1] B. Lu*, **E. Olivera*,** et al. Quantitatively Designing Porous Copper Current Collectors for Lithium Metal Anodes. ACS Appl. Energy Mater. 2021, 4, 6454-6465

[2] M. Jacobs, X. Zhou, **E. Olivera**, et al. Room temperature rectification in tapered-channel thermal diodes through nanoscale confinement-induced liquid-solid phase change. Journal of Applied Physics 129, 075103 (2021)

[3] P. Srivastava, K. Jiang, Y. Cui, **E. Olivera**, et al. The influence of nano/micro sample size on the strain-rate sensitivity of plastic flow in tungsten. International Journal of Plasticity 136, 102854 (2021)

[4] A.M. Ruminski, F. Yang, E. Cho, J. Silber**, E. Olivera**, et al. Geometric analysis of enhanced thermal conductivity in epoxy composites: A comparison of graphite and carbon nanofiber fillers. Phys. Status Solidi A, 214,No. 1, 1600368 (2017)

Chapter 1: Introduction

The need for alternative renewable and sustainable energy fuels has accelerated the search for new materials with useful properties for the fields of energy storage and conversion.[1,2] Porous metallic materials have unique properties for electrochemical applications[3] such as high surface area, open volume for guest molecules and high electrical conductivity for charge transfer mechanisms. Porous materials can be classified according to their pore sizes:[4] microporous (< 2nm), mesoporous (2-50nm) or macroporous (>50nm). Depending on their pore size structure, porous materials can be utilized for specific energy applications including, but not limited, to current collectors for batteries and catalysts of electrochemical reactions. This work, in particular, focuses on the utilization (1) of macroporous Cu as current collectors in lithium metal batteries and (2) of mesoporous Cu as catalysts for CO_2 reduction reaction.

Unlike, lithium-ion battery with their traditional graphite anodes, lithium metal batteries use lithium metal as its anode material.[5] Lithium metal possesses a high theoretical capacity (3,860 mAh/g) but the growth of lithium whiskers and the issues in electrolyte stability keep it from becoming a commercialize.[6] Macroporous metallic materials[7] are ideal to regulate the formation of dendrites as it has a high surface area to decrease the current density of deposition and a more open volume to accommodate lithium depositions compared to 2D current collectors. However, the three key parameters for the optimization of a current collector[8] such as surface area, tortuosity and surface chemistry[9] have not been extensively studied. The first part of this work quantitatively studies the surface area and the tortuosity. This is followed by a work that focuses on strategic methods to modify the surface chemistry to better accommodate lithium inside the open volume of thick current collectors via lithiophilic coating.

Decreasing the Cu pore size to the mesoporous scale (2-50nm), further increases the surface area.[10] The higher surface area can be useful in increasing the catalytic sites of a catalyst used for CO_2 reduction. Furthermore, by increasing the number of small grain boundaries and the lattice defect density at the mesoscale, these porous materials further the production of higher-reduced products (C_{2+}). Lastly, changing the surface chemistry with the addition of a second metallic coating can create a “tandem” effect” and increase the selectivity towards one product.[11] The last part of this work quantitatively studies the CO_2 reduction products in three dealloyed

mesoporous Cu with varying surface area derived from Cu-Al alloys. The effects of changing the surface chemistry of these samples by coating them with Ag or Au are also explored.

We hope to contribute to the strategies to further optimize the performance of the Cu current collectors and scalable Cu catalysts for CO2 reduction and lay the grounds for a more sustainable future.

1.1. References

(1) Schäppi, R., Rutz, D., Dähler, F. *et al.* Drop-in fuels from sunlight and air. *Nature* **601**, 63–68 (2022).
(2) Gao, L., Bryan, B. Finding pathways to national-scale land-sector sustainability. *Nature* **544**, 217–222 (2017).
(3) Du, C.; Li, P. Zhuang, Z. Fang, Z.; He, S.; Feng, L.; Chen, W. Highly porous nanostructures: Rational fabrication and promising application in energy electrocatalysis, Coordination Chemistry Reviews 466 (2022) 214604
(4) Yang, X.; Chen, L.; Li, Y.; Rooke, J. C.; Sanchez, C.; Su, B. Hierarchically porous materials: synthesis strategies and structure design. Chem. Soc. Rev., 2017, 46, 481—558
(5) Cheng, X.; Zhang, R.; Zhao, C.; Zhang, Q. Toward Safe Lithium Metal Anode in Rechargeable Batteries: A Review. Chem. Rev. 2017, 117, 10403−10473
(6) Liu, B.; Zhang, J.; Xu, W. Advancing Lithium Metal Batteries. Joule 2, 833–845, May 16, 2018
(7) Yue, Y.; Ling, H. 3D Current Collectors for Lithium-Ion Batteries: A Topical Review. Small Methods. 2018, 2, 1800056
(8) Lamiel, C.; Hussain, I.; Ma, X.; Zhang, M. Properties, functions, and challenges: current collectors. Materials Today Chemistry 26 (2022) 101152
(9) Cha, E.; Yun, J. H.; Ponraj, R.; Kim, D. K. A mechanistic review of lithiophilic materials: resolving lithium dendrites and advancing lithium metal-based batteries. Mater. Chem. Front., 2021, 5, 6294–6314
(10) Fadillah, G.; Saleh, T. A. Advances in mesoporous material for adsorption and photoconversion of CO2 in environmental pollution: Clean environment and clean energy Sustainable Chemistry and Pharmacy 29 (2022) 100812
(11) Jia, Y.; Li, F.; Fan, K.; Sun, L. Cu-based bimetallic electrocatalysts for CO2 reduction. Advanced Powder Materials 1 (2022) 100012

Chapter 2: Quantitatively Designing Porous Copper Current Collectors for Lithium Metal Anodes

2.1 Introduction

With a high theoretical capacity (3,860 mAh/g, or 2,061 mAh/cm^3) and low electrochemical potential (–3.04 V versus the standard hydrogen electrode), lithium metal is considered as the ideal candidate for the next generation battery anodes.[1] In fact, the lithium metal anode is a key component of next-generation high-energy-density battery systems such as lithium-sulfur and lithium-oxygen batteries.[2] However, there are many obstacles that need to be solved before lithium metal anodes can be effectively used in commercial cells. The fundamental problem lies in the formation of lithium whiskers during plating, which eventually leads to the formation of inactive lithium after cycling.[3] As a result, the lithium metal anode suffers from low CE and low cyclability.

Numerous methods have been proposed to mitigate the lithium whisker formation issue and improve the cyclability of lithium metal anode. One of the most promising methods to achieve this is through the engineering of the electrolyte,[4] such as adding additives,[5–7] using high lithium salt concentration[8–10] and localizing high lithium-salt concentration.[11–13] The main working principle of a high-performance electrolyte is to construct a homogeneous SEI layer and to provide a uniform lithium ion flux during the plating process so that a smooth and dense morphology can be achieved.[14] Another emerging method is the engineering of current collectors. The current collectors play a crucial role in the performance of a lithium metal battery cell. Planar Cu foils have been used as the anode current collector for decades because of their electrochemical stability against lithium.[15] However, under practical current densities, due to the inhomogeneous lithium-ion flux, lithium whiskers can easily form on the planar Cu foils during cycling.[16] Therefore, a new current collector that can regulate the local current density and provide a uniform lithium ion flux is desired for lithium metal anodes.[15, 17,18] A variety of 3D current collectors have been designed to achieve this purpose.[19–27]

For a high-performance 3D current collector, there are three key parameters that need to be carefully designed: surface area, tortuosity factor and surface chemistry.[28] However, these three parameters are correlated with each other, and often one cannot be altered without disrupting the other two. Several works have mentioned the effects of these key parameters on the performance of the 3D current collectors.[29, 30] Yun *et al.* discovered that by tuning the dealloying time of brass foil, the resulting copper foil would have different pore sizes and surface areas, which would eventually lead to different performance of the dealloyed copper foils.[29] Similarly, by tuning the Cu pillar size and spacing, Chen *et al.* were able to study the effects of surface area and pillar spacing on the CE of the Cu pillar current collector and found the best combination for the performance.[30] Therefore, there is no doubt that surface area, tortuosity factor, and surface chemistry play crucial roles in determining the performance of the 3D current collectors. However, quantitative analysis of these key parameters is required when designing a new 3D current collector system.

In the present work, 3D porous Cu current collectors were fabricated by etching Fe from Cu-Fe composites with different compositions. The physical properties of current collectors were then quantified using laboratory micro-CT,[31,32] and their performance was predicted in terms of surface areas, tortuosity factors and surface chemistry. The quantitative study suggested that the high surface area was not as beneficial as previously believed[33, 34] and that the tortuosity factor should always be kept at a minimum. The high performance can only be achieved in a system when the three key parameters are in its optimal range. The prediction of the performance was also validated by Titration Gas Chromatography (TGC)[35] and electrochemical testing.

2.2 Experimental

1) Synthesis of the porous copper networks

Pure Cu powders (Fisher Scientific, electrolytic powder) and pure Fe powder (Beantown Chemical, -325 mesh, reduced, 98%) were used to prepare Cu-Fe precursor ingots with three different compositions**:** 10 atomic percent (at%) Cu-90at%Fe, 20at%Cu-80at%Fe, and 30at%Cu-70at%Fe. The average powder size of both powders was about 30 microns. A hydraulic press was used to make pellets of 1 cm in diameter for each composition. These pellets were then arc melted five times to make homogeneous ingots with high cooling rates. In addition, the 30at%Cu-70at%Fe was loaded in a 3cm-diameter alumina crucible and heated in an Ar-filled furnace at 1550 ˚C for 1 hour, followed by slow cooling down to room temperature. The four different types of samples were sliced and polished using sandpaper to make samples 1 cm in diameter and 200 microns in thickness. These four samples are denoted throughout this paper as 10Arc, 20Arc, 30Arc and 30Furnace, in accordance with their composition and synthesis method.

After the Cu-Fe ingots were successfully synthesized, the disk was then etched in 5wt% H_2SO_4 acid solution at 90˚C under constant stirring for 24 hours. The acid solution was changed every 8 hours to prevent the accumulation of contaminants. The etched sample was then cleaned in 5wt% HCl solution under sonication for 15 minutes. This was followed by an acetone wash under sonication for 15minute to wash away any leftover contaminants. Finally, the cleaned samples were dried under vacuum for one hour.

2) Zn Electrodeposition

The 20Arc Cu sample was Zn-coated using an electrolyte of 0.05 M $ZnSO_4$ +0.3M H_3BO_3 and the 30Furnace Cu sample was Zn-coated using an electrolyte of 0.01 M $ZnSO_4$ +0.3M H_3BO_3. In both cases, a small amount of 1M H_2SO_4 was added to adjust the pH to 1-2. The cleaned porous Cu was removed from the glovebox and used as the working electrode in a three-electrode set up where the counter electrode was platinum foil and the reference electrode was Ag/AgCl in KCl. A current density of 1mA/cm^2 was used to deposit Zn for 10 min and 5 min for the 30Furnace and 20Arc, respectively. The area used for the deposition current density was the measured effective surface area. The sample was then washed with deionized water and acetone and then dried under vacuum for one hour.

3) Electrochemistry

CR2016-type coin cells were assembled in an Ar-filled glove box for electrochemical characterization. The electrolyte consisted of 75 µL of 1 M lithium bis(trifluoromethane sulfonyl)imide (LiTFSI) in a mixed solvent of 1,3-dioxolane (DOL) and 1,2-dimethoxyethane (DME) (1:1 in volume) with 2% $LiNO_3$ and Li metal foil was used as the counter electrode. A range of current density was used during lithium plating morphology study. For all CE testing, at least three cells were tested at the same condition and the average CE is calculated.

4) Scanning Electron Microscope / Energy Dispersive X-ray Spectroscopy

A FEI Apreo Scanning Electron Microscope (SEM) was used to study the structure of the as-prepared porous copper current collector as well as the morphology of the electrochemically deposited lithium (EDLi). Energy Dispersive X-ray Spectroscopy (EDS) was used to characterize the elemental composition of the sample.

5) Micro-CT

The samples were individually punched into films with a 2 mm radius piece and were stacked in a PTFE cylindrical tube with alternating PTFE films to provide separation. Two scans were conducted using a ZEISS Xradia 510 Versa micro-CT instrument. The first scan was conducted on the lager pore samples (30Furnance and 10Arc, shown in Fig 1c-d) and had a voxel size of 1.07 µm and an exposure of 4 seconds. The second scan was used to examine the smaller pore samples (20Arc and 30Arc, shown in Fig 1a-b) and had a voxel size of .7834 µm and an exposure of 6 seconds. Both scans were conducted with 1801 projections at an X-ray energy of 140 keV with a 71.3 uA current using a high energy filter at a 4X magnification. The beam hardening constant for the reconstruction was 0 and 0.6 for the first and second scan respectively. Post measurement analysis was performed by the Amira-Avizo method using the Deblur, Delineate, and Median Filter modules for data sharpening and filtration provided by the software. The Separate Objects module, which utilizes a distance map and a watershed algorithm, was used to define 3D pores and determine the overall distribution of the pore sizes. The tortuosity factor was determined for each of the resulting structures using the software TauFactor[36] and cross-validated with GeoDict, both relying on Fickian diffusion.

Simulation of the Li deposition process in the porous copper made use of an *in house* MATLAB-based stochastic algorithm. For a given capacity, the volume of deposited Li was determined considering 100 % coulombic efficiency and a molar volume of 13.02×10^{-6} m^3/mol. Then, this volume was converted into a number of pixels. Subsequently, pixels of void in contact with solid phase (Cu or Li) were converted into pixels of Li until the desired amount was achieved. To mimic the experimental observations, a percentage of the Li was deposited on the top of the copper support (see Table S1). We arbitrarily allowed for an extra 15 µm thick void to be inserted on top of the current collector for Li deposition. After Li deposition, the remaining empty thickness was removed from this extra 15 µm space in order to limit its impact on the tortuosity factor calculation. Additionally, to account for the heterogeneous deposition of Li along the thickness, an arbitrary gradient has been applied to replicate the experimental observations. Each structure was divided into 6 equal sub-volumes for which the deposited Li

amount is reported in Table S2. Then the algorithm called the software TauFactor[36] to determine the tortuosity factors of each porous copper network. Each condition was repeated between 5 and 10 times to quantify the uncertainty linked to the stochastic method.

6) Titration Gas Chromatography (TGC)

The TGC method was used to quantify the amount of inactive metallic lithium formed in the porous copper after cycling. After plating and stripping of Li, the porous Cu electrode was recovered from the coin cell; the porous copper film, including any residual inactive lithium, together with the separator, was put into a 30 mL bottle without washing. The bottle was then sealed with a rubber stopper and the internal pressure of the bottle was adjusted to 1 atm. After the bottle was removed from the glovebox, excess deionized (DI) water (0.5 mL) was injected into the bottle to react with any residual inactive metallic lithium to form H_2 gas. The vial was then well mixed by shaking, and a gas-tight syringe was used to quickly take 30 µL of the gas from the head-space of the sealed bottle. The gas was then injected into a Nexis GC-2030 Gas Chromatograph (Shimadzu) for H_2 quantification. A pre-established H_2 calibration curve was used to calculate the amount of inactive metallic lithium from the measured H_2 peak area. The mass of inactive metallic lithium in the porous copper films was directly related to the amount of H_2.

7) X-Ray Diffraction (XRD)

XRD was performed using a PANalytical X'Pert Pro powder diffractometer operating with Cu Kα radiation (λ = 1.5418 Å) using a 0.03° step size, a voltage of 45 kV, and a current of 40 mA. XRD patterns were recorded in the range of $15° < 2\theta < 85°$.

8) X-Ray Photo-electron Spectroscopy (XPS)

XPS analysis was performed using a Kratos Axis Ultra DLD spectrometer with a monochromatic Al (Kα) radiation source. A charge neutralizer filament was used to control charging of the sample. A 20 eV pass energy was used with a 0.1 eV step size; scans were calibrated using adventitious carbon by setting the C 1s peak to 284.8 eV. Samples were etched with an Ar beam with a raster size of 2mm x 2mm at an energy of 4 kV for 1 minute.

2.3 Result and Discussion

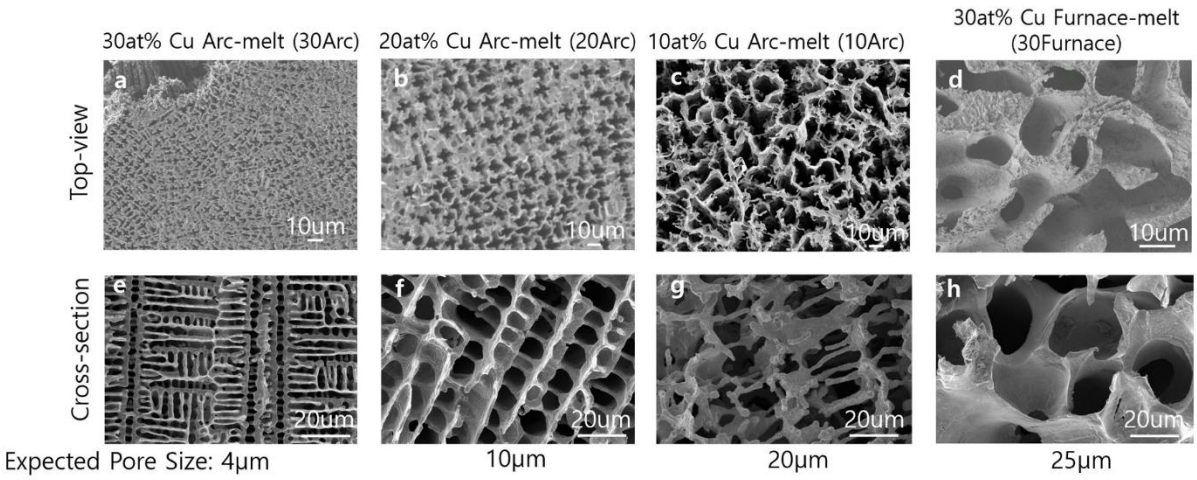

Figure 2.1. SEM images of the four porous copper films used in this work. a) Top-view and e) cross-section of the 30 at% Cu arc-melted (30Arc) sample; b) top-view and f) cross-section of the 20 at% Cu arc-melted (20Arc) sample; c) top-view and g) cross-section of the 10 at% Cu arc-melted (10Arc) sample; d) top-view and h) cross-section of the 30 at% Cu furnace-melted (30Furnace) sample.

Porous copper films with interconnected channels were fabricated by etching Fe from Cu-Fe composites. Ingots with compositions of 10, 20 and 30 atomic percentage (at%) Cu were made by arc melting and one ingot with a composition of 30 at% Cu was made using a conventional Ar-filled furnace. Arc melting involves rapid heating and rapid cooling, while heating and cooling rates in a conventional furnace are much longer. Because Cu and Fe are essentially immiscible in the solid state but fully miscible in the melt, the size of the phase separated domains that form upon solidification is strongly dependent on the cooling rate, with faster cooling of the arc furnace producing smaller domains. The XRD patterns of the as-made ingots are shown in the SI in Figure S1 and are in agreement with a phase separated mixture of Cu and Fe. For a given cooling rate, the size of domains can be further tuned using the atomic percentage of Cu and Fe with higher Fe fractions resulting in large Fe domains. Because the Fe is the fraction that is etched form the ingot, both larger Fe fractions and slower cooling rates result in larger pore in the remaining Cu. After careful etching and cleaning, porous coppers with different well-structured channels were fabricated. (Fig. 1). As observed in the XRD patterns of the post-etching samples (Fig. S2), the porous copper samples obtained from arc-melted ingots are (200) oriented and the porous copper materials made using a conventional furnace are polycrystalline. Furthermore, the XPS data for all four samples (Fig. S3-S6) show that the samples are mainly composed of Cu and some remaining copper oxide on the surface. However, there is no Fe or S remaining in the samples. Unlike other randomly structured porous copper that were also synthesized by dealloying method,[29] the porous copper networks derived from Cu-Fe composites show homogeneous, large pored micro-structures that allow us to quantitatively analyze the effects of key parameters such as surface area and tortuosity factor on the performance of a 3D current collector.

As shown in Fig. 1a and 1e, when 30 at% Cu was mixed with Fe and arc with rapid heating and cooling, the resulting porous copper had roughly 4μm-wide and 10μm-long channels, which provided empty spaces for lithium to deposit. As the Cu at% decreased in the precursor, the channels in the final porous Cu grew longer and wider. The 10 at% Arc melt porous copper showed approximately 20μm-wide channels (Fig. 1c, 1g), but the structure of the channels was very fragile. Therefore, a second melting technique was used when synthesizing the 25μm-wide porous copper, which involved slow heating and cooling an ingot with 30 at% Cu using an Ar-filled furnace. The resulting porous copper showed 25μm-wide pores with sturdy ligaments.

The physical parameters of the porous copper samples were quantified by laboratory X-ray micro-CT. Each piece of the porous copper was punched and fitted into a sample holder tube. With voxel size of 0.7834 μm or 1.07 μm, the 3D structures (Fig. 2a, 2b) of the porous coppers obtained through the tomography was analyzed using the Amira-Avizo software package and the physical properties of the porous coppers were measured (Fig. 2).

Fig. 2d reports the pore size distribution of each porous copper sample. As expected, the 30Furnace sample shows the largest pores and the 30Arc sample had the smallest pores, followed by 20Arc and 10Arc. The peak of each histogram curve represents the average length of the micro-channels in the porous copper. The results match well with the SEM images shown in Fig. 1 except for the 30Arc sample. For the 30Arc samples, the pores are in a narrow but long channel-like structure. The expected pore size measured from the SEM images is around 4 um. However, in the MicroCT measurement, the pore size is defined as the diagonal length of the pores, so the both the diameter and the length of the channel-like pores are included in the pore size calculation (Figure S7). Therefore, in the Fig 2d, the pore size of 30Arc centers around 10 um instead of 4 um. The geometric tortuosity values in Fig. 2e were calculated based on the average length a fictive particle needs to travel to go through the whole porous copper sample in the z-direction, which approximately quantifies how easy it is for a lithium ion to diffuse and electro-migrate inside the Cu network during an electrochemical plating process. Both the 10Arc and 30Furnace samples have relatively low geometric tortuosity because they have large enough pores for lithium ion to move freely without many obstacles in the z-direction. The volumetric surface area of each porous network can be directly obtained from the 3D tomography (Fig. 2c). The effective surface area was calculated based on the actual size of the electrode used in the electrochemical testing (7 mm in diameter and 200 μm in thickness). In the surface area measurement, the same trend is observed as in the geometric tortuosity: the samples with smallest pore sizes have the largest effective surface area while the larger pores give the smallest surface areas. There is a slow drop of effective surface area from the 20Arc to 10Arc materials, despite the fact that the pore size difference in these two samples is large. This is caused by the change of ligament size as the at% of Cu in the precursor ingot decreases from 20 to 10 (Fig. 1f, 1g). The thinner ligament contributes to the extra surface area in the 10Arc sample. With these key physical parameters quantified, the effects of morphology and the distribution of deposited Li can now be studied in detail.

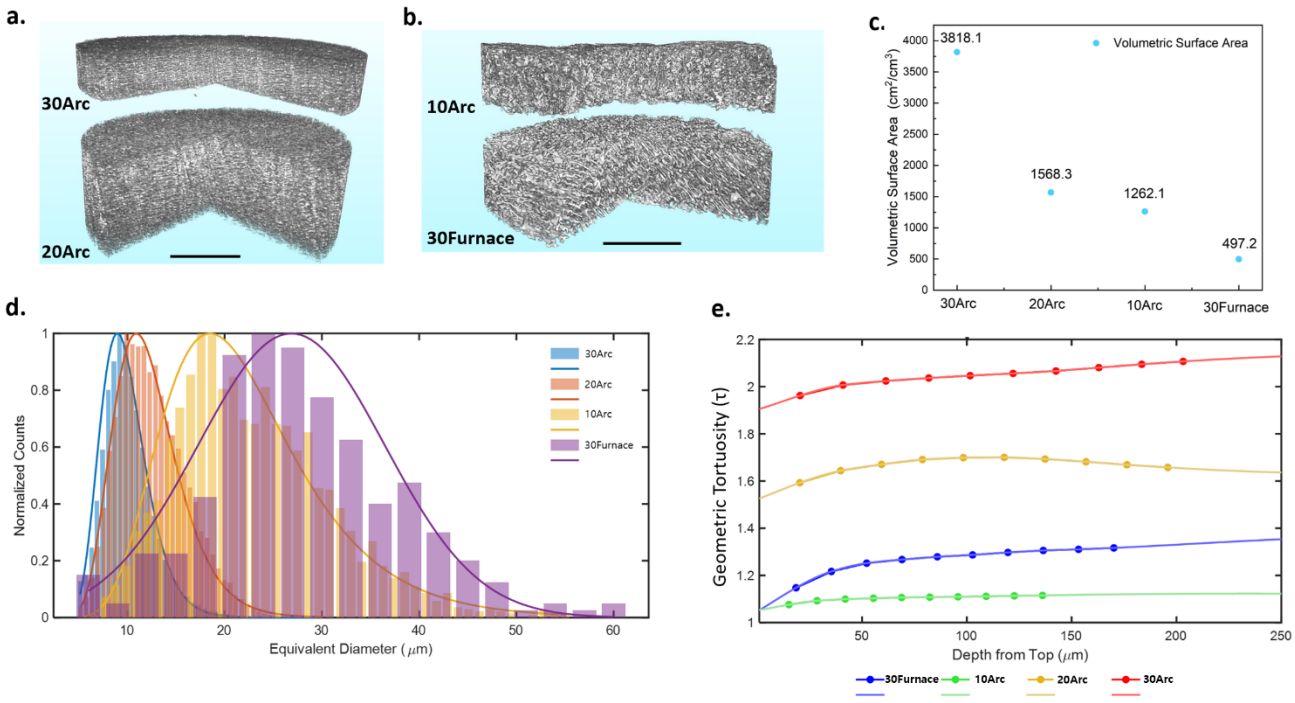

Figure 2.2. a) The 3D tomography of 30Arc and 20Arc with voxel size of 0.7834 µm. b) The 3D tomography of 10Arc and 30Furnace with voxel of 1.07 µm. For both parts a) and b), the scale bar is 200 µm. c) Volumetric surface area in the porous copper; d) Histograms of the pore size distribution for each porous copper sample. e) Geometric tortuosity of the porous copper as a function of depth.

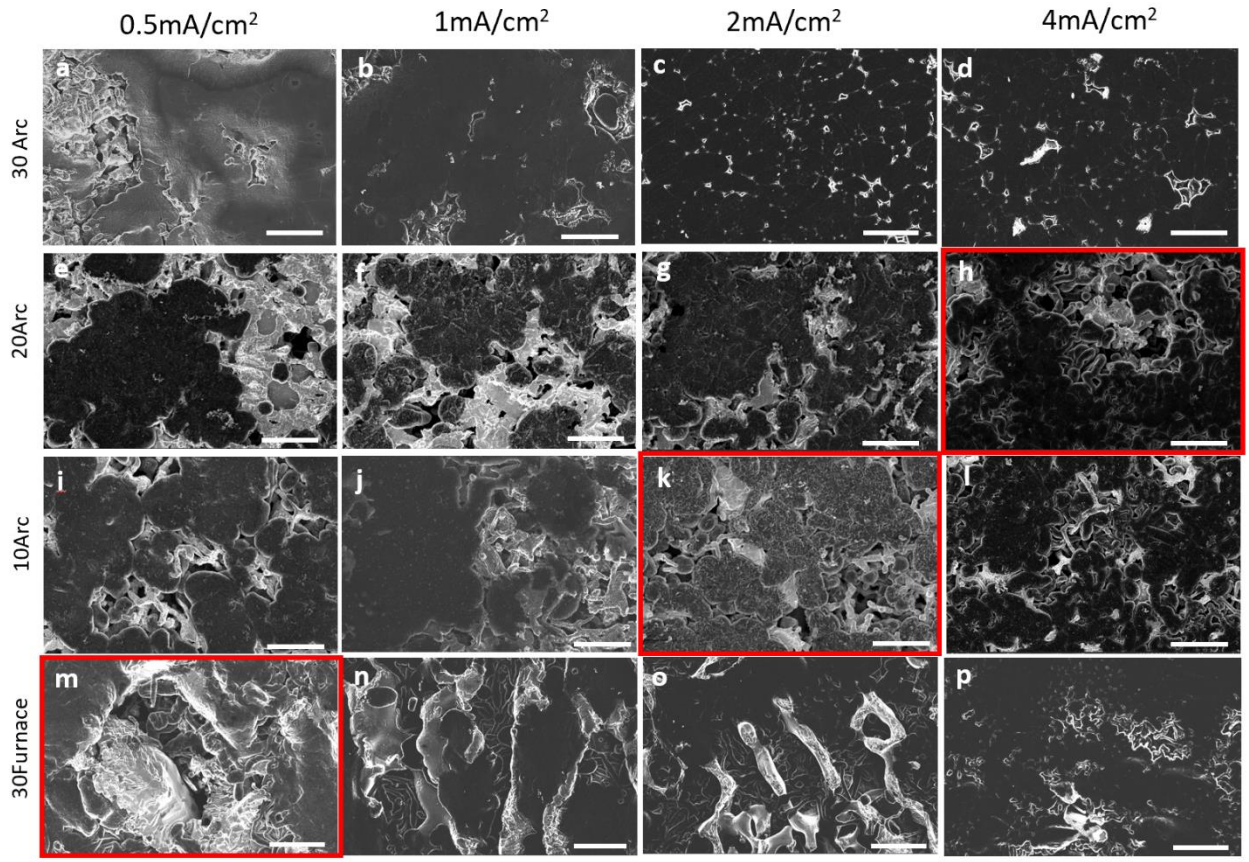

Figure 2.3 Top-view SEM images of the morphology of lithium plated under different current densities onto the porous copper networks with different pore sizes: a-d) 30Arc; e-h) 20Arc; i-l) 10Arc; m-p) 30Furnace. Current densities are indicated on the figure. The critical current densities at which lithium whiskers start to grow are marked with red boxes. All samples were plated to 4 mAh/cm^2 before imaging.

The effect of the surface area on the morphology of the deposited lithium was characterized using top-view SEM images. For each sample, 4 mAh/cm^2 of lithium was plated onto the porous copper using 4 different current densities, each of which are indicated in Fig. 3. As the surface area decreases with the increase of pore size, the effective local current density per unit surface area of Cu would also increases. It is widely accepted that high local current densities can lead to an inhomogeneous flux of lithium ions during plating, causing the formation of lithium whiskers.[17] By studying the lithium deposition morphology on the porous Cu networks with different surface areas under a range of current densities, the critical current density at which lithium whiskers begins to grow in each sample can be determined.

With the largest effective surface area, which is 29.49 cm^2 in a piece with 0.7 cm diameter and 200 μm thickness, the 30Arc samples produces a dense and smooth lithium deposition morphology throughout the four current densities tested. As the effective surface area decreased to 12.03 cm^2, the 20Arc samples also show relatively dense morphology in most of the current densities tested except at 4 mA/cm^2, which is indicated by the red box in Fig. 3h. At this

current density, lithium whiskers begin to grow on the surface of the pore channels, which means that the local current density becomes too high, inducing inhomogeneous lithium ions transport. As the effective surface area is further decreased, the critical current density also decreased. In the 30Furnace sample, where the effective surface area was only 3.76 cm^2, lithium whiskers were observed at current densities as low as 0.5 mA/cm^2, which means the critical current density might be even lower than that. Based on these observations alone, it seems that the higher the surface area in the porous copper, the better the Li morphology.

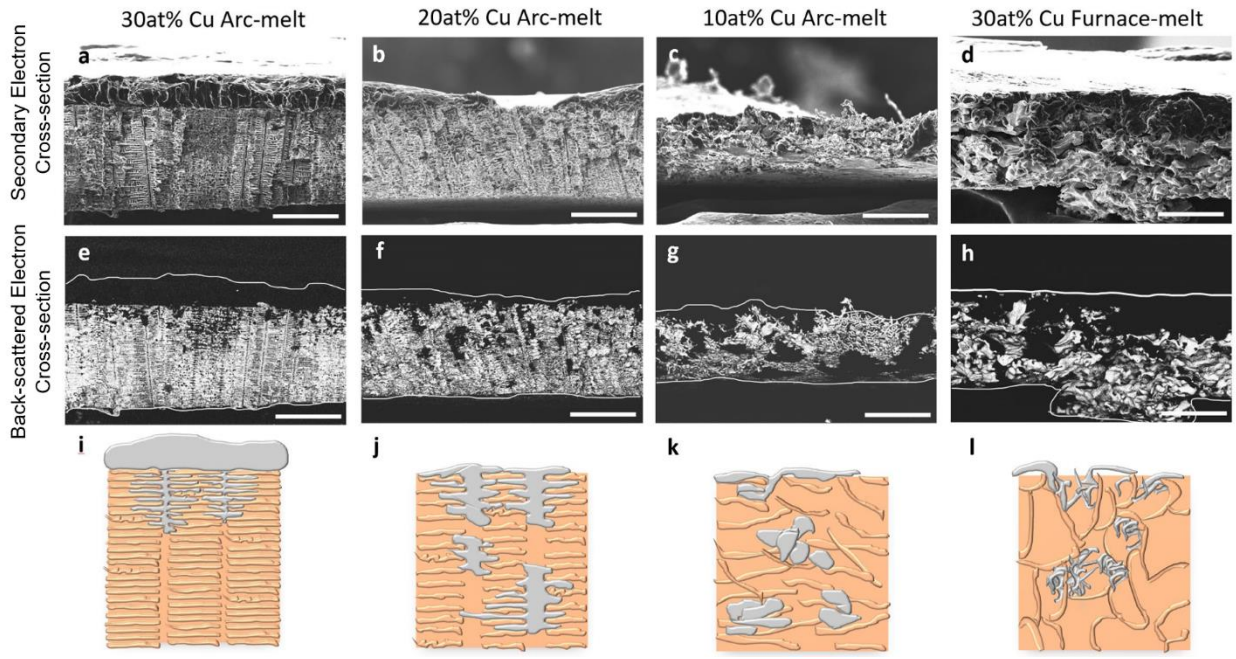

Figure 2.4. a-d) Cross-sectional secondary electron SEM images, e-h) back-scattered electron SEM images and i-l) cartoon illustrations of the observed lithium spatial distribution in the cross-section of each porous Cu sample. All samples were plated to 20 mAh/ cm^2. The scale bars in all images correspond to 50 µm.

The effect of the geometric tortuosity and pore size of the porous Cu network on the deposited lithium morphology was studied by cross-sectional SEM images. Fig. 4 shows the distribution of deposited lithium in each porous Cu sample after plating for 20 hours at 1 mA/cm^2. Back-scattered electron (BSE) images (Fig. 4e-h) give a clear view of how lithium is distributed across the whole porous copper network: the brighter region is copper, the darker region is lithium, and the boundary between vacuum and lithium is marked by white lines. Cartoon schemes were also constructed to better illustrate the observed lithium deposition distribution and morphology in the different porous copper samples (Fig. 4i-l).

With the smallest pore diameter (~4 µm) and the highest z-directional geometric tortuosity (1.35), the 30Arc samples gave the most inhomogeneous distribution of the deposited lithium within the volume (Fig 4a, 4e, 4i). Most of the deposited lithium accumulated on the top surface on the porous copper, and the space inside the pores, where the lithium was supposed to

deposit, was mostly empty. This inhomogeneous distribution of deposited lithium can be attributed to the complex structure of the porous copper, with small pores and high geometric tortuosity hampering lithium ions transport and accessibility to the majority of the structure pores. As we increased the pore size to ~10 µm, which led to a decrease in the z-directional geometric tortuosity to 1.28, the distribution of the deposited lithium in the porous copper changed dramatically (Fig 4b, 4f, 4j). More lithium was deposited inside the pores of the Cu instead of on the top surface. The higher utilization of the empty pores increases the contact area between lithium and the copper, which should lower the local effective current density and result in a more uniform morphology. The further increase in the pore size (~20 µm) and the decrease in the geometric tortuosity (1.03) allowed more lithium to grow inside the pores (Fig 4c, 4g, 4k). The deposited lithium grew in a bulky way and had a clustered morphology inside the porous Cu. In the largest porous Cu (~25 µm), the distribution of the deposited lithium was similar to that in the 10Arc sample. However, the increase of the pore size also led to a decrease of surface area. As a result, the morphology of the deposited lithium changed from bulky to whisker-like (Figure 4d, 4h, 4l). This change of morphology should eventually lead to the formation of inactive metallic lithium and cause the decrease in coulombic efficiency.[3]

To gain further insights into the factors limiting Li deposition in these porous copper structures, a computational study focused on the tortuosity factor was carried out. Such a study was designed to capture the evolution of the tortuosity factor with the increase of Li deposition in the different porous Cu structures. The tomographic structure of each sample was imported into MATLAB and the full whole volume of each sample was used for the calculation. An *in-house* MATLAB®-based algorithm was then used for the stochastic generation of lithium deposited in each porous copper sample. This algorithm favored the deposition of lithium in aggregated form, since that is what was observed experimentally. To further match with the experimental observations, a given amount of lithium was allowed to deposit on the top of the porous Cu and a deposition gradient was applied along the depth from the top to the bottom. Then, the tortuosity factor was determined for each of the resulting structures using the software TauFactor,[36] which relies on Fickian diffusion. Because of the stochastic nature of the lithium deposition simulation, each simulation was repeated between 5 and 10 times to ensure reproducibility and sufficient statistics.

The tortuosity factor results are reported in Fig. 5a for each porous Cu samples as a function of the plated lithium capacity. It appears that the tortuosity factor follows a gentle exponential rise until a certain threshold where it sharply increases (see Supporting Information Fig. 5a and Table S3). The larger the pores, the higher the threshold capacity corresponding to the steep rise in the tortuosity factor. The 30Arc sample has the smallest pores, and as a result the tortuosity factor begins to increase rapidly at the lowest capacity for this sample (at around 6 mAh/cm^2). It is noteworthy that the 30Furnace sample shows a higher tortuosity factor than the 10Arc sample until a capacity of 7 mAh/cm^2, the reason for that has been discussed in the previous section. From the 3D images on Fig. 5b, the large pores of the two structures (10Arc and 30Furnace) do not look to be clogged with lithium at 4 mAh/cm^2. At low capacities, it thus seems that if the pores are large enough to accommodate the lithium deposition, the interconnectivity of the pores and the tortuosity of the empty pores will be the most important

parameters. However, at 7 mAh/cm^2, the lithium deposits appear to be significantly denser. Indeed, beyond 7 mAh/cm^2 the 30Furnace structure displays a lower tortuosity factor which suggests that at higher capacities, the pores in the 3D structure might be filled and thus not able to accommodate more Li.

Based on the observations above, the effect of the tortuosity factor can be summarized as following. The narrow and tortuous structures, such as the case in the 30Arc sample, would largely hinder the transport of lithium ions, leading to an inhomogeneous distribution of the deposited lithium. The inhomogeneous distribution would also waste the empty space and surface area provided by the 3D structure and possibly lead to the formation of lithium whiskers after the top surface is fully covered by the deposited lithium. Therefore, as mentioned previously, an increase in surface area does not always lead to a more uniform morphology for the deposited lithium. The increase of surface area and the decrease of pore size can have competing effects. From the data presented here, it appears that the sample with high enough surface area to provide a uniform morphology for lithium deposited at various plating rates and with pore that are large enough to facilitate lithium ion transport is the 20Arc material. The material seems to be near the "sweet spot" in this porous copper system.

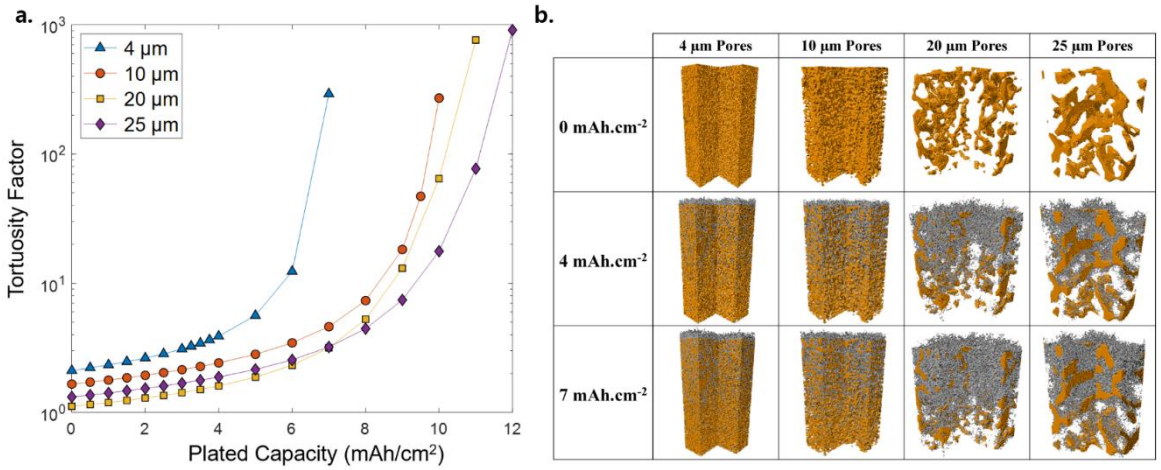

Figure 2.5. a) Tortuosity factor as a function of the capacity of Li plated into each porous copper structure; b) Porous coppers before (0 mAh/cm^2) and after (4 and 7 mAh/cm^2) Li deposition with the copper in gray and the Li in orange. The whole thickness of the current collectors is displayed with a square base of 100 µm of length. One quarter of each structure was removed for visualization-sake.

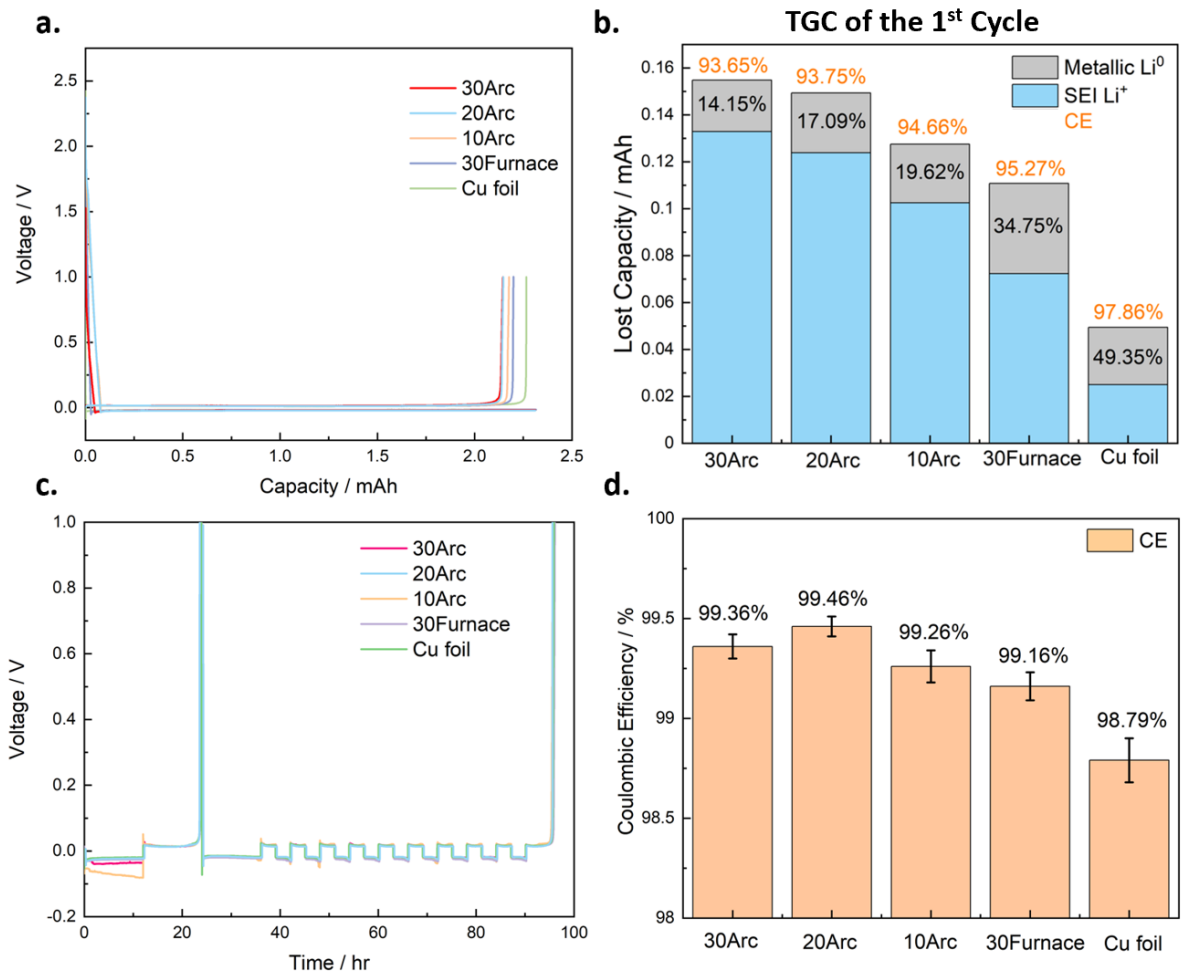

Figure 2.6. a) Electrochemical potential curve for lithium plating and stripping on each of the porous copper samples. b) TGC quantification of the SEI and inactive metallic lithium fractions for each sample. c) Electrochemical potential curve for CE testing for each porous copper sample. d) The calculated average CE of each porous copper sample from the half plating-stripping testing protocol.

To evaluate our prediction for the performance of the porous copper based on their physical parameters, Li||Cu cells were made to test the CE for lithium plating/stripping. The first cycle CE was calculated by plating 6mAh/cm^2 of lithium onto the porous coppers and stripping at 0.5mA/cm^2. After that, TGC was applied to quantify the amount of SEI Li^+ and inactive metallic Li^0 formed on the first cycle. In the TGC experiment, a fixed amount of deionized (DI) water was added to the cycled porous copper electrode, the inactive metallic lithium that was not removed during stripping will react with the DI water and release hydrogen gas. The amount the hydrogen gas quantified through gas chromatography can be directly correlated to the amount of the inactive metallic Li^0 left on the porous copper. It is known that CE values below 100% in each cycle of lithium plating/stripping comes from the combination of SEI Li^+ formation and formation of inactive metallic Li^0. By quantifying the fraction of inactive metallic Li^0, the SEI

Li^+ can then be calculated from the CE, and the combination of both values can help us to understand the failure model of each porous copper sample.

As shown in Fig 6b, the 30Arc samples showed the lowest CE on the first cycle, which was 93.65%. However, the amount of inactive metallic Li^0 formed was only 0.0219 mAh, which was only 14.15% of the total irreversible capacity, the lowest among the five types of coppers tested. The results show that although the high surface area of the 30Arc helped to improve the morphology of the deposited lithium, which is reflected in low percentage of inactive metallic Li^0, the high surface area also provided more contact surface between the electrolyte and lithium metal, which is thermodynamically unstable and leads to the formation of SEI under most conditions. In addition, during the first cycle due to the presence of CuO_x, Li would first react with this oxides layer and form SEI, which also contributes to the low CE. This is most prominently shown in the first cycle CE of the 30Arc sample, as it has the highest surface area. While the CuO_x is an issue only in the first cycle, the SEI in the high surface area samples remains a problem throughout cycles. For the 20Arc samples, with the decrease in surface area, the amount of SEI also decreased while the formation of inactive metallic Li^0 remained low. Therefore, an increase in CE was observed. As the surface area further decreased, the formation SEI also decreased in the 10Arc and 30Furnace samples. However, due to the low surface area of the 30Furnace samples, some lithium whiskers formed in these samples (Fig. 3m), increasing the fraction of inactive metallic Li^0. The sample with the highest CE in the first cycle is the 2D copper foil. The high CE in the copper foil comes from two reasons: 1) The low surface area of the copper foil limits the contact area between lithium and electrolyte and the amount of CuO_x that can form, thus leading to lower SEI formation; 2) The stack pressure on the copper foil from the coin cell also helped more lithium be stripped back to the electrolyte, whereas the stacking pressure inside porous copper was nearly zero, so the lithium can more easily detach from the copper substrate during stripping.

Based on the analysis above, it can be concluded that although the high surface area can help lithium to grow in a better morphology, the extra surface area also causes the formation of extra SEI. These competing factors led us to use a more representative way to determine the CE of the lithium plating/stripping. As shown in Fig. 6c, a half plating and stripping method was utilized to characterize the CE of the lithium plating/stripping. In this method, first, a full lithium plating/stripping cycle was performed to condition the surface of the coppers. Then, 6 mAh/cm^2 of lithium reservoir (Q_P) was plated onto the coppers at 0.5 mA/cm^2, followed by 9 cycles of striping and plating of 3 mAh/cm^2 of the lithium (Q_{half}). At the last step, all the remaining lithium was stripped to the cutoff voltage of 1V (Q_S). The average CE is calculated by $(9Q_{half} + Q_S)/(9Q_{half} + Q_P)\times100\%$. While the conventional CE testing method can tell us the efficiency of each cycle, it will include the capacity lost due to the formation of fresh SEI on cycle. The half plating and stripping technique leaves a layer of lithium reservoir after the first cycle, which can lead the lithium to fill back into the pre-existing SEI layer to minimize its formation. Furthermore, the first formation cycle has also consumed most of the oxides layer on the porous copper, leaving behind a relatively clean surface for Li metal deposition. Using this method, the average CE of the 30Arc, 20Arc, 10Arc, 30Furnace and copper foil was calculated to be 99.36%, 99.46%, 99.26%, 99.16% and 98.79% as shown in Fig. 6d. The preconditioning and the half

plating and stripping technique greatly minimized the formation of SEI in each cycle and the CE is directly reflecting effect of the morphology and the distribution of the deposited lithium. As predicted earlier, the 20Arc shows the highest CE because of its relatively high surface area and also large pore size.

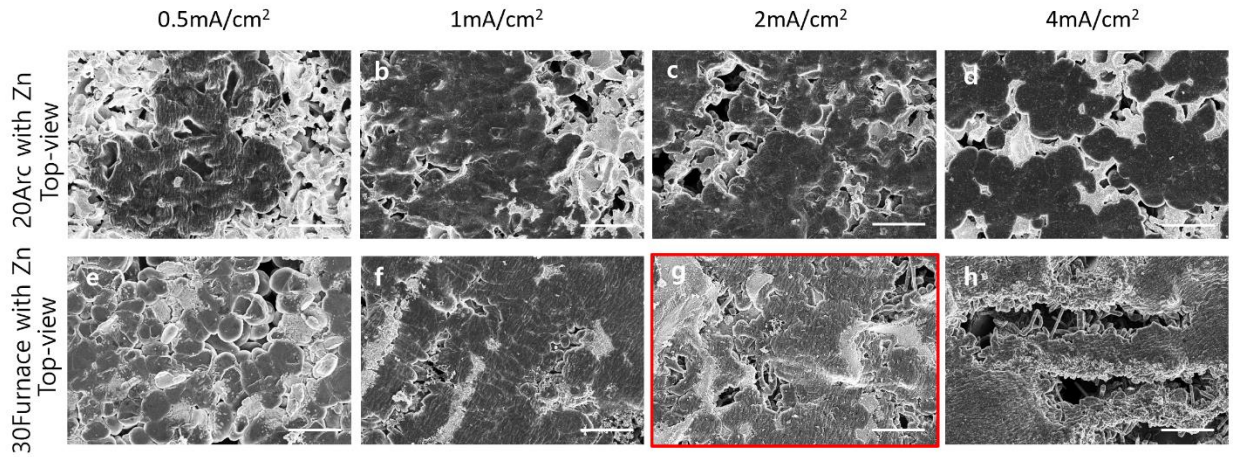

Figure 2.7. Top-view SEM images of the morphology of the lithium plated under different current density onto porous copper with a Zn coating. a-d) 20Arc sample coated with Zn; e-h) 30Furnace sample coated with Zn. The deposited Li is shown in darker contrast, while the brighter contrast shows the porous copper substrate. The critical current density at which lithium whiskers start to grow is marked with a red box. All samples were plated to 4mAh/cm^2.

The last parameter that can affect the performance of a 3D current collector is the surface chemistry. It is known that the electrochemical property of the substrate on which Li is plated can significantly influence the morphology of the Li.[19,20] To quantitatively explore how the improvement in surface chemistry can bring to the performance of the porous copper current collectors, metallic Zn, which has a lower nucleation barrier for Li than Cu,[20] was electrochemically coated onto 20Arc and 30Furnace samples. These two samples were chosen because they showed the best and the worst performance, respectively, based on the data presented above. The XRD in Figs. S10 and S11 show that upon Zn coating, the Cu and Zn form an alloy of $CuZn_5$ and Cu_5Zn_8. The SEM images of the as-made and post-coating samples (Figs. a and b in S12 and S16) show that the grains of the Cu-Zn alloy are in the sub-micron scale. Furthermore, the EDS in the coated samples (Fig. S13 and S17) shows coverage of zinc all over the sample with little oxygen. Plating inside of pores is not generally as easy as plating on top of a film, and indeed, in this case, the thickness of the Zn is greater on the top of the sample. To quantify the Zn thickness at the top and middle of the sample. EDS mapping was performed on a cross-sectional slice of each sample. As expected, the Zn intensity is brightest at the top and the bottom of the sample, but homogeneous Zn intensity is observed across the thickness of the sample (Figures S14 and S18). This intensity was quantified by integrating regions from the top and middle parts of the cross-section for both the 20Arc and 30Furnace samples after Zn coating (Figure S15 and S19). The Zn-thickness was calculated at the top and through the middle of the cross-section of the sample using the Zn and Cu weight % obtained from the metal K-α peaks and their densities. This was combined with the average cylindrical strut widths of 4um and 7um

diameters for the 20Arc and 30Furnace, respectively, as determined from SEM imaging (Figures S12A and S15A). For the 30Furnace, the calculated Zn-thickness on the top is 1100nm, and 44nm on the inside of the sample. For the 20Arc, the calculated Zn thickness on the top is 425nm and 35nm on the inside of the sample (Tables S4 and S5). While these interior thickness are much smaller than the overlayer on the top, they still provide nucleation sites for Li plating within the interior of the porous Cu.

To study the role of Zn coating, Li was electrochemically deposited onto the bare porous copper and Zn coated porous copper. The Li metal nucleation overpotential, which is defined as the voltage difference between the bottom of the voltage dip and the flat part of the voltage plateau, is a parameter that represents the energy barrier that Li needs to overcome to nucleate on the substrate.[20] As shown in Fig. S21, the nucleation overpotentials of 20Arc and 20Arc with Zn are found to be 46.1 mV and 32.5 mV respectively, meaning that the Zn coating successfully lower the nucleation barrier of Li depositing on the substrate, which should potentially lead to a more uniform and dense morphology.

The morphology of deposited Li on the Zn coated porous copper was then studied by SEM. As shown in Fig. 7a-d, the resulting Li morphology after plating in the 20Arc sample coated with Zn is dendrite free across the whole range of current density tested. This result stands in contrast to the uncoated 20Arc sample, where Li whiskers begin to appear at 4mA/cm^2. An even more dramatic improvement in Li morphology is observed in 30Furnace sample, however. As shown in Fig. 7e-h, the Li deposited Li on the 30Furnace sample coated with Zn shows a spherical morphology at 0.5 mA/cm^2. Even at this low current density, a whisker morphology was already seen in the uncoated samples. Li whiskers only begin to grow at a much higher current density of 2mA/cm^2.

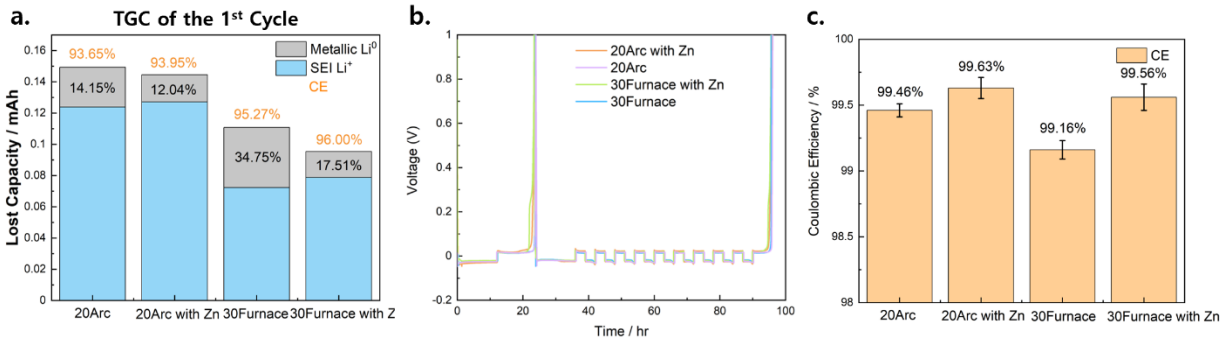

Figure 2.8. The electrochemical performance of Zn coated porous coppers: a) TGC analysis of the SEI and inactive metallic lithium; b) the electrochemical potential curve of CE testing of the porous copper samples; c) The calculated average CE of the Zn-coated porous copper sample from the half plating-stripping testing protocol.

The porous samples with Zn coatings were further tested for plating/stripping CE using the protocol mentioned previously. The 20Arc sample coated with Zn had an average CE of 99.63 %, which increased from 99.46 % of the uncoated samples, while the 30Furnace sample

coated with Zn had a CE of 99.56 %, which increased from 99.16 % of the uncoated samples, as shown in Fig. 8c. The amount of SEI Li^+ and metallic Li^0 in the first cycled was again quantified using TGC (Fig. 8a). The first cycle CE of the 20Arc samples improved only by a small amount after coating because the lithium morphology in the 20Arc was already dense without the coating, and the surface area was not significantly changed by the coating so that the SEI formed from the reaction between Li and oxides layer did not change much. The absolute amount of inactive metallic Li^0 did markedly decrease, however, presumably because of more effective Li nucleation on the improved surface. This was partly offset by a slight increase in the SEI Li^+, likely because the Cu_4Zn is more reactive toward oxygen or water than pure Cu. A more significant improvement was observed in the 30Furnace after coating. The first cycle CE improved from 95.27 % to 96.00 %, while the amount of inactive metallic Li^0 also markedly decreased because of the improved morphology. Again, a slight increase in the SEI Li^+ was observed, but change was not large enough to offset the large gains from the reduction in inactive metallic Li^0 due to the improved plating onto the lithophilic surface. The decrease in the inactive metallic Li^0 and improved cycling performance was more obvious in the 30Furnace sample upon coating with Zn than in the 20Arc sample, which proved that tuning the surface chemistry is an effective way to enable a 3D current with low surface area to achieve uniform Li plating.

2.4 Conclusions

In this work, porous copper scaffolds with interconnected micro-channels were synthesized using wet chemical etching and used as 3D current collectors for lithium metal anode. Laboratory X-ray tomography was used to quantify the physical properties of the porous copper materials. The effects of the three key parameters – surface area, tortuosity, and surface chemistry – were carefully studied. Similar to what previous work has mentioned[27], we quantitatively studied why the high surface area was harmful to the performance of the 3D current collectors, as Li metal was not able to plate deep into the pores due to diffusion limitations and more SEI was formed on the first cycle. A moderate surface area is desirable for a 3D current collector, where the local current density will be low enough to suppress the growth of lithium whiskers while keeping the formation of SEI to minimum. The tortuosity of the porous copper mainly influences the diffusion of lithium ions. To facilitate a uniform distribution of deposited lithium across the whole 3D current collector, the pore size should be kept as large as possible while the tortuosity should be minimized. In considering all of these key physical parameters, the 20Arc samples, with a balance of modest surface area and reasonable pore size, was shown to have the best performance among the copper samples tested, while the 30Furnace sample, which has very large pores and low surface area, had the worst.

These two samples were further coated with metallic Zn to evaluate how surface chemistry can influence the performance of 3D current collectors. Upon electrochemical testing, an average lithium plating/stripping CE of 99.56% was achieved in 30Furnace with Zn coated, which improved from 99.16% without coating. However, the CE for the 20Arc sample did not show as much improvement with the Zn coating because the morphology of the Li in 20Arc was already exceptionally good without coating. The results in this work led to several key points: 1)

Although the high surface area can lower the local current density and lead to a uniform Li morphology, it will also introduce large amount of SEI formation because of the increase in surface area. 2) The tortuosity of the 3D current collector should be kept at minimum to induce the uniform distribution of Li in the structure. 3) The Zn coating can effectively improve the morphology of the Li, allowing even 3D current collectors with low surface area to achieve uniform Li plating

2.5 References

(1) Xu, W. *et al.* Lithium metal anodes for rechargeable batteries. *Energy Environ. Sci.* **7**, 513–537 (2014).

(2) Lin, D., Liu, Y. & Cui, Y. Reviving the lithium metal anode for high-energy batteries. *Nat. Nanotechnol.* **12**, 194 (2017).

(3) Fang, C., Wang, X. & Meng, Y. S. Key Issues Hindering a Practical Lithium-Metal Anode. *Trends Chem.* **1**, 152–158 (2019).

(4) Lu, D. *et al.* Failure Mechanism for Fast-Charged Lithium Metal Batteries with Liquid Electrolytes. *Adv. Energy Mater.* **5**, 1400993 (2015).

(5) Ding, F. *et al.* Dendrite-Free Lithium Deposition via Self-Healing Electrostatic Shield Mechanism. *J. Am. Chem. Soc.* **135**, 4450–4456 (2013).

(6) Shiraishi, S. Surface Condition Changes in Lithium Metal Deposited in Nonaqueous Electrolyte Containing HF by Dissolution-Deposition Cycles. *J. Electrochem. Soc.* **146**, 1633 (1999).

(7) Liu, H. *et al.* Structure and Solution Dynamics of Lithium Methyl Carbonate as a Protective Layer For Lithium Metal. *ACS Appl. Energy Mater.* **1**, 1864–1869 (2018).

(8) Qian, J. *et al.* High rate and stable cycling of lithium metal anode. *Nat. Commun.* **6**, 6362 (2015).

(9) Suo, L., Hu, Y.-S., Li, H., Armand, M. & Chen, L. A new class of Solvent-in-Salt electrolyte for high-energy rechargeable metallic lithium batteries. *Nat. Commun.* **4**, 1481 (2013).

(10) Alvarado, J. *et al.* Bisalt ether electrolytes: A pathway towards lithium metal batteries with Ni-rich cathodes. *Energy Environ. Sci.* **12**, 780–794 (2019).

(11) Chen, S. *et al.* High-Voltage Lithium-Metal Batteries Enabled by Localized High-Concentration Electrolytes. *Adv. Mater.* **30**, 1–7 (2018).

(12) Chen, S. *et al.* High-Efficiency Lithium Metal Batteries with Fire-Retardant Electrolytes.

Joule **2**, 1548–1558 (2018).

(13) Ren, X. *et al.* Localized High-Concentration Sulfone Electrolytes for High-Efficiency Lithium-Metal Batteries. *Chem* **4**, 1877–1892 (2018).

(14) Xiao, B. J. How lithium dendrites form in liquid batteries. **366**, 426–428 (2019).

(15) Jin, S., Jiang, Y., Ji, H. & Yu, Y. Advanced 3D Current Collectors for Lithium-Based Batteries. *Adv. Mater.* **1802014**, 1–13 (2018).

(16) Liu, J. *et al.* Pathways for practical high-energy long-cycling lithium metal batteries. *Nat. Energy* **4**, 180–186 (2019).

(17) Pei, A., Zheng, G., Shi, F., Li, Y. & Cui, Y. Nanoscale Nucleation and Growth of Electrodeposited Lithium Metal. *Nano Lett.* **17**, 1132–1139 (2017).

(18) Shen, L. *et al.* Progress on Lithium Dendrite Suppression Strategies from the Interior to Exterior by Hierarchical Structure Designs. *Small* **16**, 1–40 (2020).

(19) Niu, C. *et al.* Self-smoothing anode for achieving high-energy lithium metal batteries under realistic conditions. *Nat. Nanotechnol.* **1**, (2019).

(20) Yan, K. *et al.* Selective deposition and stable encapsulation of lithium through heterogeneous seeded growth. *Nat. Energy* **1**, (2016).

(21) Li, G. *et al.* Stable metal battery anodes enabled by polyethylenimine sponge hosts by way of electrokinetic effects. *Nat. Energy* (2018). doi:10.1038/s41560-018-0276-z

(22) Zhang, R. *et al.* Conductive Nanostructured Scaffolds Render Low Local Current Density to Inhibit Lithium Dendrite Growth. *Adv. Mater.* **28**, 2155–2162 (2016).

(23) Liu, Y. *et al.* Oxygen and nitrogen co-doped porous carbon granules enabling dendrite-free lithium metal anode. *Energy Storage Mater.* **18**, 320–327 (2019).

(24) Zhang, R. *et al.* N-Doped Graphene Modified 3D Porous Cu Current Collector toward Microscale Homogeneous Li Deposition for Li Metal Anodes. **1800914**, 1–9 (2018).

(25) Zheng, G. *et al.* Interconnected hollow carbon nanospheres for stable lithium metal anodes. *Nat. Nanotechnol.* **9**, 618 (2014).

(26) Zhao, H. *et al.* Compact 3D Copper with Uniform Porous Structure Derived by Electrochemical Dealloying as Dendrite-Free Lithium Metal Anode Current Collector. *Adv. Energy Mater.* **8**, 1–8 (2018).

(27) Wang, Y. *et al.* Spherical Li Deposited inside 3D Cu Skeleton as Anode with Ultrastable

Performance. *ACS Appl. Mater. Interfaces* **10**, 20244–20249 (2018).

(28) Yue, Y. & Liang, H. 3D Current Collectors for Lithium-Ion Batteries: A Topical Review. *Small Methods* **1800056**, 1800056 (2018).

(29) Yun, Q. *et al.* Chemical Dealloying Derived 3D Porous Current Collector for Li Metal Anodes. *Adv. Mater.* 6932–6939 (2016). doi:10.1002/adma.201601409

(30) Chen, K. H., Sanchez, A. J., Kazyak, E., Davis, A. L. & Dasgupta, N. P. Synergistic Effect of 3D Current Collectors and ALD Surface Modification for High Coulombic Efficiency Lithium Metal Anodes. *Adv. Energy Mater.* **9**, 1–12 (2019).

(31) Frisco, S. *et al.* Internal Morphologies of Cycled Li-Metal Electrodes Investigated by Nano-Scale Resolution X - ray Computed Tomography. **18757**, (2017).

(32) Ebner, M., Wood, V., Soc, J. E., Ebner, M. & Wood, V. Tool for Tortuosity Estimation in Lithium Ion Battery Porous Electrodes F OCUS I SSUE OF S ELECTED P RESENTATIONS FROM IMLB 2014 Tool for Tortuosity Estimation in Lithium Ion Battery Porous Electrodes. (2015). doi:10.1149/2.0111502jes

(33) Liu, H. *et al.* Unique 3D nanoporous / macroporous structure Cu current collector for dendrite-free lithium deposition. *Energy Storage Mater.* 0–1 (2018). doi:10.1016/j.ensm.2018.07.010

(34) Matsuda, S., Kubo, Y., Uosaki, K. & Nakanishi, S. Lithium-metal deposition/dissolution within internal space of CNT 3D matrix results in prolonged cycle of lithium-metal negative electrode. *Carbon N. Y.* **119**, 119–123 (2017).

(35) Fang, C. *et al.* batteries. *Nature* doi:10.1038/s41586-019-1481-z

(36) Cooper, S. J., Bertei, A., Shearing, P. R., Kilner, J. A. & Brandon, N. P. TauFactor: An open-source application for calculating tortuosity factors from tomographic data. *SoftwareX* **5**, 203–210 (2016).

Chapter 3: Increasing the lifetime of thick porous Cu current collectors for Lithium Metal Batteries via asymmetric lithiophilic coating

3.1. Introduction

Lithium metal batteries (LMBs) possess a number of outstanding characteristics compared to traditional lithium-ion batteries, including a low anode potential (3.04 V vs. standard hydrogen electrode) and a 10-fold improvement in anode specific capacity (3860 mAh/g) compared to conventional graphite anodes (372 mAh/g).[1,2] The main issue with commercializing LMB is the uneven deposition and stripping of Li, which leaves behind inactive "dead" Li after multiple cycles.[3] This inactive Li arises from the formation of dendritic structures, which also leads to excessive solid electrolyte interphase (SEI) formation that can consume the electrolyte. Furthermore, dendrite formation can cause short circuits and safety hazards.

One strategy to circumvent the dendrite formation issue has been to stabilize the SEI by making an artificial SEI to homogenize Li plating. For example, a ceramic thin-film of $Li_{0.35}La_{0.52}[V]_{0.13}TiO_3$ (LLTO) with high ionic and electronic conductivity can be deposited on the lithium metal surface, which is able to buffer the Li-ion concentration gradient and level secondary current distribution.[5] Alternatively, a polymeric artificial layer made out of polycationic poly(diallyl dimethyl ammonium) (PDDA) and bis(trifluoromethanesulfonyl)imide (TFSI) anions can also be used to stabilize Li plating on the anode.[6] The former provides an electrostatic shielding effect to unify Li-ion flux, while the latter brings hydrophobic characteristics to improve moisture stability on the SEI.

Other researchers have modified the liquid electrolyte to stabilize the SEI using dual-salt electrolytes or liquefied gas electrolytes. Dual-salt electrolytes can be used to make more flexible and conductive SEI layers while keeping the conductivity of the separator high due to the electrolyte's low wetting on the separator.[6] Liquefied gas electrolytes can improve the electrolyte's ionic conductivity while maintining Li metal stability.[6] To reduce safety concerns, the non-aqueous electrolyte can alternatively be replaced with a safer solid-state electrolyte (SSE).[8] However, this comes with other challenges such as low ionic conductivity, inferior solid-solid contact with electrode materials, and poor maneuverability due to the SSE's fragile nature.[9]

Another way to prevent dendrite formation is to modify the surface chemistry of the current collector onto which Li deposits.[10] The deposition of Li on 2D surfaces results in a non-uniform Li morphology due to the high energy to nucleate Li deposition. In order to make a denser Li deposition, lithiophilic metal surfaces (Ag,[11,12] Sb,[13] Zn,[14] Au[15]) can be used as seeds for Li nucleation. These metals possess high affinity towards Li because they can alloy with Li and have a small but finite Li solubility. Different lithiophilic surfaces have been previously studied and it was observed that the overpotential of nucleation greatly decreases, leading to denser Li morphologies compared to deposition on Cu.[16] However, 2D surfaces are not able to reach practical current densities due to their low surface area.

To reduce the local current density, 3D porous current collectors can help to suppress dendrite formation and decrease the Li volume expansion. Recent studies have used 3D carbon,[17,18] nickel,[19] copper[20,21] or lithium itself[22] as metallic scaffolds with substantial improvements from

their 2D counterpart. Some of the characteristics that make an efficient 3D current collector include having a pore size close to the Li nucleus size (1-10 μm) with narrow pore size distribution, low tortuosity and moderate pore depth (20-50μm) [23]. The appropriate pore size allows for a dense Li morphology, low tortuosity facilitates Li ions to easily diffuse in and out of the framework. and a moderate pore depth reduces the Li diffusion length and the chance of leaving large fractions of the pores unfilled. In addition, the capacity of a 3D current collector is determined by its thickness[24] and the open volume[25] available to store Li. Although thick 3D porous current collectors could increase the overall battery volume, it can also increase its capacity while keeping the mass of the battery low due to its low density.

When utilizing such a 3D current collector, the key goal is to develop methods to effectively fill the entire pore volume. During Li deposition onto a 3D current collector, the local Li current density inside the structure is governed by three resistances: the ionic resistance (R_{ion}) of the electrolyte confined in the 3D framework, the charge-transfer resistance (R_{ct}) for lithium deposition, and the electric resistance (R_e) which is the resistance in the 3D framework to conduct electrons (Fig. 1A).[26] While R_e is the lowest at the back of the current collector and increases moving through the porous network to the electrolyte interface, the larger term is the Li-ion concentration, which decreases from the top of the porous network at the interface with the electrolyte, down through the porous network. As a result, R_{ion} increases as the concentration of Li ions decreases, which leads to Li deposition that is 'top-favored' with the outermost pores of the framework filling preferentially, and pore clogging over cycles (Fig. 1B, top). This can accelerate the formation of dendritic structures and the sudden failure of the cell. In order to accommodate Li inside the 3D porous structure, Li deposition should be 'bottom-favored'.

A strategy to drive bottom-favored Li deposition is to make use of lithiophilic coatings like those described above. Unfortunately, while the use of a homogenous coating should facilitate deposition throughout the network, it does not mitigate the gradient in ionic conductivity, and thus the tendency for lithium to preferentially plate at the top porous network. To balance that ionic gradient, a gradient in coating density that increases in concentration from the electrolyte down the bottom of the porous network can be used to create a gradient in R_{ct} that balances the gradient in R_{ion} (Fig. 1B, bottom). With the most favorable lithophilic coating at the base of the porous network, Li ions should migrate inside the porous structure and deposit preferentially at the bottom of the framework because the Li nucleation barrier is the lowest there. Li should then continue to deposit at next lowest nucleation barrier, making its way up to the top of the framework.

In this paper, we test this gradient lithophilic coating strategy for 'bottom-favored' Li deposition using two macroporous Cu frameworks with average pore sizes of 10μm and 14μm. These Cu structures were made via arc-melting of a Cu-Fe pellets followed by acid etching of Fe to produce a porous network. The starting pellet composition of the 10 μm-pore size Cu structure was 30at%Cu-70at%Fe and that of the 14 μm-pore size Cu structure was 20at%Cu-80at%Fe. Therefore, they are denoted as 30-Cu and 20-Cu, respectively. Previous results[27] showed that these two frameworks developed dense Li morphology and high average coulombic efficiency (CE) over 10 cycles. However, these samples experienced a 'top-favored' Li deposition which limited their long-term performance. In this work, these samples were coated with a gradient of closely-packed

Ag nanoparticles via an electroless deposition method, with a goal of inducing 'bottom-favored' Li deposition. The gradient was achieved using an assymetric coating process, and the long-term performance of these asymmetrically coated samples is compared against an uncoated sample and a sample coated symmetrically with Ag to produce a homogeneous distribution of Ag nanopoarticles. The CE, the number of stable cycles, and the morphology is then analyzed at different current densities and capacities to provide insights into how this method can be used to optimize the performance of thick porous 3D current collectors in lithium metal batteries.

3.2. Experimental Section

1) Synthesis of porous 3D Copper Frameworks

Pure Cu powders (Fisher Scientific, electrolytic powder) and pure Fe powder (Beantown Chemical, −325 mesh, reduced, 98%) were used to prepare Cu–Fe precursor ingots with two different compositions: 20 atomic percent (atom %) Cu–80atom %Fe, and 30atom %Cu–70atom %Fe. The average powder size of both powders was about 30 μm. A hydraulic press was used to make pellets of 2cm in diameter for each composition. These pellets were then arc-melted under an argon atmosphere for 1-2 minutes with 70A of current five times to make homogeneous ingots with high cooling rates. The two different types of samples were sliced and polished using sandpaper to make samples 1 cm in diameter and 250 μm in thickness. Porous copper derived from these samples are denoted throughout this paper as 20-Cu and 30-Cu, in accordance with their starting composition.

After the Cu–Fe ingots were successfully synthesized, the disk was then etched in 5 wt% H_2SO_4 acid solution at 90 °C under constant stirring for 24 h. The acid solution was changed every 8 h to prevent the accumulation of contaminants. The etched sample was then cleaned in 5wt % HCl solution under sonication for 15 min. This was followed by a pure acetone (ACS reagent >99.5% pure) and 200 proof ethanol wash under sonication for 10 min each to wash away any leftover contaminants. Finally, the cleaned samples were dried under vacuum for 1 h.

2) Ag electroless coating

Both 20-Cu and 30-Cu samples were Ag-coated by immersing the samples in an electrolyte of 0.6mM $AgNO_3$ (Alfa Aesar, 99.95% metal basis) and 3mM Citric Acid Monohydrate (VWR, ACS grade) in ethanol. The symmetrically-coated samples were immersed in a 20mL solution for 1min while sonicating. The asymmetrically-coated samples were covered on the back and sides with tape, so that only a defined samples area on one side of the porous Cu was exposed to the electrolyte. This was immersed in the solution for 2min while sonicating and then the tape was removed. Both samples were then washed with acetone and 200 proof ethanol for 10 min each under sonication and then dried under vacuum for 1h.

3) Scanning Electron Microscope/Energy-Dispersive X-Ray Spectroscopy

A JEOL JSM-6700F scanning electron microscope (SEM) was used to study the structure of the as-prepared porous copper current collector as well as the morphology of the

electrochemically deposited lithium. Secondary electron SEM was used to image current collector microstructure and Li morphology studies and back-scattering electron (BSE) SEM was used to image the phase contrast between Li and Cu. Air-sensitive samples containing Li were bagged in an Ar-filled bag and loaded into the SEM with only 3 seconds of exposure to air. Energy-dispersive X-ray spectroscopy (EDS) was used to characterize the elemental composition of the samples.

4) Electrochemical Testing

CR2016-type coin cells were assembled in an Ar-filled glovebox for electrochemical characterization. The electrolyte consisted of 100 μL of 1 M lithium bis(trifluoromethane sulfonyl)imide (LiTFSI) in a mixed solvent of 1,3-dioxolane (DOL) and 1,2-dimethoxyethane (DME) (1:1 in volume) with 2% $LiNO_3$ and Li metal foil was used as the counter electrode. Current densities of 1mA/cm^2 (6mAh/cm^2), 2mA/cm^2 (10mAh/cm^2) and 4mA/cm^2 (10mAh/cm^2) were used for cycling. The first cycle (forming cycle) was ran at 0.5mA/cm^2 and 6mAh/cm^2 and the second cycle (alloying cycle) was ran at 0.005mA/cm^2 and 0.06mAh/cm^2 (Fig. S6).

5) X-Ray Diffraction

XRD was performed using a PANalytical X'Pert Pro powder diffractometer operating with Cu Kα radiation (λ = 1.5418 Å) using a 0.03° step size, a voltage of 45 kV, and a current of 40 mA. XRD patterns were recorded in the range of $15° < 2\theta < 85°$.

6) X-ray Photoelectron Spectroscopy (XPS)

XPS analysis was performed using a Kratos Axis Ultra DLD spectrometer with a monochromatic Al (Kα) radiation source. A charge neutralizer filament was used to control charging of the sample. A 20 eV pass energy was used with a 0.1 eV step size; scans were calibrated using adventitious carbon by setting the C 1s peak to 284.8 eV.

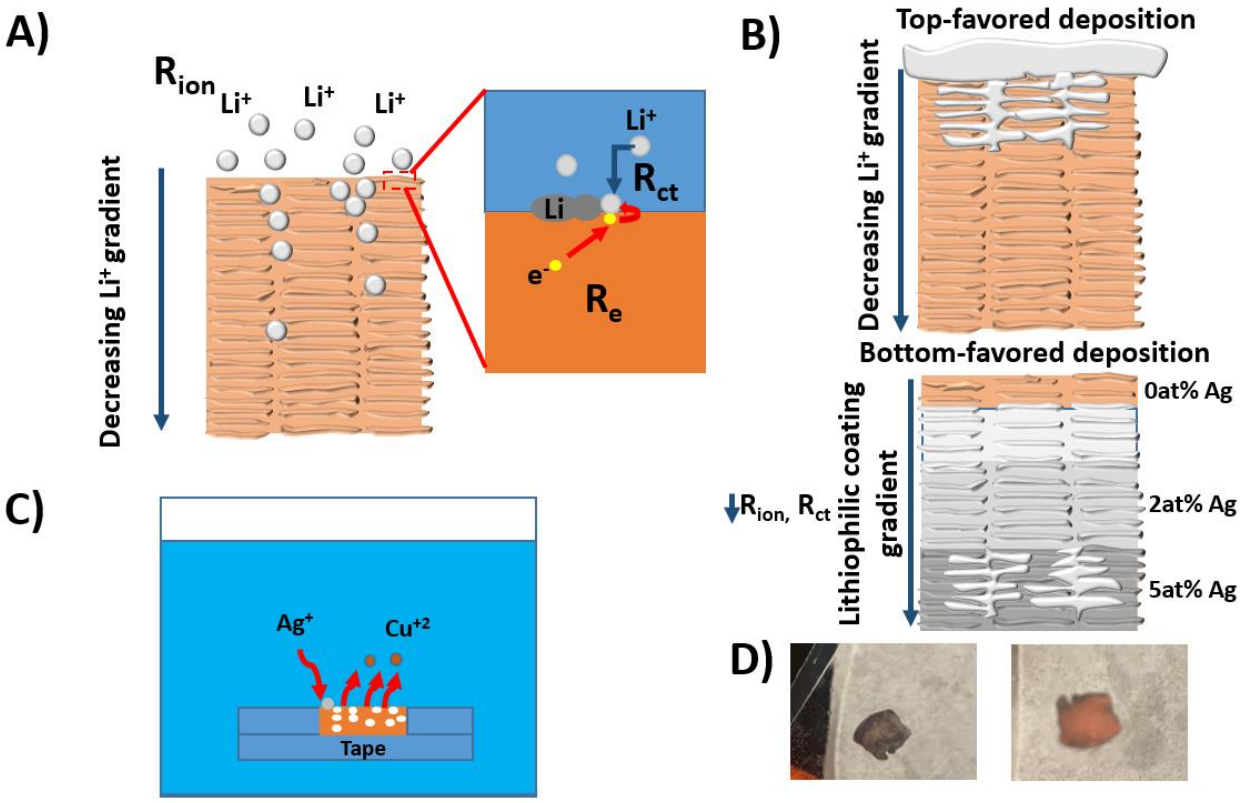

Figure 3.1. Schematic illustration of the Li plating process in a 3D porous network electrode and the three resistances involved: Li-ion diffusion inside the framework (R_{ion}), interfacial charge-transfer resistance at the reduction sites (R_{ct}), and electronic resistance to the current collector (R_e). B) Cartoon showing 'top-favored' Li deposition on an uncoated 3D framework and 'bottom-favored' Li deposition on an asymmetrically Ag-coated 3D framework. C) Cartoon of the process for electroless coating of Ag on Cu using a solution containing Ag^+. D) Optical image of a piece of asymmetrically coated porous Cu showing the Ag coated back (left) and the uncoated front (right).

3.3. Results and Discussion

A variety of samples with different pore sizes and coatings were used to fully understand how structural porosity and lithiophilic coatings can be used to to optimize lithium deposition. The following notation is used to refer to the samples used in this work: composition-surface chemistry-metal (i.e. 30-U-Cu refers to an uncoated Cu made from an ingot with 30at%Cu-70at%Fe composition). Samples of 30-Cu and 20-Cu with three different surface chemistries were made: uncoated Cu samples (30-U-Cu and 20-U-Cu), asymmetrically or 1-sided coated samples (30-1Ag-Cu and 20-1Ag-Cu) and symmetrically or 2-sided coated samples (30-2Ag-Cu and 20-2Ag-Cu). Figures 2A and 2D show the top-view of the 30-U-Cu and 20-U-Cu samples, with

average pore sizes of 10µm and 14 µm respectively. The ligaments of these samples before coating have a rough surface (Figs. 2B and 2E). XRD for the 30-Cu and 20-Cu samples show that the phase separated Fe is dissolved away after etching and cleaning, leaving only a Cu metal structure (Figures S1 and S2). After asymmetrically coating with Ag, the side exposed to the electrolyte shows ligaments covered with closely-packed nano-sized Ag particles (Figs. 2C and 2F). XRD shows no Ag peak in the 1Ag-Cu materials, as expected for a small amount of nano-sized Ag deposited, but a small, broad Ag peak is observed in the 2Ag-Cu samples (Figure S3). In addition, EDX mapping shows that Ag can be found homogeneously distributed across the Cu framework (Fig. S4). Finally, XPS corroborates the presence of Ag metal in addition Cu with a small amount of Cu oxide in the Ag-coated structures (Fig. S5).

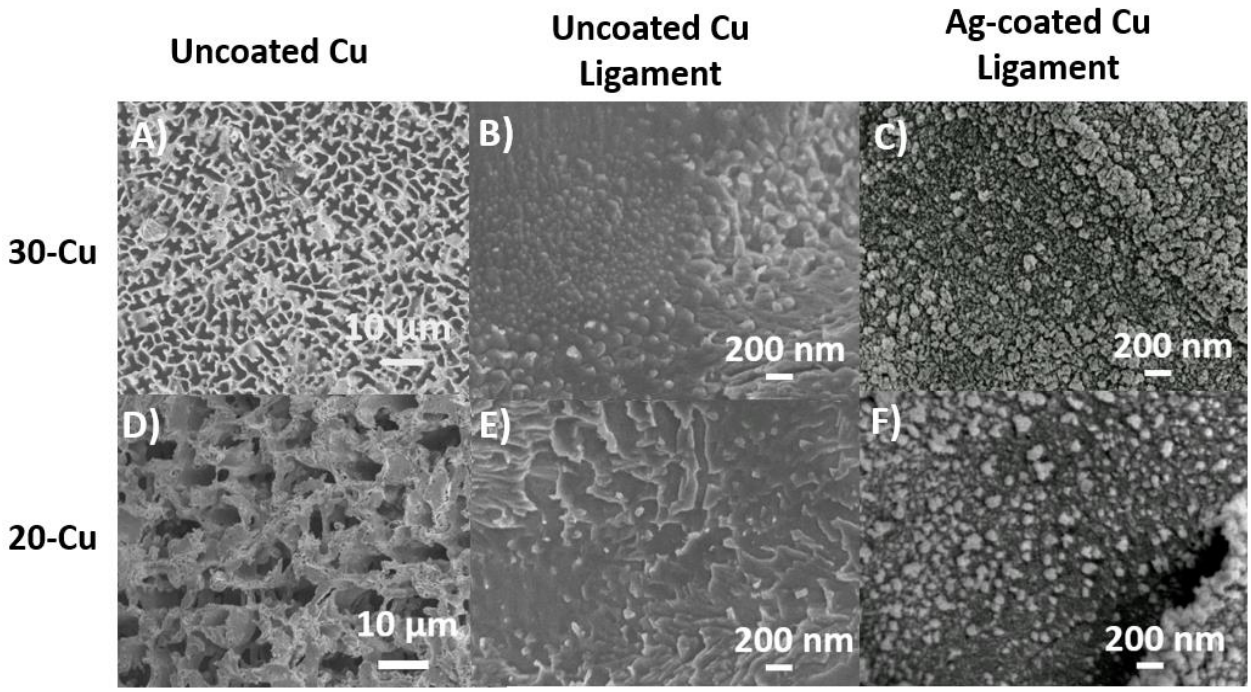

Figure 3.2. SEM images of the two 3D frameworks used in this work: A) 30Arc and D) 20Arc Cu with average pore sizes of 10µm and 14µm, respectively. Their respective ligaments show a rough surface before coating (B and E) and are completely covered by nano-sized Ag particles after electroless coating (C and F).

After proving that Ag is plated onto the porous Cu, the next challenge is to confirm a gradient in Ag density, and to see if that gradient affects the location of Li plating. To this end, 6mAh/cm^2 of Li was deposited at 1mA/cm^2 on 30-U-Cu and 30-1Ag-Cu samples. Backscattering SEM (BSE-SEM) images are useful in showing phase contrast between Li (dark areas) and Cu (light areas) thanks to their notable atomic size difference. Fig. 3A shows that for the 30-U-Cu sample, Li deposits almost entirely at the top of the porous framework, resulting in a black band above the open pores. For the case of the 30-1AgCu sample, however, the cross-section SEM images in Fig. 3B shows that there is Li located at the top, middle and bottom areas of the sample

(Figs. 3C-E). The EDX mapping across the cross-section of the sample shows the Ag gradient with an atomic fraction that decreases from 5 at% Ag at the bottom of the sample, to 0 at% Ag at the top (Figs. 3F-H). This shows directly that the asymmetric coating can lead to more homogeneous Li deposition throughout the porous network.

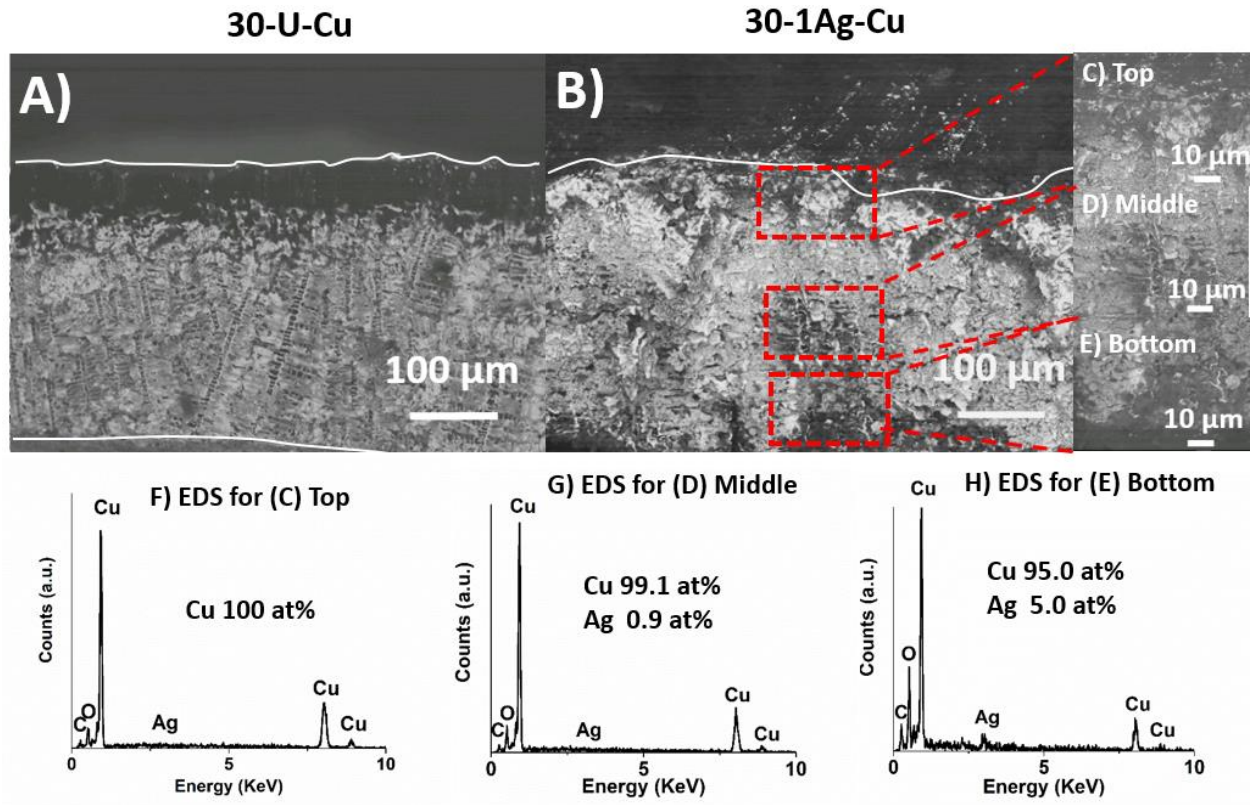

Figure 3.3. Cross-sectional BSE SEM of (A) 30-U-Cu and (B) 30-1Ag-Cu sample after deposition of 6mAh/cm2 at 1mA/cm2. The 30-1Ag-Cu sample shows Li areas on the C) top, D) middle and E) bottom of the cross-section. EDX spectra of the three regions (panels F), G), and H), respectively) shows the decreasing Ag content from bottom to top.

The electrochemical performance of the various samples was then tested by cycling them in half-cells with Li foil as the counter/reference electrode. The parameters of interest include the lifetime (includes cycles before CE drops below 90%), average coulombic efficiency during the cycle lifetime (excluding the first three cycles), the fluctuations in that coulombic efficiency, the potential difference between plating and stripping, and the nucleation overpotential. The fluctuations of the coulombic efficiency were quantified by calculating the average standard deviation every 5 cycles; this value provide information about how stably the battery is able to cycle, with instability indicative of Li dendrite formation. The potential difference between plating and stripping is quantified using the Li deposition plateau potential and the Li stripping plateau potential (Fig. S7) and it is proportional to the combination of R_i, R_e, and $R_{ct.}$. The nucleation overpotential is defined as the driving force used to overcome the heterogeneous nucleation barrier between Li ions and a metal surface. In the galvanostatic curve, it is the voltage dip at the beginning

of Li metal deposition, and it is followed by the voltage plateau for Li deposition. The capacities and current densities used were the following: 6mAh/cm^2 at 1mA/cm^2, 10mAh/cm^2 at 2mA/cm^2 and 10mAh/cm^2 at 4mA/cm^2. After the samples were cycled, an extra Li deposition under the same testing parameters was done and the cell was opened. Cross-sectional and top-view secondary electron and back-scattering electron SEM images were taken to examine the location and morphology of Li deposited.

To begin to understand the role of the Ag coating, three samples, 30-U-Cu, 30-1Ag-Cu, and 30-2Ag-Cu samples are first cycled to a capacity of 6mAh/cm^2 at a current of 1mA/cm^2 for 100 cycles. During cycling, the CE of 30-2Ag-Cu shows the most fluctuations, followed by the 30-U-Cu material, and then 30-1Ag-Cu samples (Fig. 4A), with the fluctuations likely caused by dendrite formation. We use the standard deviation of the CE to quantify these fluctuations, and find that the value goes up as the number of cycles increases for all samples, but the increase is much higher for the 30-U-Cu and 30-2Ag-Cu samples than for the 30-1Ag-Cu material (Fig. 4B). This means that over the 100 cycles examined in this experiment, the cells become less stable, likely due to an accumulation of inactive Li. The 30-1Ag-Cu sample was the most stable cell of the three, suggesting the least inactive Li formation, and thus the least Li dendrite formation. Fig. 4C shows the potential difference between plating and stripping at select cycles (the detailed analysis is shown in Fig. S7). The 30-1Ag-Cu material retains the lowest and most consistent potential difference of the three samples, which likely related to the reduced charge transfer resistance in this sample, where most of the lithium is plating inside of the pores, rather than on top.

The nucleation overpotential provides direct information on the nature of the surface where Li initially plates. In agreement with this idea, the nucleation overpotential of the 30-U-Cu material (Fig. 4D) starts with a high value of 49.2mV at the 3rd cycle, and then decreases down to 30.0mV for the 25th - 100th cycles. This decrease is likely due to residual Li that is left on the Cu after stripping that provides a nucleation site for the next plating cycle. Based on the SEM images in Fig. 5A-C, taken after the 3rd cycle, it appears that this Li plating takes place mostly on top of the 3D Cu. Both regular (Fig.5A) and back-scattered electron (BSE, Fig. 5B) images show a thick Li layer on top of the porous Cu, and Li is only observed in the pores nearest the top of the network (black in the BSE image), with open pores observed throughout the porous Cu (Fig. 5A). The top view image (Fig. 5C) also indicates that the pores are fully covered with a dense Li layer. As cycling continues, plating and stripping continue to take place large on top of the porous Cu, and a clear Li overlayer is observed after the 100th cycle by SEM, as observed by both standard and BSE SEM (Fig. 6A-B). Again Li is only found in the porous Cu near the top, but the region of Li containing copper appears to have grown somewhat (black in Fig. 6B), indicating progressively more infiltration with increased cycle number. Most of the pores remain open, however (Fig. 6A). With repeated plating and stripping, the deposition also becomes more uneven, and the smooth Li morphology of Fig. 5C evolves into a whisker-like morphology in Fig. 6C, indicative of dendrite formation.

The symmetrically coated 30-2Ag-Cu initially shows a much low nucleation overpotential (29.5mV) because Li metal is depositing on a lithiophilic surface (Fig. 4F). The overpotential decreases somewhat to 22.0 mV on the 25th cycle, then increases back to 31.0mV on the 100th cycle. These low values indicate a low R_{ct} in all cases, meaning Li is always plating on either a lithophilic Ag surface or on other Li. The variation may be due in part to R_i and the location of plating within the porous Cu. Initially, Li nucleates at many locations both on top of and inside the Ag-coated Cu pores, resulting in a broad voltage dip at rather high capacity (Fig. 4E). This behavior sits in strong contrast to the sharp dip at very low capacity in Fig. 4D for the uncoated material, which likely has little nucleation in the pores. As plating continues, the dip moves to lower capacity, but remains broad because of the combined effects of decreases in R_{ion} and R_{ct}. For this sample as well, most of the Li deposition appears to take place on top of the 3D structure, as shown by both standard and BSE cross-section SEM image (Figs. 5G-H). Top view SEM also shows a continuous Li overlayer after 3 cycles, although the Li plates with a favorable dense morphology (Fig. 5I). After the 100th cycle, the Li remains mostly on top of the porous Cu, with some Li infiltration near the top (Fig. 6G,H). The open pores can still be clearly images, indicating that they are not full of Li. Interestingly, unlike the uncoated sample, the Li morphology observed in top-view SEM remains dense, even after 100 cycles (Fig. 6I), indicating a positive effect from the Ag coated porous Cu, even if the Li is not all plating within the pores.

The most favorable behavior is observed in the 30-1Ag-Cu sample. In terms of nucleation overpotential, the material is very similar to the 30-2Ag-Cu material. It has a nucleation overpotential of 27.3mV at the 3rd cycle, which then decreases down to 20.0mV at the 25th cycle and increases to 25.5mV at the 100th cycle (Fig. 4E). These low values are consistent with nucleation on a lithiophilic surface, and the high capacity for the position of the dip is consistent with nucleation inside of the pores. SEM images, however, indicate the clear difference in this material. For the 30-1Ag-Cu sample, Li deposition appears to take place throughout the porous copper. After the 3rd cycle, Li can be observed all the way down to the bottom of the porous network (Fig. 5E), and the pores in Fig. 5D are mostly obscured, indicating they are filled with Li. In top-view SEM (Fig.5F), the pores can still be seen, indicating a lack of a thick Li overlayer. Furthermore, after the 100th cycle, the 30-1Ag-Cu sample still experiences 'bottom-favored' Li deposition with Li plating throughout the porous network, as indicated by the extensive dark regions in Fig. 6E, and the almost complete lack of open pores in Fig. 6D. While some Li can be observed on top of the porous Cu after 100 cycles in Fig. 6F, the pores can still be seen, ruling out the presence of a thick Li overlayer. The fact that Li deposits throughout the 30-1Ag-Cu sample, even after 100 cycles, helps to keep the overall thickness of the current collector low (287 μm) compared to the thickness of 30-U-Cu (351 μm). The electrochemical data along with the SEM images thus corroborate that the asymmetrical coating strategy to produce a gradient of Ag nucleation sites results in more stable cycling with a lower nucleation overpotential and less voltage hysteresis because Li deposition occurs within the porous Cu, rather than on top. Although none of the three Cu samples had failed at 100 cycles, the first 100 cycles provided a clear picture of the superior stability of the 30-1Ag-Cu sample.

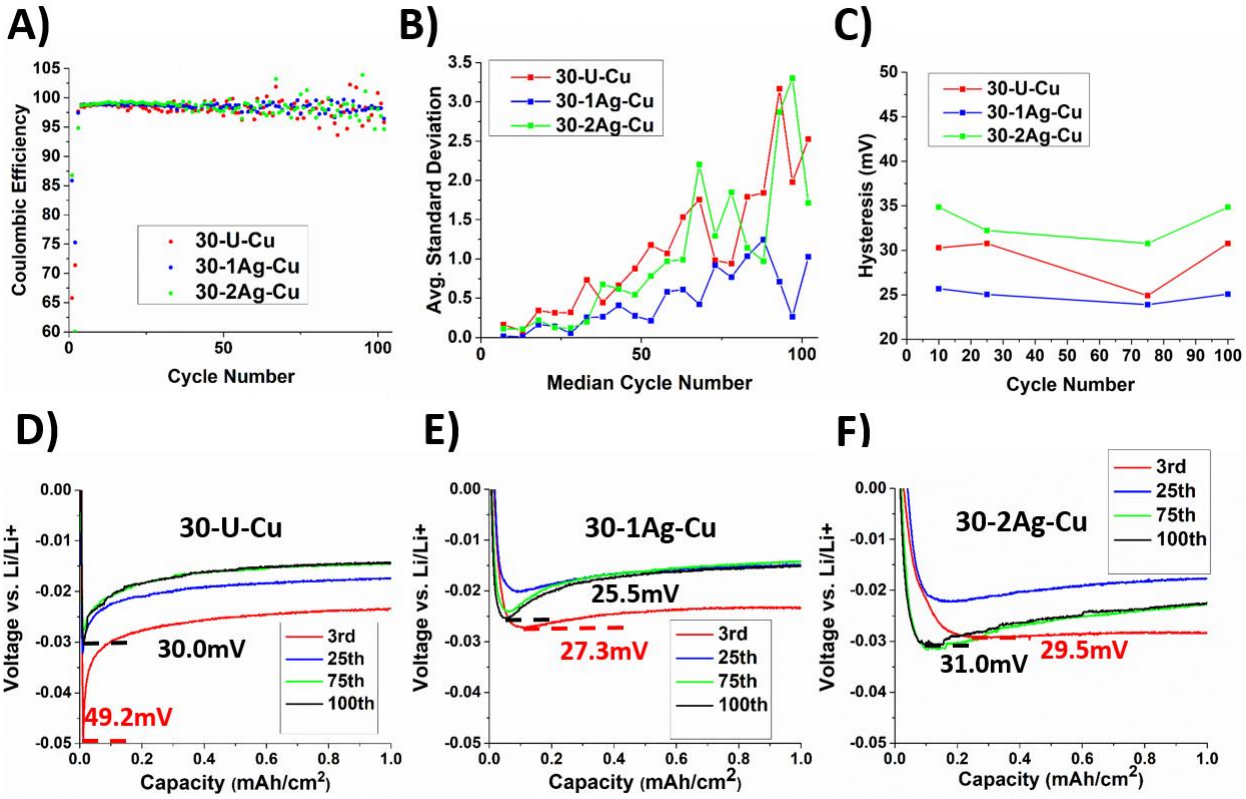

Figure 3.4. Electrochemical galvanostatic cycling of 30-Cu samples cycled at 1mA/cm^2 and 6mAh/cm^2 over 100 cycles. Plots show the A) coulombic efficiency vs. cycle number, B) the standard deviation of the CE averaged over every 5 cycles (excluding the first 3 cycles) and C) the hysteresis between plating and stripping at select cycles. For all measurements, the 30-1Ag-Cu sample show the best electrochemical performance, including longest cycle life, lowest fluctuations, and smallest hysteresis. The nucleation overpotential at various cycles for D) 30-U-Cu, E) 30-1Ag-Cu and F) 30-2Ag-Cu samples showed that the 30-1Ag-Cu sample had the lowest nucleation overpotential. This is likely because lithium plated inside the pores of the porous Cu current collector (Fig. 5D and Fig. 5E), while the other two samples had lithium plated on top of the pores.

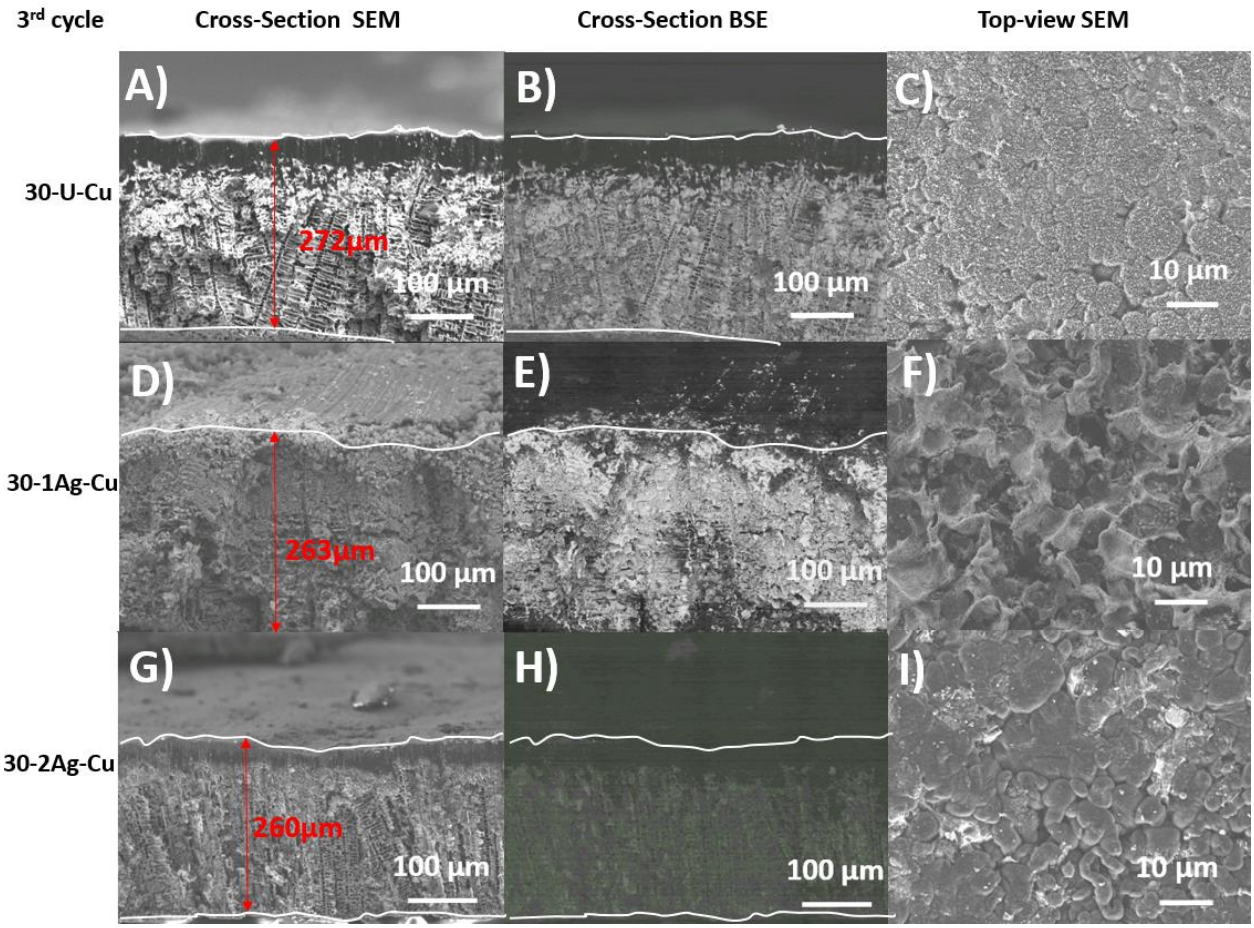

Figure 3.5. SEM images of lithium deposition in various porous Cu samples after the 3rd lithium plating cycle. Cross-sectional secondary-electron SEM image (A,D,G), cross-sectional back-scattered electron (BSE) SEM images (B,E,H), and top-view secondary-electron SEM image (C,F,I) of 30-U-Cu materials (A,B,C), of 30-1Ag-Cu materials (D,E,F) and of 30-2Ag-Cu materials (G,H,I). Cycling parameters were 1mA/cm^2 and 6mAh/cm^2 for all samples. White lines are traced on cross-sectional images to show the top and bottom edges of the cross-section. Lithium plates mostly on top of the uncoated and symmetrically coated samples, but the asymmetrically coated Cu shows Li deposition throughout the pores and porosity that is still visible at the top of the film.

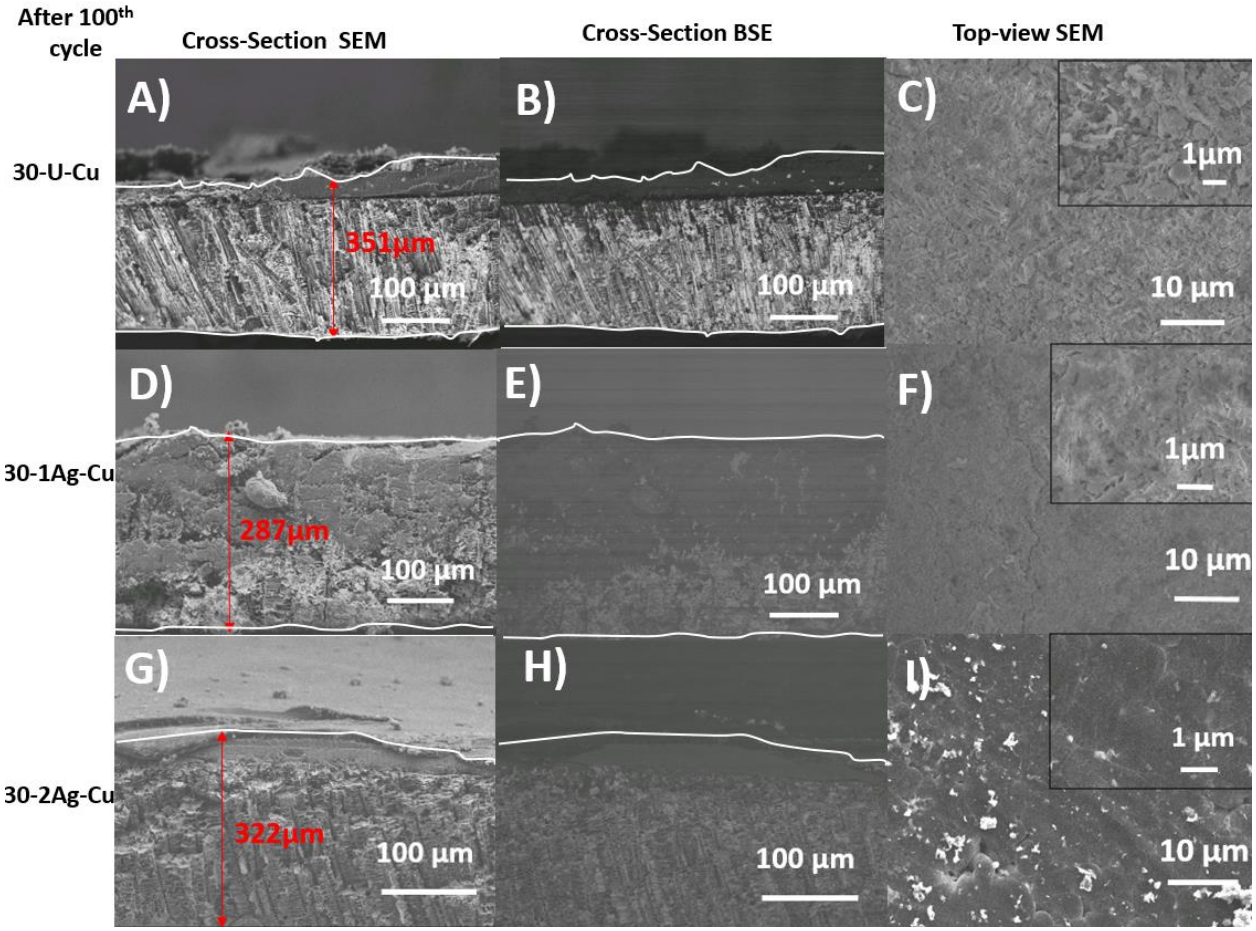

Figure 3.6. SEM images of lithium deposition in various porous Cu samples after the 100th lithium plating cycle. Cross-sectional secondary-electron SEM image (A,D,G), cross-sectional back-scattered electron (BSE) SEM images (B,E,H) and top-view secondary-electron SEM image (C,F,I) of 30-U-Cu materials (A,B,C), of 30-1Ag-Cu materials (D,E,F), and of 30-2Ag-Cu materials (G,H,I). Cycling parameters were 1mA/cm^2 and 6mAh/cm^2 for all samples. White lines are traced on cross-sectional images to show the top and bottom edges of the cross-section. Lithium plates mostly on top of the uncoated and symmetrically coated samples, as shown in the BSE SEM images (B,H) by the black band on top of the porous Cu. The asymmetrically coated sample shows Li deposition throughout the pores (E), making its overall electrode thickness (287 µm) smaller than that of the uncoated (351 µm) and symmetrically coated (322 µm) samples. Top view images corroborate these conclusions and show dendritic Li for the 30-U-Cu material (C), smooth but dense Li for the 30-2Ag-Cu sample (I), and thin Li that shows some of the top pores for the 30-1Ag-Cu material (F).

To test performance at higher lithium plating rates and higher capacity, a 30-U-Cu sample and a 30-1Ag-Cu sample were cycled at a current of 2mA/cm^2 and a capacity of 10mAh/cm^2. The CE of the 30-U-Cu suddenly dropped at the 100th cycle after being unstable for the last 20 cycles (Fig. 7A). At this higher current and capacity, the 30-1Ag-Cu sample also experienced a sudden drop below 90% after the 102nd cycle, although it experienced smaller fluctuations in the CE in the last 20 cycles than the uncoated sample (Fig. 7B). The average CE for the 30-U-Cu was 98.0% over a 100 cycle lifespan and that for the 30-1Ag-Cu was 97.8% over a 102 cycle lifespan. The potential difference between Li deposition and stripping remained lower for the 30-1Ag-Cu than for the 30-U-Cu sample but there was a sudden increase in the last 20 cycles for both samples. The instability in both samples in the last 20 cycles is likely due to accumulation of inactive Li on top of the pores, which blocks diffusion of Li into the 3D framework. It appears that at this higher current and capacity, the average pore sizes of 10μm for these samples are not big enough to allow effect diffusion into the structure. This result stands in contrast to the case when the samples were cycled at 1mA/cm^2. In addition, the increase in capacity from 6 to 10 mAh/cm^2, raises the sample's ionic resistance.[26] This favors clogging of the pores with deposited Li, making it more difficult for the asymmetric coating to facilitate Li ion deposition inside the Cu framework.

The nucleation overpotential for the 30-U-Cu sample (Fig. 7D) corroborates the idea the Li plates mostly on top of the pores. It started at a value of 42.5mV at the 10th cycle, decreased to a little below 40mV at the 25th cycle and then increased to 55.0mV at the 100th cycle. The initial slight decrease in nucleation overpotential may be due to inactive Li accumulation, which serves as a seed for further Li nucleation. The following increase in nucleation overpotential is likely due to the uneven deposition and the increasing amount of dendrite formation. Cross-sectional SEM images of Li deposited after the 103rd cycle showed that most of the Li deposited on top of the pores, with a small amount depositing inside the pores, as displayed by the black regions in the images (Fig. 8A-B). The top-view SEM image (Fig. 8C) showed dendritic morphology which may have contributed to the instability in CE in the last 20 cycles.

In contrast, the 30-1Ag-Cu sample showed more favorable behavior, despite the fact that plating became unstable after 103 cycles. A nucleation overpotential of only 35.0mV was observed at the 10th cycle, decreasing to 33.0 mV at the 25th cycle, and then retaining this value up to the 100th cycle (Fig. 7E). This stability over the first 100 cycles is due to the 'bottom-favored' Li deposition which is shown in SEM images of the sample after the 103rd cycle by the dark Li regions inside the porous framework (Fig. 8D-E). Despite the fact that Li was clearly plating inside the pores, the morphology of Li on the top of the sample still showed signs of dendrite formation (Fig. 8F). These results thus show that at 2mA/cm^2 and 10mAh/cm^2, both the uncoated and asymmetrically coated samples displayed similar lifetimes of ~100 cycles, likely due to the formation of dendritic lithium on top of both samples. However, the 30-1Ag-Cu sample retains a superior CE and stability in the last 20 cycles compared to 30-U-Cu due to fact that much of the lithium was still depositing within the pore system, rather than on top of the pores. This is

demonstrated by the smaller overall electrode thickness of the 30-1Ag-Cu (293µm) sample compared to that of 30-U-Cu (343µm) at the end of the cycling experiment (Fig. 8A and 8D).

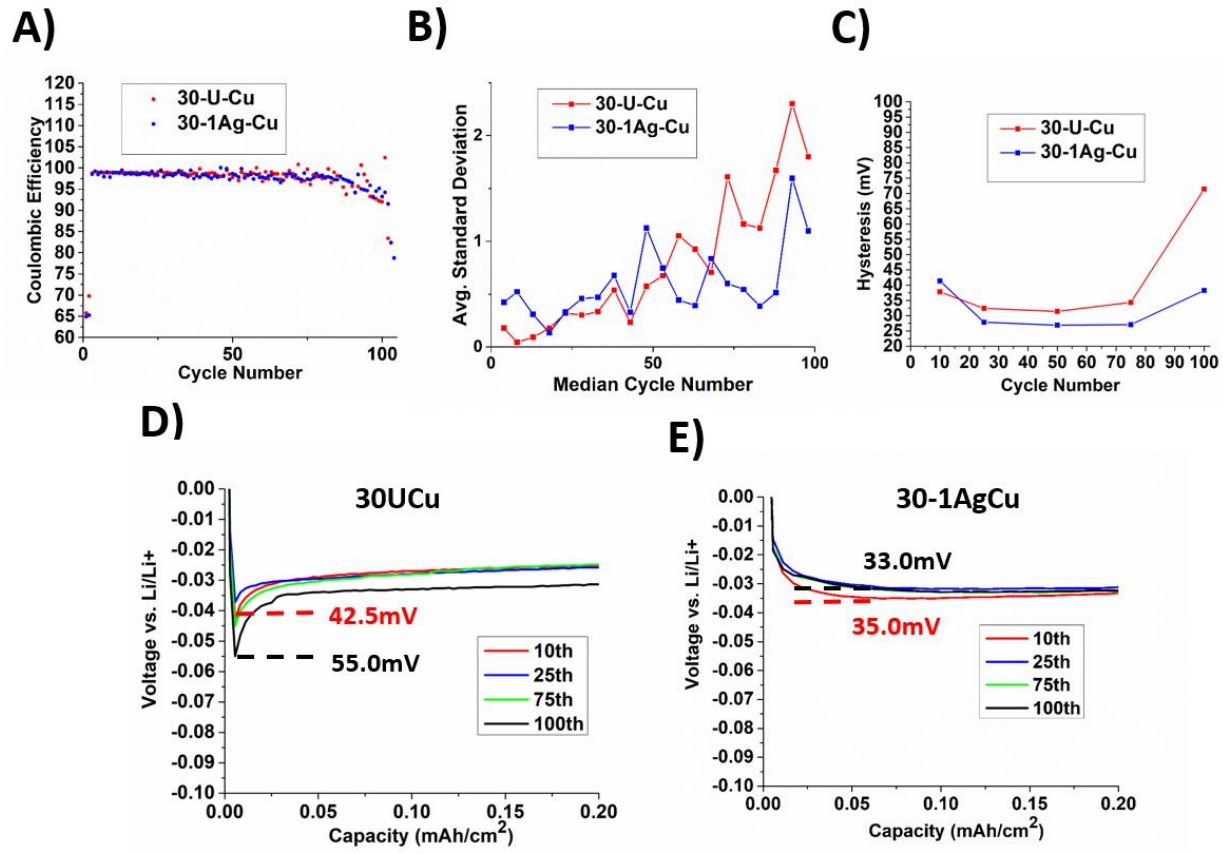

Figure 3.7. Electrochemical galvanostatic cycling of 30-Cu samples cycled at 2mA/cm^2 and 10mAh/cm^2 over 100 cycles. Plots show the A) coulombic efficiency vs cycle number, B) the standard deviation of the CE over every 5 cycles (excluding first 3 cycles) and C) the hysteresis between plating and stripping at select cycles. For all measurements, the 30-1Ag-Cu sample show the best electrochemical performance, including longest cycle life, lowest fluctuations, and smallest hysteresis. The nucleation overpotential at various cycles for the D) 30-U-Cu and E) 30-1Ag-Cu samples showed that the 30-1Ag-Cu sample had the lowest nucleation overpotential. This is likely because lithium plated inside the pores of the porous Cu current collector (Fig. 8D and Fig. 8E), while the uncoated sample had lithium plated on top of the pores.

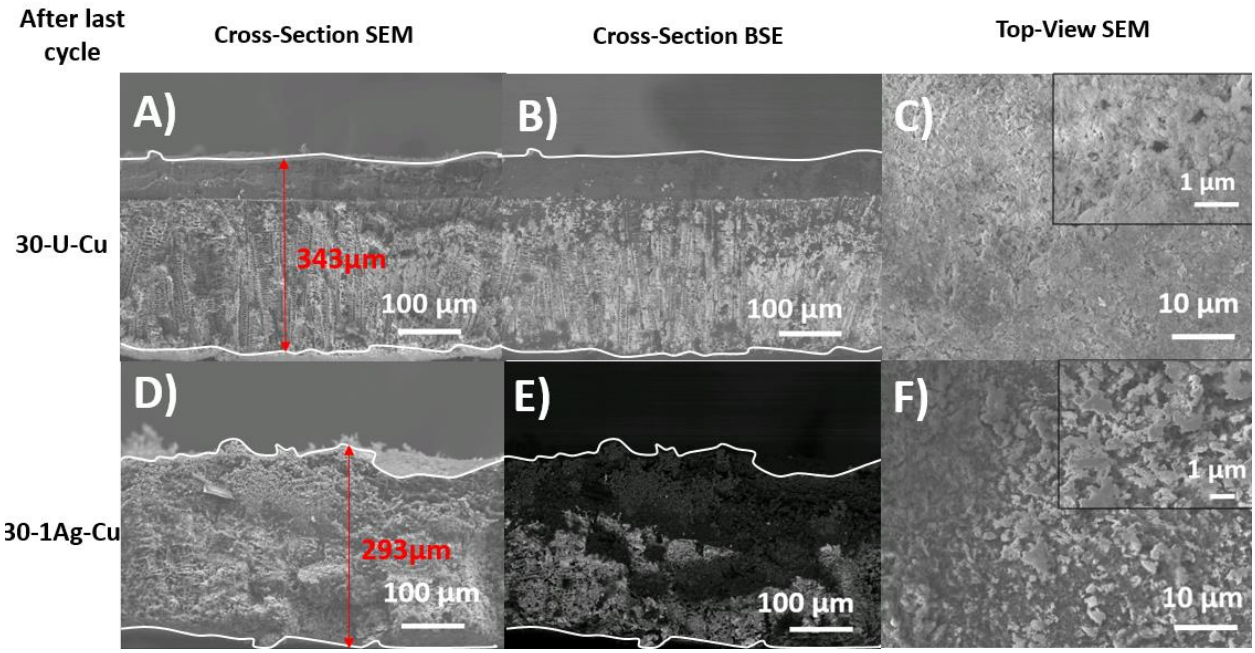

Figure 3.8. Cross-sectional secondary-electron SEM image (A,D), cross-sectional back-scattered electron (BSE) SEM images (B,E) and top-view secondary-electron SEM image (C,F) of 30-U-Cu materials (A,B,C) and of 30-1Ag-Cu materials (D,E,F). All images were collected after a Li deposition post-103rd cycle. Cycling parameters were 2mA/cm^2 and 10mAh/cm^2 for all samples. White lines are traced on cross-sectional images to show the lower and upper edges of the sample. Lithium plates mostly on top of the uncoated sample, as shown in the BSE SEM image (B) by the black band on top of the porous Cu. The asymmetrically coated sample shows Li deposition throughout the pores (E), making its overall electrode thickness (293 µm) smaller than that of the uncoated (343 µm) sample. The comparable lifetime of 102 cycles in both samples is likely due to the formation of dendritic structure in both samples.

Because it appears that the 10 µm pores of the 30-Cu samples cannot fully accommodate the high Li^+ flux associated with cycling at 2 mA/cm^2, uncoated and asymmetrically coated samples with a bigger average pores size of 14 µm (denoted as 20-U-Cu and 20-1Ag-Cu, respectively) were also tested to see how well they allow for better diffusion of Li inside the porous Cu structure. The two samples were first tested at 1mA/cm^2 and 6mAh/cm^2 for 100 cycles, which is the same modest current density and capacity used in Figure 4 for the smaller pore scaffolds. In contrast to the smaller pore materials, both the uncoated and asymmetrically coated samples showed quite small fluctuations from the average CE (Fig. 9A). This is likely because this capacity and current density could be accommodated in the near surface regime for both materials, and so the asymmetric coating did not further decrease the already very small fluctuations over the first 100 cycles (Fig. 9B). The average CE values were 98.6% and 98.5% for the 20-U-Cu sample and the 20-1Ag-Cu sample, respectively. The uncoated value is slightly higher than for the smaller pore 30-Cu counterpart under the same cycling parameters, which show CE values of 98.2% for 30-U-Cu and 98.5% for 30-1Ag-Cu. The potential difference between plating and stripping (Fig.

9C) stayed low during the 100 cycles when the asymmetrically coated 20-Cu sample was used due to the reduced R_{ct} from the lithiophilic surface. This hysteresis value was higher for the uncoated sample (Fig. 9C), and decreased as nucleation sites were formed through a lithium over-layer. The nucleation overpotential for the 20-U-Cu sample (Fig. 9D) starts at 38.5mV with a wide shape at the 10^{th} cycle and barely decreases to 36.5mV with a sharper shape during the 25^{th} through the 100^{th} cycle. This minimal change may be due to the fact that a lithium over-layer develops quickly in the top of the pore system, and then does not evolve significantly thereafter. The 20-1Ag-Cu, on the other hand, started with a low nucleation overpotential of 16.2mV at the 10^{th} cycle (Fig. 9E) but gradually increased to 24.7mV at the 100^{th} cycle. This increase is likely due to the accumulation of inactive Li, which changes the nature of the nucleating surface.

Cross-sectional SE SEM (Fig. 10A) and BSE SEM (Fig. 10B) images of the 20-U-Cu after cycling show that some Li deposited inside the porous structure, but most of it was deposited on top of the pores as demonstrated by the dark regions. From the image, the penetration may have been slightly better than in the smaller pore 30-U-Cu (Fig. 6A,B), but the results are qualitatively similar. The top-view SEM (Fig. 10C) shows a dense Li morphology which is representative of the stability of the CE of the 20-U-Cu sample over the 100 cycles. The Cross-section SE SEM (Fig. 10D) and BSE SEM (Fig. 10E) images of the 20-1Ag-Cu after cycling show that the Li deposited throughout the sample, as shown by the coverage of pores in the SE SEM and the dark regions in the BSE SEM. Furthermore, the top-view SE SEM image of 20-1Ag-Cu (Fig. 10F) shows a dense morphology after cycling, which is expected for the good electrochemical stability displayed in the other parameters. With an average CE of 98.6% for the 20-U-Cu sample and 98.5% for the 20-1Ag-Cu sample, these samples appear to show similar electrochemical performance under these parameters, which is also represented in their overall electrode thickness after cycling in Figs. 10A and 10D (258µm for the 20-U-Cu sample and 264µm for the 20-1Ag-Cu sample). Although the 20-1Ag-Cu sample shows reduced plating and stripping potential differences and nucleation overpotential, the CE fluctuations started to increase after the 30^{th} cycle likely due to inactive Li accumulation or impurities in the sample. As a result, it appears that the asymmetric coating was not as effective at improving the electrochemical performance of 20-Cu under these parameters. This is likely due to more effect ion diffusion with the lower current and larger pores.

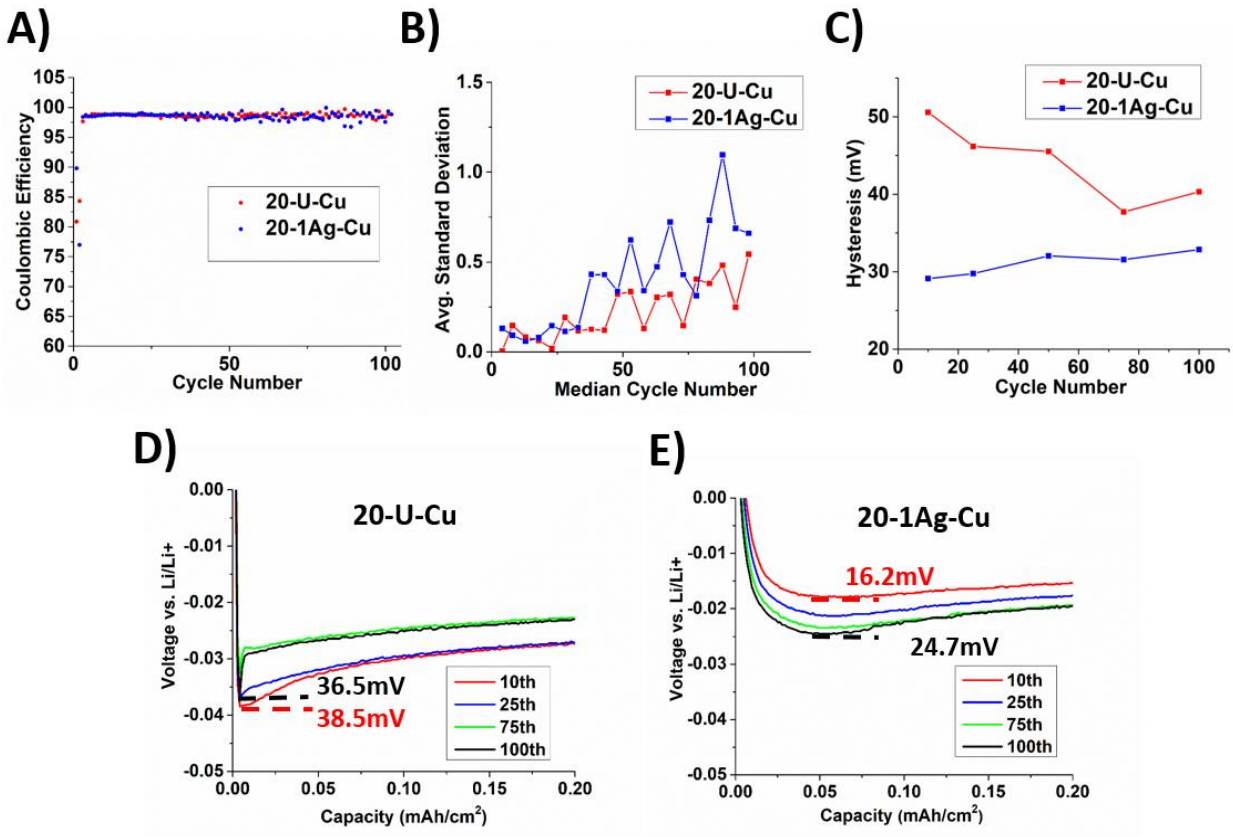

Figure 3.9. Electrochemical galvanostatic cycling for 20-Cu samples cycled at 1mA/cm^2 and 6mAh/cm^2 over 100 cycles. Plots show A) the coulombic efficiency vs. cycle number, B) the standard deviation of the CE, averaged over every 5 cycles (excluding the first 3 cycles) and C) the hysteresis between plating and stripping at select cycles. For all measurements, the 20-1Ag-Cu sample showed better electrochemical performance, including longer cycle life, lower fluctuations, and smaller hysteresis. The nucleation overpotential at various cycles for the D) 20-U-Cu and E) 20-1Ag-Cu samples showed that the 20-1Ag-Cu sample had a lower nucleation overpotential. This is likely because lithium plated inside the pores of the porous Cu current collector (Fig. 10D and Fig. 10E), while the uncoated sample had lithium plated on top of the pores.

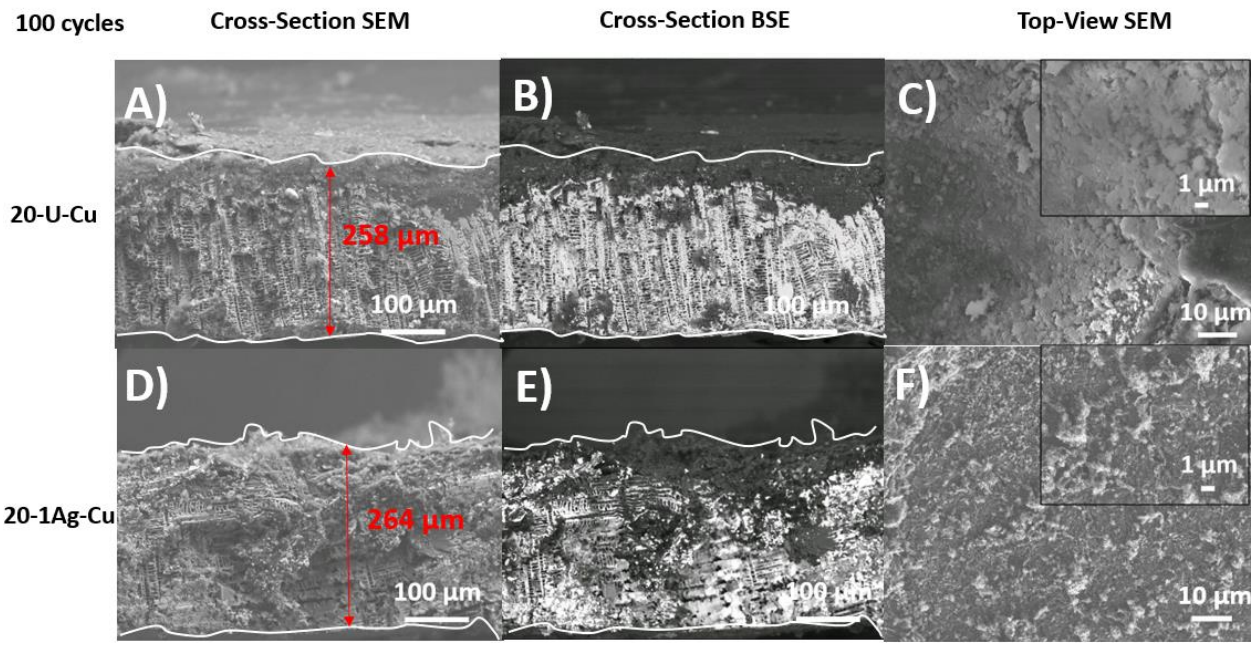

Figure 3.10. Cross-sectional secondary-electron SEM image (A,D), cross-sectional back-scattered electron (BSE) SEM images (B,E) and top-view secondary-electron SEM image (C,F) of 20-U-Cu materials (A,B,C) and of 20-1Ag-Cu materials (D,E,F). All images were collected after a Li deposition post-100nd cycle. Cycling parameters were 1mA/cm^2 and 6mAh/cm^2 for all samples. White lines are traced on cross-sectional images to show the lower and upper edges of the sample. Lithium plates mostly on top of the uncoated sample with some Li going inside the pores, as shown in the BSE SEM image (B). The asymmetrically coated sample shows Li deposition further inside the pores (E). The overall electrode thickness of 20-U-Cu (258 µm) is comparable to that of 20-1Ag-Cu (264 µm), which is representative of the similar electrochemical performance of both samples. This may be due to the large avg. pore size of 14µm that allows Li to deposit further into the uncoated sample, while making the effect of asymmetric coating on 20-1Ag-Cu less effective under these testing parameters.

To accentuate the performance differences between the uncoated and asymmetrically coated samples, the 20-U-Cu sample and the 20-1Ag-Cu sample were cycled at higher currents and total capacities of $2mA/cm^2$ and $10mAh/cm^2$. The fluctuations from the average CE in the 20-U-Cu sample were much higher than for that in the 20-1Ag-Cu sample over most of the cycling period (Fig. 11A). The 20-1Ag-Cu sample showed a superior lifespan with an average CE of 97.8% over 128 cycles, which was significantly longer than the 20-U-Cu sample, which showed and average CE of 98.1% over 83 cycles before the CE dropped below 90%. The CE fluctuations of the uncoated sample increased quite a bit after the 60^{th} cycle but that of the asymmetrically coated sample remained low all the way through the 100^{th} cycle (Fig. 11B). The fluctuations are likely due to the accumulation of dead Li on top of the pores of the uncoated sample. The potential difference between deposition and stripping for the 20-U-Cu sample started high and decreased for the first 50 cycles as a dense Li nucleation layer built up. The value then started to increase as lithium dendrites formed until the cell shorted after 80 cycles (Fig. 11C). The 20-1Ag-Cu sample, in contrast, started with a much lower hysteresis value (Fig. 11C) and showed a slightly increasing trend in potential difference between deposition and stripping, although the absolute value stayed low, even at 100 cycles. The nucleation overpotential for the uncoated sample started at a relatively high value of 42.0mV at the 10^{th} cycle and progressively increased to 44.5mV at the 100^{th} cycle (Fig. 11D). In contrast, the nucleation overpotential of the asymmetrically coated sample started at 22.5mV at the 10^{th} cycle and increased only up to 29.5mV at the 100^{th} cycle (Fig. 11E). The reduced charge transfer resistance inside the pores of the 20-1Ag-Cu sample allowed for more electrochemical stability, as reflected by the small CE fluctuations, low potential difference between deposition and stripping, and the reduced nucleation overpotential throughout cycling.

After the 100^{th} cycle, the 20-U-Cu sample shows a thick Li layer on top of the porous Cu, as shown by the dark strip in both the SE SEM image (Fig. 12A) and the BSE SEM image (Fig. 12B). The top-view SE SEM (Fig. 12C) shows a dendritic morphology, which was expected, given that the cell had already shorted after the 80^{th} cycle. The SE SEM image (Fig. 12D) and the BSE SEM image (Fig. 12E) of the 20-1Ag-Cu sample after the 128^{th} cycle showed that Li deposited both inside the pores and on top of the porous structure, as shown by the large dark regions in the images. The Li morphology after cycling (Fig. 12F) retained a dense aspect, aligning well with its superior electrochemical performance. In addition, the upper edge borderline of the 20-1Ag-Cu sample's cross-section after 128 cycles is more compact and the overall electrode thickness thinner (347 µm) than that of the 20-U-Cu sample (435 µm after 100 cycles). The physical characteristics that helped to increase the 20-1Ag-Cu sample's lifetime under these conditions are their bigger pore size, and lower tortuosity relative to that of the 30-1Ag-Cu sample, which facilitates the Li diffusion inside the Cu structure. This resulted in low CE fluctuations, the small difference between deposition and stripping potential, the reduced nucleation overpotential and the 'bottom-up' Li deposition due to reduced R_{ct}.

Uncoated, asymmetrically coated and symmetrically coated 30-Cu and 20-Cu samples were also cycled at $4mA/cm^2$ and $10mAh/cm^2$. Under these parameters (Fig. S8 and Fig. S9), the 30-1Ag-Cu showed a superior lifetime (53 cycles) and average CE over its lifespan (98.6%)

compared to that of the 30-U-Cu sample (98.0% over 43 cycles) and 30-2Ag-Cu sample (96.6% over 39 cycles). For the case of the 20-Cu samples under these parameters (Fig. S10 and Fig. S11), the 20-1Ag-Cu outperformed all the other samples in terms of lifetime, but its average CE decayed significantly over its lifespan (96.9% over 81 cycles). The 20-U-Cu sample and 20-2Ag-Cu samples both had shorter lifespans (average CE of 97.4% over 73 cycles and 97.3% over 18 cycles, respectively).

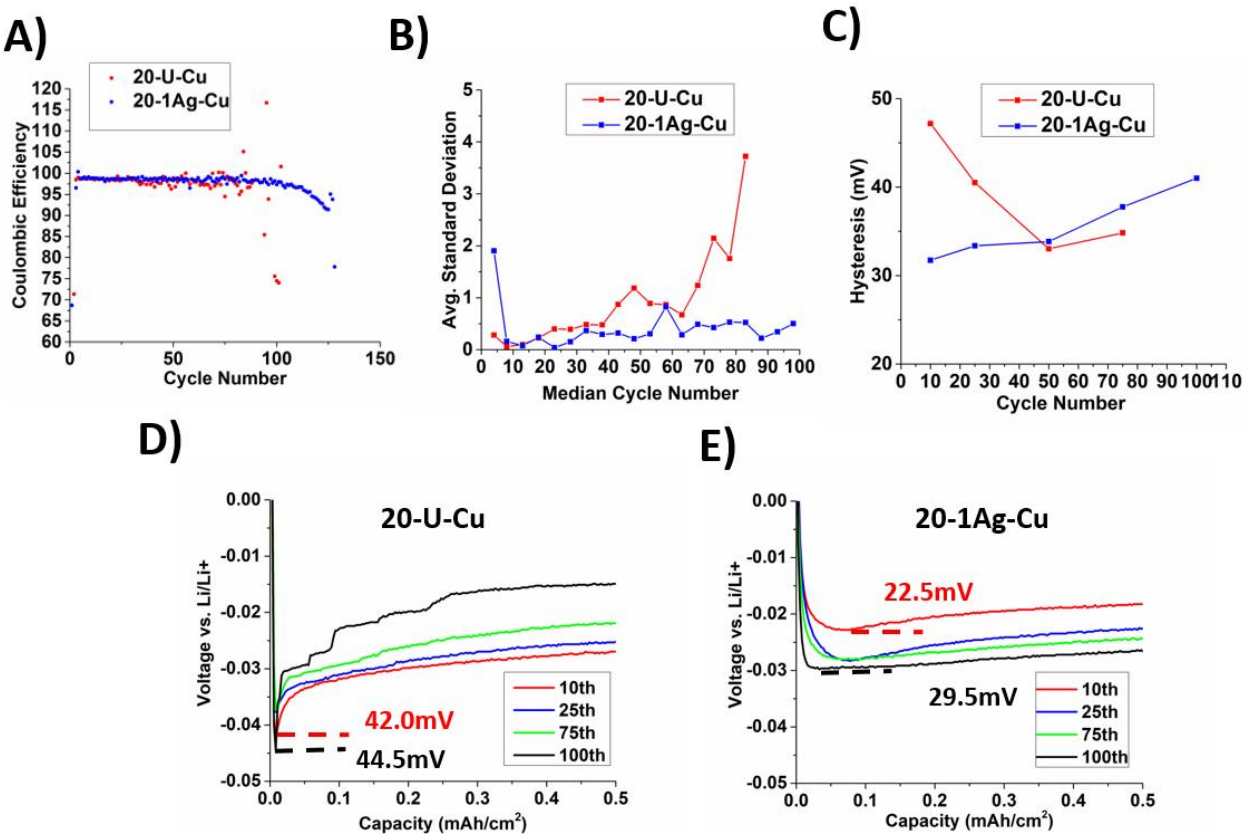

Figure 3.11. Electrochemical galvanostatic cycling of 20-Cu samples cycled at 2mA/cm^2 and 10mAh/cm^2 over 100 cycles. Plots show the A) coulombic efficiency vs cycle number, B) the standard deviation of the CE over every 5 cycles (excluding the first 3 cycles) and C) the hysteresis between plating and stripping at select cycles. For all measurements, the 20-1Ag-Cu sample show the best electrochemical performance, including longest cycle life, lowest fluctuations, and smallest hysteresis. The nucleation overpotential at various cycles for the D) 20-U-Cu and E) 20-1Ag-Cu samples showed that the 20-1Ag-Cu sample had the lowest nucleation overpotential. This is likely because lithium plated inside the pores of the porous Cu current collector (Fig. 12D and Fig. 12E), while the uncoated sample had lithium plated on top of the pores.

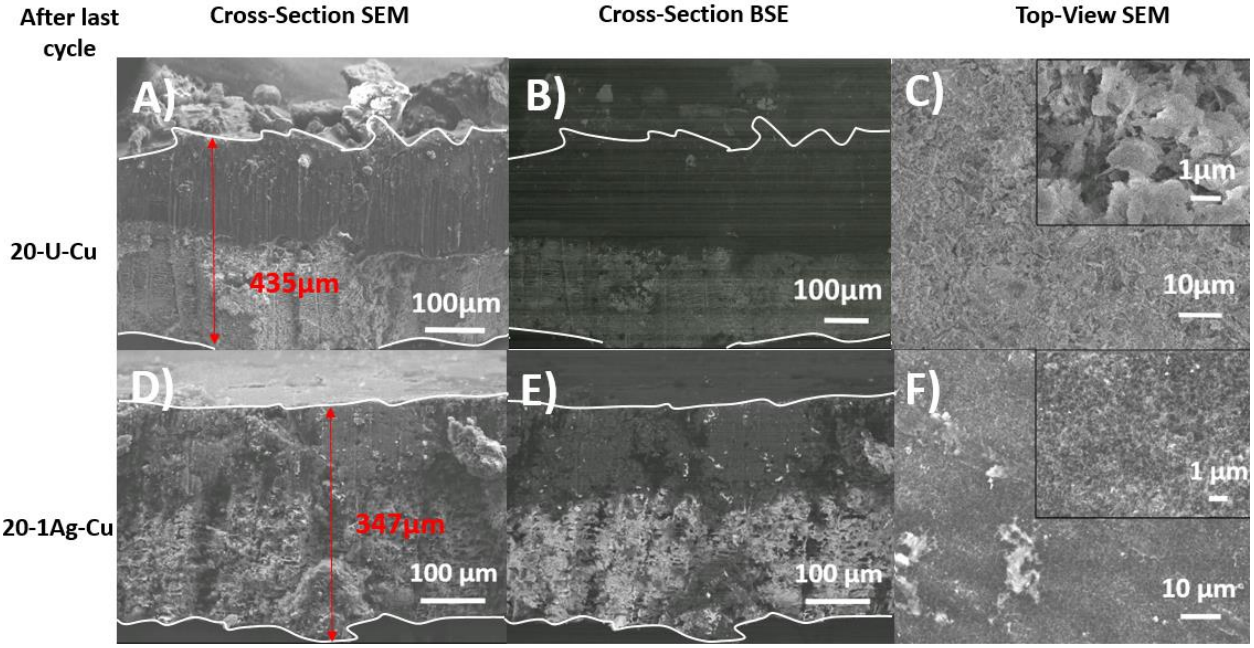

Figure 3.12. Cross-sectional secondary-electron SEM image (A,D), cross-sectional back-scattered electron (BSE) SEM images (B,E) and top-view secondary-electron SEM image (C,F) of 20-U-Cu materials (A,B,C) and of 20-1Ag-Cu materials (D,E,F). The images for the 20-U-Cu sample were collected after a Li deposition post-100th cycle. The images for the 20-1Ag-Cu sample were collected after a Li deposition post 128th cycle. Cycling parameters were 2mA/cm^2 and 10mAh/cm^2 for all samples. White lines are traced on cross-sectional images to show the lower and upper edges of the sample. Lithium plates mostly on top of the uncoated sample, as shown in the BSE SEM image (B). The asymmetrically coated sample shows Li deposition further inside the pores (E). The overall electrode thickness of 20-U-Cu (435µm) after the 100th cycle is much higher than that of 20-1Ag-Cu (347 µm) after the 128th cycle, which is representative of the superior electrochemical performance of the 20-1Ag-Cu sample under these testing parameters.

In making sense of all of these trends, it is worth noting that the same facile diffusion that allows for easier diffusion of Li^+ into the pores to facilitate high rate charging, likely also applies to Ag^+. As a result, it should be harder to produce a steep gradient in the Ag coating in the 20-1Ag-Cu than in the 30-1Ag-Cu material. The shallower gradient should allow more Li to plate on top of the 20-1Ag-Cu than on top of the 30-1Ag-Cu. This fact points to a fundamental challenge of this method. The beauty of the gradient coating method presented in this work is its simplicity, but that creates a fundamental contradition between the need for some diffusion limitations to produce a gradient, and the need for minimal diffusion limitations to facilitate Li plating deep within the porous scaffold. Fortunately, these diffusion constrains are not identical in rate or spatial distribution, and so significant optimization is clearly possible. More importantly, a key

conclusion of the work is that if steep gradients in lithophilic coatings could be produced in large pore scaffolds, nearly ideal, dendrite free Li plating and stripping should be possible.

3.4. Conclusion

This work presents a strategy to optimize the performance of high-capacity 3D current collectors using a lithiophilic Ag coating gradient. Utilizing 3D Cu frameworks with pore sizes of 10µm (30-Cu) and 14 µm(20-Cu), it was found that by asymmetrically coating the 3D frameworks Li was able to deposit all the way down to the bottom of the scaffold. This was contrasted to uncoated Cu samples or uniformly Ag-coated Cu samples, where lithium mostly deposited on top of the porous scaffold. The cycling stability of these Cu frameworks with different surface chemistries were tested at 1mA/cm^2 and 6mAh/cm^2, 2mA/cm^2 and 10mAh/cm^2, and 4mA/cm^2 and 10mAh/cm^2. For the case of low current density and capacity (1mA/cm^2 and 6mAh/cm^2), the smaller pore 30-1Ag-Cu materials performed much better than either the uncoated or the homogeneously coated scaffolds. The gradient-coated materials show stable cycling with low overpotentials and low hysteresis between plating and stripping; more importantly, it showed full plating of Li deep within the pores. In contrast, both the larger pore 20-U-Cu and 20-1Ag-Cu materials showed good electrochemical performance over 100 cycles. Due to the large average pore sizes and low tortuosity, the 20-U-Cu already performs well without much improvement when asymmetrically coated. At faster rates and higher capacities of 2mA/cm^2 and 10mAh/cm^2, however, the 20-1Ag-Cu clearly showed better electrochemical performance, with much improved cycle life compared to the uncoated version of the same scaffold. The ability to perform well at high rate is mainly due to its bigger pore size and lower tortuosity compared to the 30-Cu sample, which reduces the resistance to Li^+ diffusion into the pores. Lastly, at the highest current of 4mA/cm^2 (10mAh/cm^2), the 20-1Ag-Cu sample clearly has the longest lifespan of the samples with 81 cycles before the CE began to drop, but even for the large pore material did not allow for enough Li^+ diffusion to facilitate very long stable cycling at the highest rates.

While a range of behaviors can be observed, depending on the current density and total capacity, the key result of this work is the fact that a gradient lithophilic coating can be used to overcome the gradient in ionic conductivity that always arises in porous hosts. The successful application of this idea prevents a key problem with the use of lithophilic coatings, which is the formation of thick Li overlayers that completely bypass the pore system. This design idea of a gradient in lithiophilic coating should be helpful to further improve the lifetime and stability of other high-capacity 3D current collectors while decreasing the possibility of having dendrite formation.

3.5. References

(1) Cai, M.; Dai. F.; Chen, S. Opportunities and Challenges of High-Energy Lithium Metal Batteries for Electric Vehicle Applications. ACS Energy Lett. 2020, 5, 3140-3151.

(2) Fang, C.; Wang, X.; Meng, Y. S. Key Issues Hindering a Practical Lithium-Metal Anode. *Trends Chem.* 2019, 1, 152–158.

(3) Fang, C.; Li, J.; Zhang, M.; Zhang, Y.; Yang, F.; Lee, J. Z.; Lee, M.; Alvarado, J.; Schroeder, M. A.; Yang, Y.; Lu, B.; Wiliams, N.; Ceja, M.; Yang, L.; Cai, M.; Gu. J; Xu, K.; Wang, X. and Meng, Y. S. Quantifying inactive lithium in lithium metal batteries. *Nature* **572**, 511–515 (2019).

(4) Yan, J.; Yu, J.; Ding, B. Mixed Ionic and Electronic Conductor for Li-Metal Anode Protection. Adv.Mater. 2018, 30, 1705105.

(5) Wu. K. et al. Polycationic Polymer Layer for Air-Stable and Dendrite-Free Li Metal Anodes in Carbonate Electrolytes. *Adv. Mater. 2021, 33, 2007428.*

(6) Zheng, H.; Xiang, F.; Jiang, Y.; Liu, Y.; Sun, X.; Liang, Y.; Feng, Y.; Yu, Y. Lithium Difluorophosphate-Based Dual-Salt Low Concentration Electrolytes for Lithium Metal Batteries. Adv. Energy Mater.2020, 10, 2001440.

(7) Yang, Y.; Yin, Y.; Davies, D. M.; Zhang, M.; Mayer, M.; Zhang, Y.; Sablina, E. S.; Wang, S.; Lee, J. Z.; Borodin, O.; Rustomji, C. S.; Meng, Y. S. Liquefied gas Electrolytes for Wide-Temperature Lithium Metal Batteries. Energy Environ. Sci., 2020, 13, 2209-2219.

(8) Choudhury, S.; Stalin, S.; Vu, D.; Warren, A.; Deng, Y.; Biswal. P.; Archer, L. A. Solid-State Polymer Electrolyte for High-Performance Lithium Metal Batteries. *Nat. Commun*. 2019, 10.

(9) Cheng, X. et al Recent Advances in Energy Chemistry between Solid-State Electrolyte and Safe Lithium-Metal Anodes. *Chem*, 2019, 5, 74-96.

(10) Kai, Y.; Lu, Z.; Lee, H.; Xiong, F.; Hsu, P.; Li, Y.; Zhao, J.; Chu, S.; Cui, Y. Selective deposition and stable encapsulation of lithium through heterogeneous seeded growth. *Nat. Energy*, 2016, 1.

(11) Zhu, Z.; Wang, Z.; Liu, S.; Li, G. Gao, X. Uniform lithium plating within 3D Cu foam enabled by Ag nanoparticles. *Electrochim. Acta*, 2021, 379, 138152, 0013-4686.

(12) Wu, Q.; Qin, M.; Yan, H.; Zhong, W.; Zhang,W.; Liu, M.; Cheng, S.; Xie, J. Facile

Replacement Reaction Enables Nano-Ag Decorated Three-Dimensional Cu Foam as High-Rate Lithium Metal Anode. *ACS Appl. Mater. Interfaces,* **2022,** *14* (37), 42030-42037.

(13) Wang,J.; Wang, M.; He, X.; Wang, S.; Dong, J.; Chen, F.; Yasmin, A.; Chen, C. A. Lithiophilic 3D Conductive Skeleton for High Performance Li Metal Battery. ACS Appl. Energy Mater. **2020,** 3 (8), 7265-7271.

(14) Yu Ye, Yutao Liu, Jiliang Wu, Yifu Yang, Lithiophilic Li-Zn alloy modified 3D Cu foam for dendrite-free lithium metal anode. *J. Power Sources*, 2020, 472, 228520, 0378-7753.

(15) Kim, S.; Kim, Y.; Nguyen, C.; Jang, T.; Lee, H.; Byon, H. R. Promoting lithium electrodeposition towards the bottom of 3-D copper meshes in lithium-based batteries. *J. Power Sources*, 2020, 472, 228495, 0378-7753.

(16) Pei, A., Zheng, G., Shi, F., Li, Y. & Cui, Y. Nanoscale Nucleation and Growth of Electrodeposited Lithium Metal. *Nano Lett.* 17, 1132–1139 (2017).

(17) Liu, L.; Yin, Y.; Li, J.; Wang, S; Guo, Y. Wan, L. Uniform Lithium Nucleation/Growth Induced by Litghtweight Nitrogen-Doped Graphitic Carbon Foams for High Graphitic Carbon Foams for High-Performance Lithium Metal Anodes. *Adv.Mater*, 2018, 30, 1706216.

(18) Zhang, Y.; Luo, W.; Wang, C.; Li, Y.; Chen, C.; Song, J.; Dai, J.; Hitz, E. M.; Xu, S.; Yang, C.; Wang, Y. Hu, L. High-capacity, low-tortuosity, and channel-guided lithium metal anode. PNAS, 2017, 114, 3584-3589.

(19) Chi, S.; Liu, Y.; Song, W.; Fan, L.; Zhang, Q. Prestoring Lithium into Stable 3D Nickel Foam Host as Dendrite-Free Lithium Metal Anode. *Adv. Funct. Mater.* 2017, 27, 1700348.

(20) Yun, Q., He, Y.-B., Lv, W., Zhao, Y., Li, B., Kang, F. and Yang, Q.-H. (2016), Chemical Dealloying Derived 3D Porous Current Collector for Li Metal Anodes. *Adv. Mater*., 28. 6932-6939.

(21) Yun, Q., He, Y.-B., Lv, W., Zhao, Y., Li, B., Kang, F. and Yang, Q.-H. (2016), Chemical Dealloying Derived 3D Porous Current Collector for Li Metal Anodes. Adv. Mater., 28: 6932-6939.

(22) Hafez, A. M.; Jiao, Y. Shi, J.; Ma, Y.; Cao, D.; Liu, Y.; Zhu, H. Stable Metal Anode enabled by Porous Lithium Foam with Superior Ion Accessibility. *Adv. Mater*. 2018, 20,

1802156.

(23) Zhan, Y.; Shi, P.; Zhang, X.; Ding, F.; Huang, J.; Jin, Z.; Xiang, R.; Liu, X. Zhang, Q. The Insights of Lithium Metal Plating/Striping in Porous Hosts: Progress and Perspectives. *Energy Technol*, 2021, 9, 2000700.

(24) Ogihara, N.; Itou, Y.; Sasaki, T.; Takeuchi, Y. Impedance Spectroscopy Characterization of Porous Electrodes under Different Electrode Thickness Using a Symmetric Cell for High-Performance Lithium-Ion Batteries. *J. Phys. Chem. C*. **2015,** 119 (9), 4612-4619.

(25) Ju, Z.; Zhang, X.; Wu, J.; King, S. T.; Chang, C.; Yan, S.; Xue, Y.; Takeuchi, K. J.; Marschilok, A. C.; Wang, L.; Takeuchi, E. S.; Yu, G. Tortuosity Engineering for Improved Charge Storage Kinetics in High-Areal-Capacity Battery Electrodes. Nano Lett. ***2022***, 22 (16), 6700-6708.

(26) Wu, J.; Ju, Z.; Zhang, X.; Marschilok, A. C.; Takeuchi, K. J.; Wang, H.; Takeuchi, E. S.; Yu, G. Gradient Design for High-Energy and High-Power Batteries. *Adv. Mater.* 2022, 2202780.

(27) Lu, B.; Olivera, E.; Scharf, J.; Chouchane, M.; Fang, C.; Ceja, M.; Pangilinan, L.; Zheng, S.; Dawson, A.; Cheng, D.; Bao, W.; Arcelus, O.; Franco, A. A.; Li, X.; Tolbert, S. H.; Meng, Y. S. Quantitatively Designing Porous Copper Current Collectors for Lithium Metal Anodes. ACS Appl. *Energy Mater*. 2021, 4, 6454-6465.

Chapter 4: Mesoporous, Dealloyed Copper Catalysts for the Electrochemical Reduction of Carbon Dioxide

4.1 Introduction

The electrochemical reduction of carbon dioxide (CO_2R) to useful fuels and chemicals is of interest for its promise in producing carbon-neutral chemicals of value, such as ethylene and ethanol.[1] With continually decreasing solar and wind electricity prices [2], the development of an economical CO_2R conversion system relies on the efficiency and scalability of the catalyst material itself. Finding a catalyst material that can provide a high production yield of C_{2+} products and can be made in large scale is crucial for a sustainable future.[3] Beyond the catalyst, reactors capable of operating at industrially relevant reaction rates (>100 mA/cm^2) with gas diffusion electrodes[4] (GDE) and membrane electrode assemblies[5] (MEA) are vital to displacing current petrochemical processes. Of catalyst materials, copper (Cu) is unique in its ability to form hydrocarbons and alcohols from CO_2[6] facilitating the formation of C_{2+} products. Cu possesses a wide product distribution, with up to a dozen multi-carbon products reported from a single foil.[7] Consequently, steering CO_2R selectivity to *specific* desirable products is a significant challenge requiring a detailed understanding of reaction mechanisms, electrolyte engineering, and altering catalyst composition.[8]

Porosity serves as a physical mechanism for catalyst layer modification. For example, a mesoporous Sn/SnO_2 catalyst[9] was shown to enhance formate and carbon monoxide production on a nickel-nitrogen-doped carbon catalyst. Even in a nanoporous system, optimized porosity is still effective in improving mass transport, with such an effect being shown on nanoporous gold[10] and 3D porous silver[11] in CO_2R and cobalt oxide in oxygen electrochemistry (ORR/OER).[12] While porosity increases the surface area of the catalyst material and, thus, its catalytic sites,[13] CO_2 reduction higher-reduced products (C_{2+}) are more prone to increase due to the higher number of grain boundaries[14,15] and lattice defect density.[16,17]

Catalyst layers can also be modified through composition of active material, and bimetallic systems are a promising approach to modifying composition.[18] Bimetallic catalysts involving Cu and a carbon monoxide (CO)-producing catalyst (gold, silver)[19, 20, 21] have been investigated to achieve a "tandem" effect of CO production on gold/silver sites and CO reduction on Cu sites. This can result in enhanced alcohol production at lower overpotentials for dilute amounts of gold on a copper surface[22] and tandem copper/silver nanoparticles producing industrially relevant amounts of C_{2+}products in a vapor-fed electrolyzer.[23] Bimetallic effects extend beyond tandem catalysis with a second active metal to materials with dilute amounts of aluminum in a Cu-based alloy catalyst being an interesting example of this. A combined theoretical and experimental analysis indicating that copper alloyed with dilute amounts of aluminum at certain surface locations has a unique ability to produce larger amounts of C_{2+} products than Cu alone or other alloys by facilitating CO dimerization.[24]

Dealloying is a scalable method used to create porous materials[25,26], including porous Cu catalysts. Particularly, Cu-Al alloys with less than 33at% Cu are a two-phase eutectic containing Al and $CuAl_2$, and can be used to make porous Cu with dilute amounts of Al.[27] Interestingly, the

precursor alloy composition can be used to tune the pore size, pore size distribution and surface area. During dealloying, all of the Al dissolves, and Al is etched out of the Al-rich α-phase. The Al domains leave behind macropores approximately tens of microns in size while the intermetallic θ phase leaves behind nano-sized mesopores upon dealloying, creating a hierarchical mesoporous-macroporous structure.[28]

Increasing the Cu content in the precursor alloy increases the density of mesopores and surface area upon dealloying. A dealloyed version of this system, with excess Al etched in hydrochloric acid, was shown to exhibit enhanced mesoporosity, producing ethylene with a high selectivity of over 80 percent.[29] This fabrication scheme provides two particular advantages for CO_2R electrolyzers. First, conversion of active material to a powder form provides facile integration with conventional GDE fabrication techniques.[30] Second, tandem catalytic effects are easily implemented through coating of a CO-promoting active material (Ag, Au) via galvanic displacement due to the nobility of these metals.[31-33]

In this work, mesoporous Cu powder made by dealloying a Cu-Al alloy within the eutectic system, are integrated with a gas diffusion electrode for use in a membrane electrode assembly (MEA). Catalyst surface area and pore size distributions are tuned by changing the compositional parameters within the eutectic region of the Cu-Al system, with an increase in surface area observed with increasing Cu content in precursor alloy. Samples with varying compositional content (10-22 atomic percent Cu in precursor alloy) were tested electrochemically to observe trends in production of higher-reduced products, with increasing surface area facilitating a 31.5% increase in geometric current density and a 52.6% increase in ethylene selectivity across compositional range. Tandem catalysis was demonstrated through coating powders in dilute amounts of either Au or Ag, with Ag-coated Cu showing combined production rates of ethylene and ethanol of -102.44 mA/cm^2 at a full-cell voltage of -4 V; a 14.5% improvement over-the same powder without coating at 500 mV higher cell potential.

4.2 Experimental

1) Alloy Fabrication and Dealloying Process:

Cu shots (Alfa Aesar,1-10mm 99.9% metal basis) and Al metal granules (Alfa Aesar, 8-12 mm, 99.9% metal basis) were used to prepare Cu–Al alloys with three different compositions: 10 atomic percent (at%) Cu–90 at% Al (hypoeutectic), 17.5 at% Cu–82.5at%Al (eutectic), and 22at %Cu–78at %Al (hypereutectic). Each composition had about 1at% excess of Al to make up for evaporated Al. About 120g of each composition was loaded into a graphite crucible and heated in an Argon-filled furnace at 800 °C for 1 h, followed by slow cooling down to room temperature. An alloy rod of about 10cm in height and 3cm in diameter with uniform composition was obtained for each sample. Each of the three samples was sliced and polished using sandpaper to make samples of about 500μm in thickness. The samples were then dealloyed in 5wt% HCl acid solution at 75°C under constant stirring until bubbling stopped. The dealloyed samples were broken into powder towards the end of the dealloying process to make sure that the internal parts of the 3D structure are dealloyed. This was followed by a pure acetone (ACS reagent >99.5% pure) and 200 proof ethanol wash to clean off remaining contaminants. Finally,

the cleaned samples were dried under vacuum for 1 h and immediately stored under Argon environment.

2) Ag and Au Coating by Galvanic Displacement:

The hypoeutectic and eutectic samples were Ag-coated by immersing the as-dealloyed porous Cu powder in a 1.2mM $AgNO_3$ (Alfa Aesar, 99.95% metal basis) and 0.3mM Citric Acid (VWR, ACS grade) in ethanol solution under sonication for 1hr and 1.5hrs., respectively. The hypereutectic samples were Ag-coated by immersing the as-dealloyed porous Cu powder in a 2.4mM $AgNO_3$ (Alfa Aesar, 99.95% metal basis) and 0.3mM Citric Acid Monohydrate (VWR, ACS grade) in 200 proof ethanol solution under sonication for 2hrs. The hypoeutectic, eutectic and hypereutectic samples were Au-coated by immersing the as-dealloyed mesoporous Cu powder in a 1 mM $HAuCl_4$ (BTC, 99.999% trace metal basis) aqueous solution for 40min, 1hr and 2hrs., respectively. Every sample was then cleaned with three washes of pure acetone (ACS reagent >99.5% pure), dried under vacuum for 1hr. and immediately stored under Argon environment.

3) Gas diffusion electrode fabrication:

Dealloyed porous Cu powder was suspended in an ink by taking 50 mg of dealloyed porous Cu powder combined with 5 weight percent Nafion, dispersed in 5 mL of solvent (40% v/v isopropanol/water). The ink was sonicated in an ice bath using an ultrasonic tip sonicator (QSonica) for at least 20 minutes. The ink was manually sprayed onto a gas diffusion layer (Sigracet 39 BB) using an airbrush (Paasche VLST-3) connected to a N_2 gas line with an outlet pressure ranging from 5-10 psi during the process of spraying. Electrodes were weighed before and after spraying to determine loading, with catalyst loading calculated as $\frac{.95\times(final\ mass)-(initial\ mass)}{geometric\ area}$, with a target loading of 1 mg/cm^2. In the event of insufficient loading (< 0.5 mg/cm^2) after completing this process, the process was repeated an additional time to acquire sufficient loading.

4) Membrane electrode assembly:

The membrane electrode assembly was formed through cathodes as described above, combined with a Sustainion X37-50 RT membrane (Dioxide Materials) and a commercial iridium oxide (IrO_2) on carbon paper anode (Dioxide Materials). These components were sandwiched into a 5 cm^2 electrolyzer (Fuel Cell Technologies) with .010" gaskets used to restrict the active area to 1cm^2. A torque wrench was used to apply 40 lb·in of torque to each bolt to complete assembly.

5) System operating parameters:

Cell temperature was kept at 25 ˚C using a heating element (Fuel Cell Technologies). 0.1 M potassium bicarbonate anolyte was fed on the anode, with a flow rate of 5 mL/min set using a peristaltic pump (Ismatec Reglo ICC). On the cathode, CO_2 (Praxair, 99.999%) was fed through a needle valve and 0.1 M $KHCO_3$ bubbler, with the cathode outlet connected to a miniature deionized water bubbler (Sigma-Aldrich, 4mL) in an ice bath for collection of liquid products

accumulated on the cathode, along with a desiccant reservoir en route to a gas chromatograph. The flow was standardized to be within 10% of 50 sccm through use of a flow rate meter (Agilent ADM Flow Meter) at the gas chromatograph outlet.

6) Potentiostat setup:

Electrochemistry was performed using a Biologic VMP3-16 potentiostat in a two-electrode configuration. Cyclic voltammetry was performed Chronoamperometry was performed by holding a constant full-cell voltage (without *iR* compensation) was for 40 minutes after performing potentiostatic electrochemical impedance spectroscopy at the same voltage from 100 kHz to 100 mHz. Experiments were performed thrice for reproducibility.

7) Product quantification and collection:

An SRI 8610C Gas Chromatograph placed in-line with the membrane electrode assembly was used for collecting and quantifying gaseous products. For any given chronoamperometry experiment, three gas injections occurred at 5, 20, and 35 minutes into chronoamperometry. Liquid products were collected through both at the cathode via a bubbler and through the anolyte collected after chronoamperometry. Products were detected through ^{1}H nuclear magnetic resonance (Varian Inova 600) with a phenol/dimethylsulfoxide internal standard.

For calculating product selectivity, a molar flow rate $\dot{n}_i$ was first calculated using the equation $\dot{n}_i = c_i \times (Conversion\ Factor) \times \dot{V}$, where c_i is the measured product concentration from gas chromatography, $\dot{V}$ is measured flow rate, and using a conversion factor of $4.158 \times 10^{-11}\ \frac{mol}{ppm}$ as determined through gas chromatograph calibration. Faradaic efficiency to each product was then determined using the equation $FE_i = 100 \times \frac{\dot{n}_i F e_i}{\bar{J}}$, where F is Faraday's constant, e_i is the number of electrons transferred to that specific product, and $\bar{J}$ is current density averaged from the minute preceding injection. Total Faradaic efficiency is the sum of that equation to all detected products ($FE = \sum FE_i$).

8) SEM-EDS:

For the mesoporous Cu powder (uncoated and coated), a JEOL JSM-6700F scanning electron microscope (SEM) coupled with Energy-dispersive X-ray spectroscopy (EDS) was used to study their structure. EDS was performed to characterize the elemental composition of the samples. For the gas diffusion electrodes, SEM was performed using a Thermo Fisher Scientific Apreo S LoVac Scanning Electron Microscope equipped with a Bruker Quantax EBSD 400i integrated system for collecting EDS images and spectra. The accelerating voltage and current was 20 kV and 1.6 nA, respectively.

X-Ray Diffraction:

XRD was performed using a PANalytical X'Pert Pro powder diffractometer operating with Cu Kα radiation (λ = 1.5418 Å) using a 0.03° step size, a voltage of 45 kV, and a current of 40 mA. XRD patterns were recorded in the range of $15° < 2\theta < 85°$.

9) X-ray Photoelectron Spectroscopy (XPS):

XPS analysis was performed using a Kratos Axis Ultra DLD spectrometer with a monochromatic Al (Kα) radiation source. A charge neutralizer filament was used to control charging of the sample. A 20 eV pass energy was used with a 0.1 eV step size; scans were calibrated using adventitious carbon by setting the C 1s peak to 284.8 eV.

10) Nitrogen Porosimetry:

N_2 adsorption porosimetry was performed using a Micrometrics Tristar II 3020 on 100-120 mg powdered samples. Three different batches were used for each of the uncoated samples and two different batches for each of the coated samples to obtain averaged results. Before each measurement, the samples were degassed under vacuum for at least 12 hours at 90 ˚C to remove all water in the pores. Brauner- Emmett-Teller (BET) and Barrett-Joyner-Halenda (BJH) methods were used to obtain surface areas and pore size distributions, respectively.

4.3 Results and Discussion

Cu-Al alloys of three different compositions were made in a furnace under argon flow: 10at%Cu-90at%Al (hypoeutectic), 17.5at%Cu-82.5at%Al (eutectic) and 22at%Cu-78at%Al (hypereutectic). Each of these samples possessed a microstructure composed of Al-rich (α) phase and $CuAl_2$ intermetallic, as shown by XRD (Fig. S1). As the Cu content increased, the $CuAl_2$ content also increased and that of the α-phase decreased. These samples were dealloyed in 5wt% HCl under stirring and broken into powder due to insufficient mechanical integrity as a 3D monolith (Figure 1). The samples were then washed, dried under vacuum and stored in argon environment.

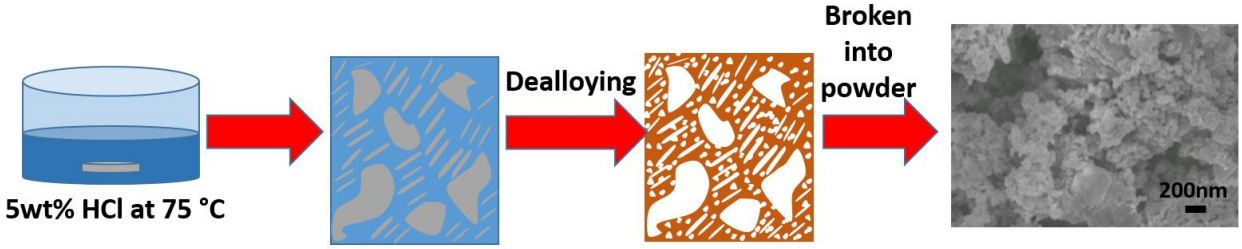

Figure 4.1. Cartoon of dealloying process for a hypoeutectic Cu-Al alloy immersed in 5wt% HCl at 75 ℃. Macroscopic image of a hypoeutectic alloy microstructure. After dealloying, there are a variety of macropores where there was primary and secondary α-phase (grey areas) and mesopores where there was $CuAl_2$. SEM image of sample broken into powder for further dealloying showing mesopores and some macropores.

In order to see the hierarchical porous structure of these samples, images of the 3D monoliths before and after dealloying are shown on Fig. 2. The hypoeutectic sample before dealloying (Fig. 2A) shows dark regions of hundreds of microns of primary α-phase and a lamellar region of

eutectic composed of alternating secondary α-phase and secondary $CuAl_2$ phase. After dealloying the primary α-phase gets dissolved leaving macropores of few hundreds of micron, the secondary Al-rich phase in the eutectic region leaves macropores of tens of micron (Fig. 2D) and the Al dissolved from the secondary $CuAl_2$ phase in the eutectic region leaves mesopores of tens of nm (Fig. 2G). Similarly, the eutectic sample before dealloying (Fig. 2B) shows a eutectic lamellar region with alternating dark regions representing α-phase areas and white regions representing $CuAl_2$ areas. After dealloying the Al dissolved from the α-phase areas leaves macropores of tens of micron and some elongated pores of hundreds of microns (Fig. 2E). Furthermore, the Al dissolved from the $CuAl_2$ leaves mesopores of tens of nm (Fig. 2H). Lastly, the hypereutectic sample before dealloying (Fig. 2C) shows light-colored grains of 100s of microns of primary $CuAl_2$ phase and a lamellar region of eutectic composed of alternating secondary α-phase and secondary $CuAl_2$ phase. After dealloying, the hypereutectic sample possesses pores of tens of micron from the Al dissolved in the secondary α-phase (Fig. 2F) and mesopores from both the primary and secondary $CuAl_2$ phases (Fig. 2I).

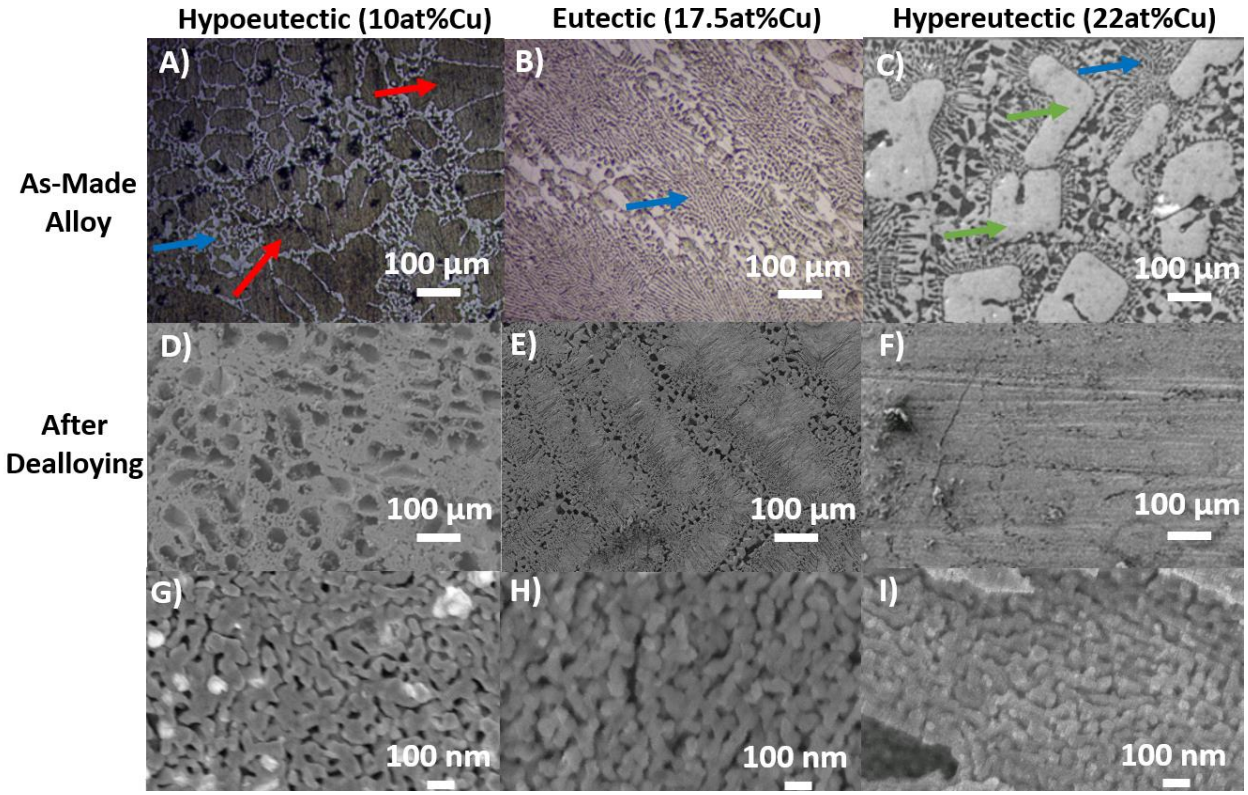

Figure 4.2. Optical microscope images of as-made (A) hypoeutectic, (B)eutectic and (C) hypereutectic alloys. SEM images of dealloyed Cu monoliths derived from (D) hypoeutectic, (E) eutectic and (F) hypereutectic samples showing their macropores. High-magnification SEM images of dealloyed Cu monoliths derived from (G) hypoeutecutic, (H) eutectic (I) hypereutectic samples showing their mesopores. Red arrows show primary Al (α-phase), blue arrows show eutectic phase composed of secondary α-phase and secondary $CuAl_2$ phase, and green arrows show primary $CuAl_2$ phase.

Samples were broken into powder (Fig. S3) before the end of the dealloying process to facilitate electrode fabrication. Only a Cu crystalline structure was observed according to XRD (Fig. S2). It should also be noted in the XRD that the eutectic sample shows the sharpest peaks and it is more (111) oriented, representative of its elongated grains and more uniform microstructure. Additionally, the hypereutectic sample shows the broadest peaks which is consistent with its predominantly mesoporous structure and higher density of small grain boundaries. EDS (Table S1) showed dilute amounts of Al (<5 at.%) left over (Fig. S4-S6). Furthermore, XPS (Table S2 and Figs. S7-S9) the presence of Cu and some trace amounts of CuO_x on all uncoated samples.

Nitrogen porosimetry (Fig. 4 and Table S4) of uncoated Cu samples show an increase in surface area with Cu content composition in precursor alloy (2.8 m^2/g for hypoeutectic, 6.8 m^2/g for eutectic, and 9.5 m^2/g for hypereutectic) due to the increasing amount of mesopores going from hypoeutectic to hypereutectic. This can be observed through sample differential pore size distribution (DPSD) showing an increasing peak intensity of mesopores and a peak shift to smaller average pore sizes (57.9 nm for hypoeutectic, 46.9 nm for eutectic, and 13.1 nm for hypereutectic) (Table S5)

Samples of these three powders were coated via galvanic displacement (Fig. S3) with either Ag or Au by immersing them in electrolytes containing the respective metal ions (details in experimental section), with hypereutectic samples in particular requiring either longer coating times or higher concentration of precursor solution. This is likely due to the higher number of smaller grain sizes, increased surface areas, and larger amounts of native oxide on the hypereutectic sample, which can hinder galvanic displacement.[34] EDS for the coated samples shows less than 4.3at% Al and less than 1at% of metal coating across all coated samples (Figs. S4-S6). XPS shows less than 2% of coating for all samples (Table S2-S3). Ag-coated samples (B and C, Fig. S7-S9) show Cu and CuO_x peaks, along with either Ag or Ag/AgO_x peaks[35] (AgO_x only for the Ag-coated hypoeutectic). Furthermore, all of the Au-coated samples (D and E in Figs. S7-S9) show Cu and CuO_x in addition to Au alloyed with Cu. This is observed in the Au $4f_{7/2}$ peak position shift by 0.1-0.3 eV from the metallic Au peak position of 84.0 eV, which indicates the presence of Au-Cu alloys.[36] These results were expected as Ag and Cu phase separate[37] and Au alloys[38] with Cu at room temperature.

Nitrogen porosimetry of the hypoeutectic sample (Fig. 4A) shows an increase in surface area (2.8 m^2/g) upon coating with either Ag (11.4 m^2/g) or Au (7.8 m^2/g). This is due to the easiness to coat sample with large pores of hundreds of microns in size that extend beyond the DSPD range (Fig. 4D) and little amount of mesopores. Coating these samples result in an increase in surface roughness that ultimately contribute to the increase in surface area. The eutectic sample experiences no significant change in surface area upon coating (Fig. 4B). The bimodal porous structure of eutectic in its DSPD (Fig. 4E) shows significant number of mesopores and pores well above 100nm. These bigger pores facilitate coating but the roughness created upon coating with Ag (7.1 m^2/g) or Au (7.2 m^2/g) does not change its original surface area (6.8 m^2/g) by much. The hypereutectic sample starts with a high density of mesopores (Fig 4F) and upon coating with Ag or Au, the smallest pores seem to be covered up by the coating material. The surface area does not change by much comparing the uncoated hypereutectic (9.5

m^2/g) to the one coated with Ag (7.7 m^2/g) or Au (9.6 m^2/g). Even though the coating on these samples is limited (~1at% coating from EDS), they manage to cover up the mesopores and spread the DSPD to bigger pore sizes (Fig. 4F).

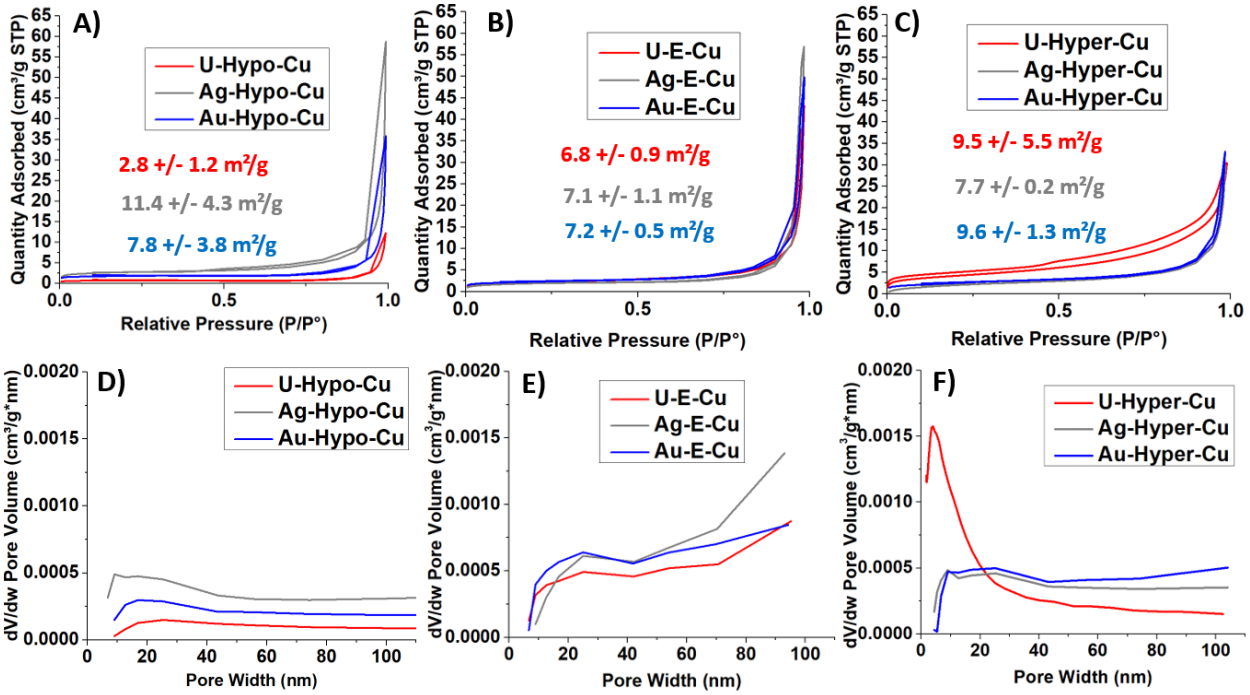

Figure 4.3. Nitrogen adsorption-desorption isotherms measured at 77 K on powdered samples and surface areas (A,B,C) of (A)uncoated (U-Hypo-Cu) and coated (Ag-Hypo-Cu and Au-Hypo-Cu) hypoeutectic samples; (B) uncoated (U-E-Cu), and coated (Ag-E-Cu and Au-E-Cu) eutectic samples and (C) uncoated (U-Hyper-Cu), and coated (Ag-Hyper-Cu and Au-Hyper-Cu) hypereutectic samples. The surface area value matches the color of the curve (red for uncoated samples, grey for Ag-coated samples and blue for Au-coated samples). Differential pore size distribution, dV/dW (D,E,F) for all nine powdered samples used in this work.

The nine powder samples shown in Fig. S3 were impregnated onto a gas diffusion layer for testing as a gas diffusion electrode (GDE) through forming an ink and manually spraying said ink onto the gas diffusion layer. While electrodes made through a manual process have a fair amount of variability, electrodes were found to have a target mass loading of approximately 1 mg/cm^2 (1.09 ± 0.4). This representative of variability associated with manual fabrication methods. [39,40] SEM-EDS measurements (Fig. S10-S18) performed on electrodes provide similar results as powder, along with minute amounts of silver and gold (< 3% relative to atomic percentage of Cu) observed in the case of secondary metal coating (Table S6-S14), with no particular trend with respect to precursor alloy composition. These electrodes were then put into an MEA electrolyzer to test their electrochemical performance.

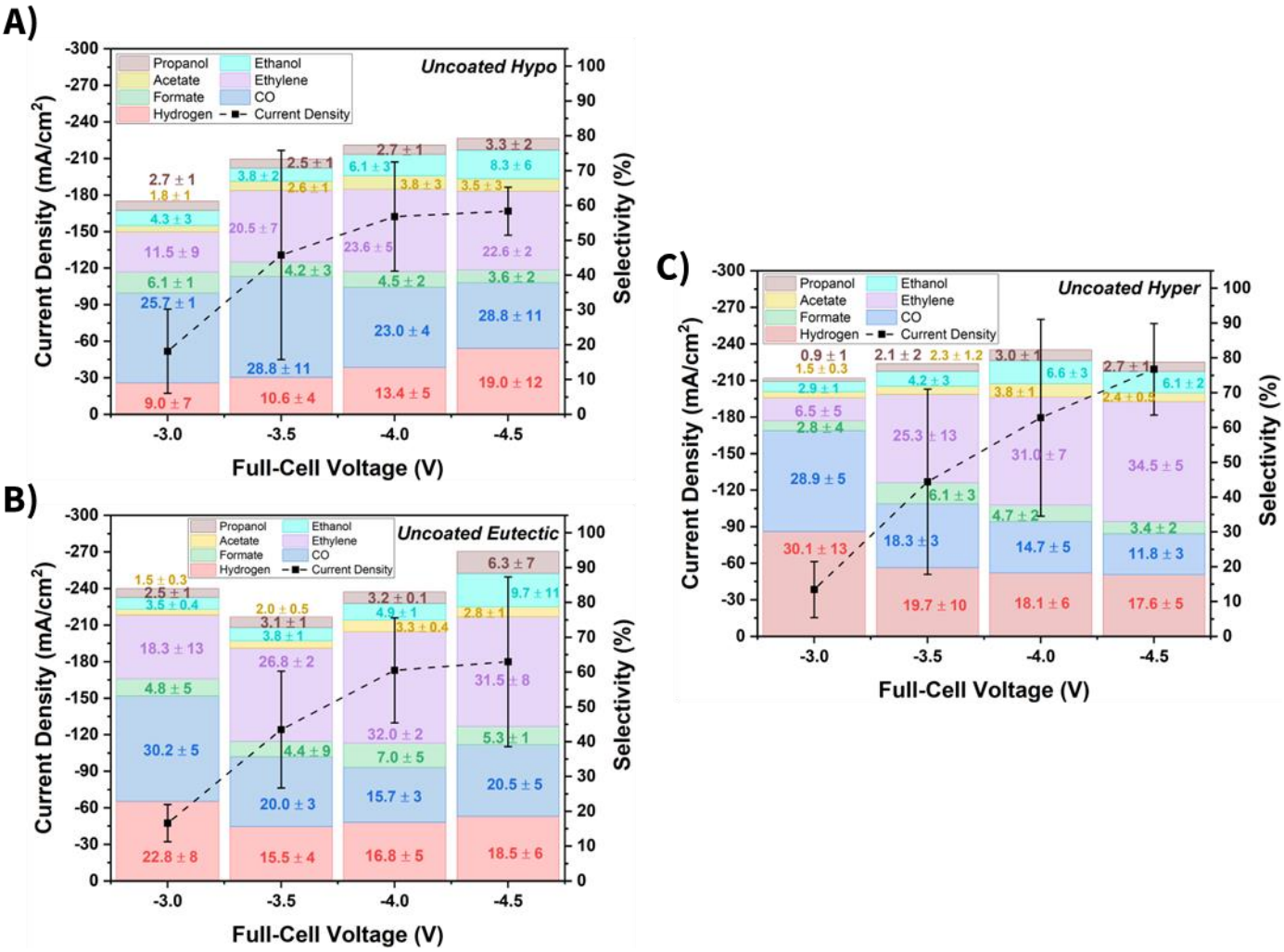

Figure 4.4. Measured selectivity and current density toward different CO_2R products on mesoporous dealloyed powder Cu, including (A) uncoated hypoeutectic, (B) uncoated Cu and (C) uncoated hypereutectic.

Uncoated samples were tested first to isolate the effect of increasing surface area. **Figure 4** shows the results of chronoamperometry on uncoated samples. Across samples, only around 70-80% of total Faradaic efficiency is able to be accounted for, with the rest expected to be lost from migration and subsequent oxidation of liquid products (formate, acetate, ethanol, propanol) at the anode.[41] Trace amounts (less than 1%) of methane, methanol, acetaldehyde, and ethylene glycol were also observed in varying amounts from each sample. (**Supplementary Dataset**) Generally, less C_1 and more C_{2+} products are observed as full-cell voltage becomes increasingly negative, but this trend grew more pronounced across compositional range, as moving from a hypoeutectic to hypereutectic sample resulted in a 52.2% increase in ethylene production at -4.5 V, (22.66% to 34.5%), accompanied with a 37% decrease at that same voltage (18.79% to

11.83%). Similar to the trend in reduced products, maximum geometric current densities also increased 31.5% over compositional range (166.72 mA/cm^2 for hypoeutectic, -179.88 mA/cm^2 for eutectic, and -219.27 mA/cm^2 for hypereutectic). This higher C_{2+} product production in the hypereutectic sample can be attributed not only to its superior surface area which allows for more catalytic sites, but most importantly to the smaller grain sizes and more lattice defects developed in mesoporous structures[42] during high temperature dealloying.[43]

Testing of coated samples occurred under the same conditions as uncoated samples to establish a general understanding of how composition and coating interact with surface area. The overall results for each sample can be found within the supplementary information (Fig. S19-S20), but in order to draw general insights from the effect of sample coating on electrochemical performance, results were compared across precursor alloy composition, full-cell voltage, and sample coating through a series of contour plots (**Figure 5**), highlighting a few key indicators, namely CO_2R:HER ratio (reflecting overall CO_2R selectivity) and C_{2+}:C_1 production ratios (indicating proportion of higher-reduced products). In short, compositional trends = remain consistent regardless of galvanic displacement coating: increasing the amount of copper in precursor alloy (eutectic, hypereutectic) translates to enhanced C_{2+} production over C_1 products as full-cell voltage becomes more negative. This trend is quite different from that of the competition between CO_2R and hydrogen evolution (HER); which is generally most favorable at the least negative full-cell voltages with the lowest amount of Cu in preceding alloy regardless of any coating. This HER increase with increased overpotential is consistent with other CO_2R studies conducted on planar Cu systems[7], as the additional overpotential also makes HER more favorable. While increased HER rates are also observed upon galvanic displacement coating, in the case of silver coating, the tradeoff is higher levels of C_{2+} production at a lower cell voltage (-127.41 mA/cm^2 at -4 V for the Ag-coated hypereutectic sample as compared to -103.26 mA/cm^2 at -4.5 V for the uncoated hypereutectic sample, a 23.3% increase) and an improvement in C_{2+} selectivity over C_1 selectivity (4.27 at -4.5 V for the Ag-coated hypereutectic sample over 2.98 at the same voltage for the uncoated sample, a 43.2% increase in C_{2+}:C_1 ratio).

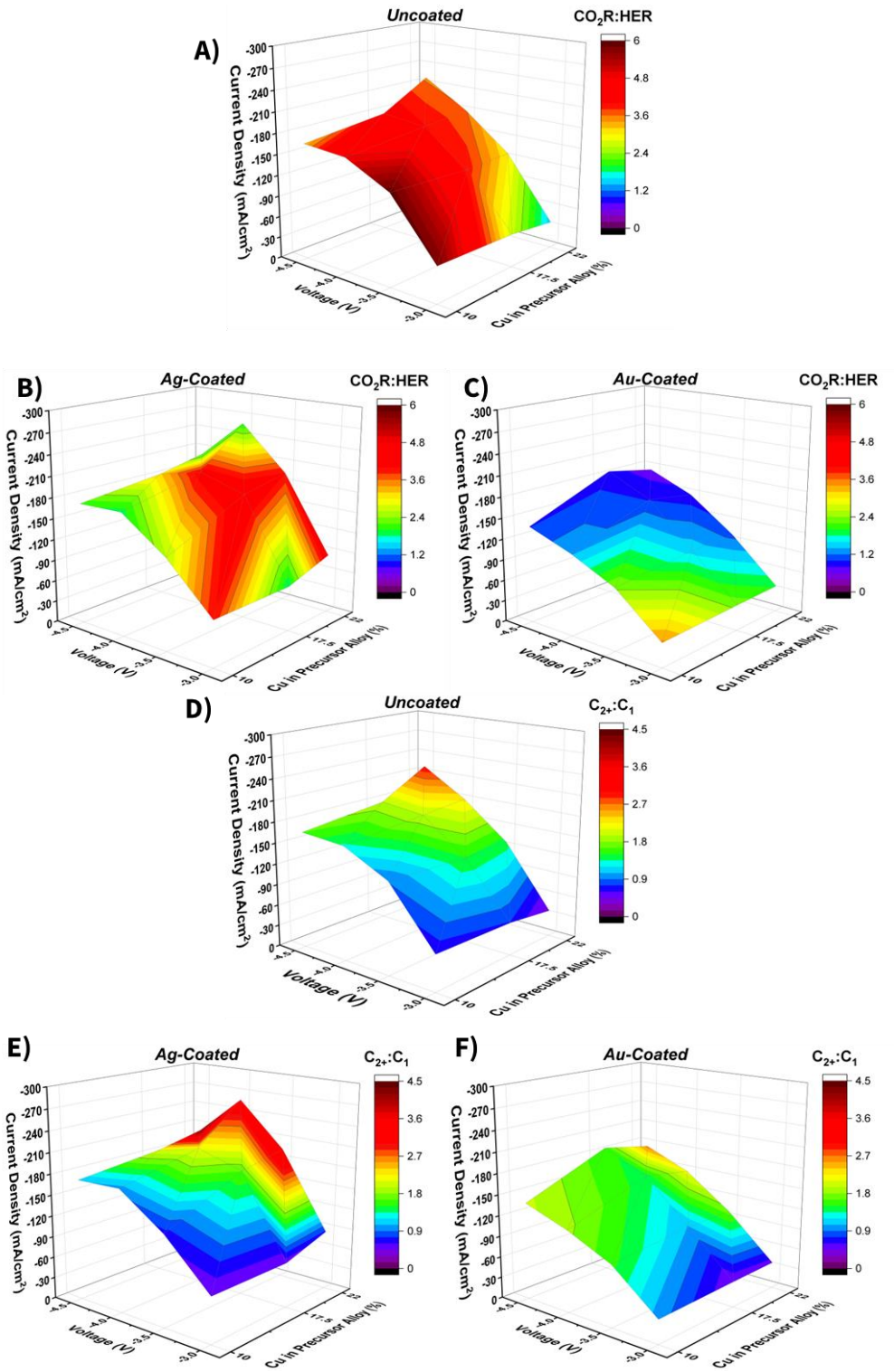

Figure 4.5. Top: Contour plots comparing ratios of CO_2R:HER reaction rates across full-cell voltage and amount of Cu in precursor alloy for (A) uncoated, (B) Ag-coated, and (C) Au-coated samples. Bottom: Contour plots comparing ratios of C_2:C_1 production rates across full-cell voltage and amount of Cu in precursor alloy for the (D) uncoated, (E) Ag-coated, and (F) Au-coated Cu samples.

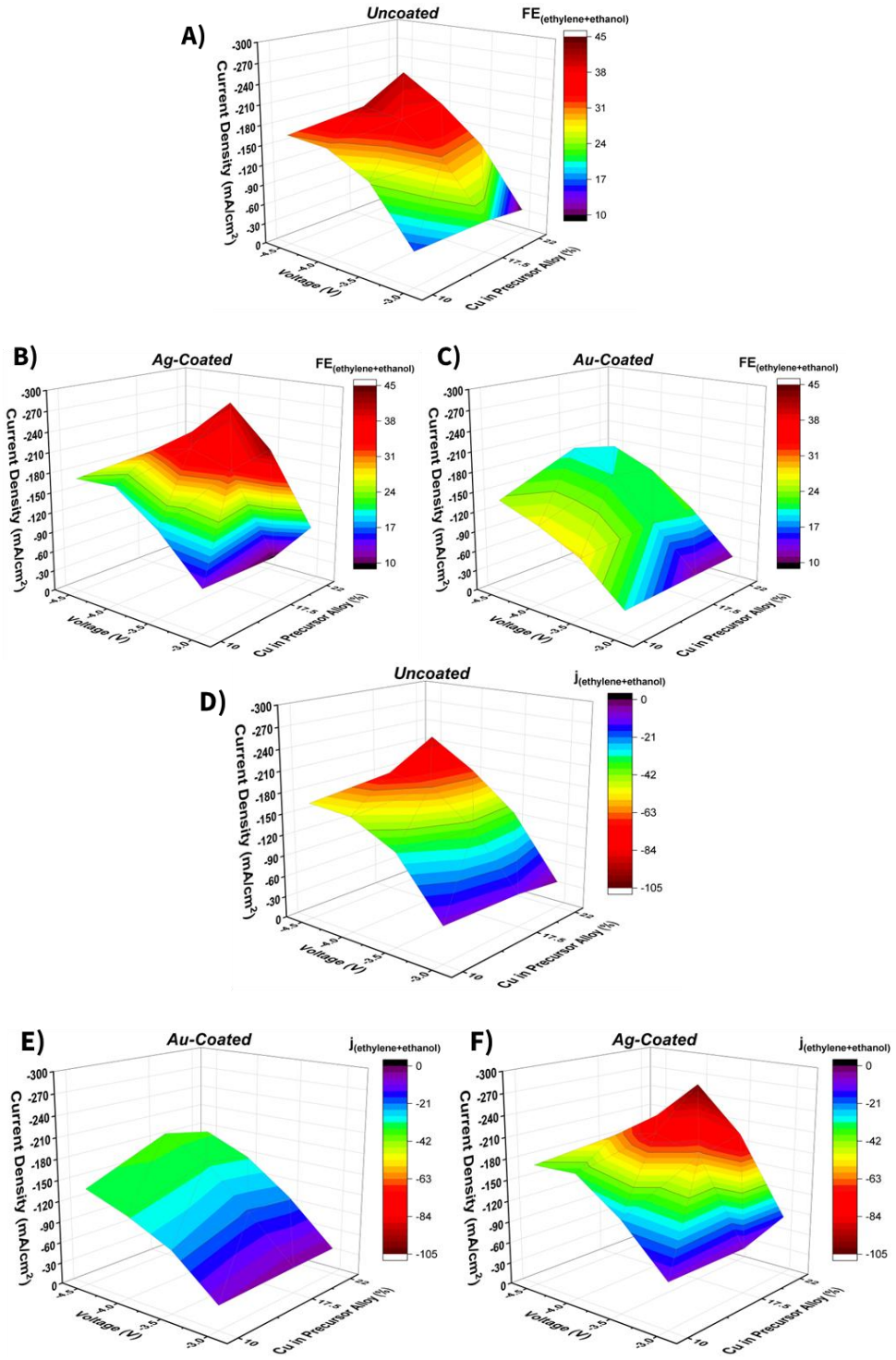

Figure 4.6. Top: Contour plots comparing the faradaic efficiency (FE) across full-cell voltage and amount of Cu in precursor alloy for (A) uncoated, (B) Ag-coated, and (C) Au-coated samples. Bottom: Contour plots comparing partial current density (j) of ethylene and ethanol production across full-cell voltage and amount of Cu in precursor alloy for (D) uncoated, (E) Ag-coated, and (F) Au-coated Cu samples.

Figure 6 highlights the combined production of two industrially-relevant, higher-reduced products in ethylene and ethanol. On a selectivity basis, both uncoated and silver-coated samples show similar combined Faradaic efficiencies at peak production conditions (ranging between 35-40%); a more significant difference is observed in comparing peak current densities, with a maximum combined partial current density of -102.44 mA/cm^2 for the Ag-coated hypereutectic, a 14.8% increase over its uncoated counterpart (-89.16 mA/cm^2). While the silver coating provides a slight increase in peak production of ethylene and ethanol (and a clear enhancement of C_{2+}:C_1 ratio), this same effect is not observed with a gold coating, which results in lower overall current densities (< 200 mA/cm^2), CO_2R selectivities (<30% combined selectivity to ethylene and ethanol), and dramatically lower C_{2+} production rates relative to (consistently below 50 mA/cm^2). A proposed explanation for the failure of Au to provide a tandem effect lies in potential windows: selectivity changes as a function of cell potential, and if the potential regimes for gold and copper do not align, that would be sufficient to explain the absence of a tandem effect. Fundamental studies of CO_2R on gold[44] and silver[45] show silver has an expanded potential window for carbon monoxide production out to -1.3 V vs. RHE, whereas gold surfaces see a significant increase in HER by -0.9 V vs. RHE, supporting the idea that the effect of a gold coating is to promote HER over providing a tandem effect. Further, since a tandem effect of gold on copper has been observed[22] at lower overpotentials (-0.75 V vs. RHE) and at low current densities, an entirely different effect may be seen as a result of system architecture and operating voltage. Although the specific operating half-cell potential is unknown, knowing the difference between the potential windows of Cu and Au combined with knowing that larger overpotentials are needed to begin seeing C_2 products gives strong reason to expect increased HER with Au in this work.

A deeper comparison between silver-coated and uncoated samples begins to illuminate how two different phenomena (original sample structure, sample coating) interact with each other when combined. Not only is the structure created upon dealloying (smaller grain sizes, smaller average pore size, larger initial surface area) beneficial for CO_2R, this structure also appears to be the most optimal for galvanic displacement coating, as the strongest enhancement due to tandem catalysis is seen in the hypereutectic composition. In other words, composition-dependent structure becomes a prerequisite to leveraging secondary effects. Although trends in sample surface area with respect to composition change upon coating, the fact that the trend in electrochemical performance with respect to composition stays constant indicates that the advantages in composition-dependent structure extend beyond just surface area to pore and grain size, and these advantages are robust to additional processes (powder formation, galvanic displacement coating, electrode fabrication). In short, this work indicates how tunable catalyst powder composition can serve as a scalable platform for integrating multiple strategies for tuning CO_2R selectivity and enhancing the development of catalyst layers for CO_2 electrolysis.

4.4 Conclusion

To summarize, mesoporous copper powders were made by dissolving Al from Cu-Al alloys via chemical dealloying in hydrochloric acid at high temperature. These mesoporous powders were coated with dilute amounts of silver or gold to realize tandem catalysis to further enhance

production of highly reduced CO_2R products. Tuning alloy composition through precursor amount of copper clearly shows the ability to improve C_{2+} production rates (particularly those of ethylene and ethanol) through improved surface area, decreased average pore size, and higher density of small grain boundaries and lattice defects. The presence of a silver coating provides a slight boost to C_{2+} production through a tandem catalytic effect while a gold coating hampers CO_2R performance relative to having no coating due to increased hydrogen production. Improving structural properties through composition-dependent tuning is crucial to leveraging this effect, evidenced from maximum C_{2+} selectivity, ethylene, and ethanol production with an Ag-coated hypereutectic GDE. Further work can be done to investigate the compositional relationship for alloys with larger amounts of copper precursor (this work only goes up to 22%, the presence of an Al-$CuAl_2$ eutectic is present up to 33%) and to rigorously quantify the effect of electrochemically active surface area (ECSA). The strategies developed in this work can be used to engineer high surface area catalysts for CO_2 reduction, produce them in large scale and optimize their performance.

4.5 References

(1) Nitopi, S.; Bertheussen, E.; Scott, S. B.; Liu, X.; Engstfeld, A. K.; Horch, S.; Seger, B.; Stephens, I. E. L.; Chan, K.; Hahn, C.; Nørskov, J. K.; Jaramillo, T. H.; Chorkendorf, I. Progress and Perspectives of Electrochemical CO2 Reduction on Copper in Aqueous Electrolyte. Chem. Rev. 2019, 119, 7610−7672

(2) Chu, S.; Majumdar, A. Opportunities and challenges for a sustainable energy future. Nature, 2012, 488.

(3) Grim, R. G.; Huang, Z.; Guarnieri, M. T.; Ferrell III, J. R.; Tao, L.; Schaidle, J. A. Transforming the carbon economy: challenges and opportunities in the convergence of low-cost electricity and reductive CO_2 utilization. Energy Environ. Sci., 2020, 13, 472-494.

(4) Higgins, D.; Hahn, C.; Xiang, C.; Jaramillo, T. F.; Weber, A. Z. Gas-Diffusion Electrodes for Carbon Dioxide Reduction: A New Paradigm. *ACS Energy Lett.* **2019**, *4* (1), 317–324.

(5) Gabardo, C. M.; O'Brien, C. P.; Edwards, J. P.; McCallum, C.; Xu, Y.; Dinh, C. T.; Li, J.; Sargent, E. H.; Sinton, D. Continuous Carbon Dioxide Electroreduction to Concentrated Multi-Carbon Products Using a Membrane Electrode Assembly. *Joule* **2019**, *3* (11), 2777–2791.

(6) Hori, Y.; Wakebe, H.; Tsukamoto, T.; Koga, O. Electrocatalytic Process of CO Selectivity in Electrochemical Reduction of CO2 at Metal Electrodes in Aqueous Media. *Electrochim. Acta* **1994**, *39* (11–12), 1833–1839.

(7) Kuhl, K. P.; Cave, E. R.; Abram, D. N.; Jaramillo, T. F. New Insights into the Electrochemical Reduction of Carbon Dioxide on Metallic Copper Surfaces. *Energy Environ. Sci.* **2012**, *5* (5), 7050.

(8) Nitopi, S.; Bertheussen, E.; Scott, S. B.; Liu, X.; Engstfeld, A. K.; Horch, S.; Seger, B.; Stephens, I. E. L.; Chan, K.; Hahn, C.; Nørskov, J. K.; Jaramillo, T. F.; Chorkendorff, I. Progress and Perspectives of Electrochemical CO 2 Reduction on Copper in Aqueous Electrolyte.

(9) Liu, S.; Pang, F.; Zhang, Q.; Guo, R.; Wang, Z.; Wang, Y.; Zhang, W.; Ou, J. Stable Nanoporous Sn/SnO 2 Composites for Efficient Electroreduction of CO 2 to Formate over Wide Potential Range. *Appl. Mater. Today* **2018**, *13*, 135–143.

(10) Hyun, G.; Song, J. T.; Ahn, C.; Ham, Y.; Cho, D.; Oh, J.; Jeon, S. Hierarchically Porous Au Nanostructures with Interconnected Channels for Efficient Mass Transport in Electrocatalytic CO2 Reduction. *Proc. Natl. Acad. Sci. U. S. A.* **2020**, *117* (11), 5680–5685.

(11) Abeyweera, S. et al. Hierarchically 3D Porous Ag Nanostructures Derived from Silver Benzenethiolate Nanoboxes: Enabling CO_2 Reduction with a Near-Unity Selectivity and Mass-Specific Current Density over 500 A/g. Nano Lett. 2020, 20, 2806−2811

(12) Cho, S. A.; Jin Jang, Y.; Lim, H.-D.; Lee, J.-E.; Hee Jang, Y.; Hong Nguyen, T.-T.; Marques Mota, F.; Fenning, D. P.; Kang, K.; Shao-Horn, Y.; Ha Kim, D.; Cho, S. A.; Jang, Y. J.; Lee, J.; Jang, Y. H.; Nguyen, T. H.; Mota, F. M.; Kim, D. H.; Lim, H.; Kang, K. S.; Fenning, D. P.; Shao-Horn, Y. Hierarchical Porous Carbonized Co 3 O 4 Inverse Opals via Combined Block Copolymer and Colloid Templating as Bifunctional Electrocatalysts in Li-O 2 Battery Lithium-Oxygen Batteries. **2017**.

(13) Wang, H.; Han, Z.; Zhang, L.; Cui, C.; Zhu, X.; Liu, X.; Han, J.; Ge, Q. Enhanced CO selectivity and stability for electrocatalytic reduction of CO2 on electrodeposited nanostructured porous Ag electrode. Journal of CO2 Utilization 15 (2016) 41–49

(14) Chen, Z.; Wang, T.; Liu, B.; Cheng, D.; Hu, C.; Zhang, G.; Zhu, W.; Wang, H.; Zhao, Z.; Gong, J. Grain-Boundary-Rich Copper for Efficient Solar-Driven Electrochemical CO2 Reduction to Ethylene and Ethanol. J. Am. Chem. Soc. 2020, 142, 6878−6883

(15) Mariano, R. G.; McKelvey, K.; White, H. S.; Kanan, M. W. Selective increase in CO_2 electroreduction activity at grain-boundary surface terminations. Science, 358, 1187–1192

(2017)
(16) Gu, Z.; Shen, H.; Chen, Z.; Yang, Y.; Yang, C.; Ji, Y.; Wang, Y.; Zhu, C.; Liu, J.; Li, J; Sham, T.; Xu, X.; Zheng, G. Efficient Electrocatalytic CO2 Reduction to C2+ Alcohols at Defect-Site-Rich Cu Surface. Joule, 2021, 5, 429–440.
(17) Sharma, P. P.; Wu, J.; Yadav, R. M.; Liu, M.; Wright, C. J.; Tiwary, C. S.; Yakobson, B.; Lou J.; Ajaya, P. M.; Zhou, X. Nitrogen-Doped Carbon Nanotube Arrays for High Efficiency Electrochemical Reduction of CO2: On the Understanding of Defects, Defect Density, and Selectivity. Angew. Chem, 2015, 127, 13905–13909.
(18) Hannagan, R. T.; Giannakakis, G.; Flytzani-Stephanopoulos, M.; Skyes, E. C. H. Single-Atom Alloy Catalysis. Chem. Rev. 2020, 120, 12044−12088.
(19) Liu, K.; Ma, M.; Wu, L.; Valenti, M.; Cardenas-Morcoso, D.; Hofmann, J. P.; Bisquert, J.; Gimenez, S.; Smith, W. A. Electronic Effects Determine the Selectivity of Planar Au-Cu Bimetallic Thin Films for Electrochemical CO 2 Reduction. *ACS Appl. Mater. Interfaces* **2019**, *11* (18), 16546–16555.
(20) Higgins, D.; Landers, A. T.; Ji, Y.; Nitopi, S.; Morales-Guio, C. G.; Wang, L.; Chan, K.; Hahn, C.; Jaramillo, T. F. Guiding Electrochemical Carbon Dioxide Reduction toward Carbonyls Using Copper Silver Thin Films with Interphase Miscibility. *ACS Energy Lett* **2018**, *3*, 25.
(21) Zhang, H.; Chang, X.; Chen, J. G.; Goddard, W. A.; Xu, B.; Cheng, M. J.; Lu, Q. Computational and Experimental Demonstrations of One-Pot Tandem Catalysis for Electrochemical Carbon Dioxide Reduction to Methane. *Nat. Commun.* **2019**, *10* (1), 1–9.
(22) Morales-Guio, C. G.; Cave, E. R.; Nitopi, S. A.; Feaster, J. T.; Wang, L.; Kuhl, K. P.; Jackson, A.; Johnson, N. C.; Abram, D. N.; Hatsukade, T.; Hahn, C.; Jaramillo, T. F. Improved CO2 Reduction Activity towards C2+ Alcohols on a Tandem Gold on Copper Electrocatalyst. *Nat. Catal.* **2018**, *1* (10), 764–771.
(23) Chen, C.; Li, Y.; Yu, S.; Li, M.; Ross, M. B.; Yang, P. Cu-Ag Tandem Catalysts for High-Rate CO 2 Electrolysis toward Multicarbons. *Joule* **2020**, *4*, 1688–1699.
(24) Weitzner, S. E.; Akhade, S. A.; Kashi, A. R.; Qi, Z.; Buckley, A. K.; Huo, Z.; Ma, S.; Biener, M.; Wood, B. C.; Kuhl, K. P.; Varley, J. B.; Biener, J. Evaluating the Stability and Activity of Dilute Cu-Based Alloys for Electrochemical CO2 Reduction. *J. Chem. Phys.* **2021**, *155* (11), 114702.
(25) Y. An, Y. Tian, C. Wei, Y. Tao, B. Xi, S. Xiong, J. Feng, Y. Qian. Dealloying: An effective method for scalable fabrication of 0D, 1D, 2D, 3D materials and its application in energy storage. Nano Today, 37 (2021) 101094.
(26) T. Songa, M. Yanb, M. Qiana. The enabling role of dealloying in the creation of specific hierarchical porous metal structures—A review. Corrosion Science 134 (2018) 78–98
(27) Y. Funamizu, K. Watanabe. Interdiffusion in the Al-Cu System*. Trans. Jpn. Inst. Met., 12(1971), pp. 147-152.
(28) Chen F.; Chen, X.; Zou, L.; Yao, Y.; Lin, Y.; Shen, Q.; Lavernia, E. J.; Zhang, L. Fabrication and mechanical behavior of bulk nanoporous Cu via chemical de-alloying of Cu–Al alloys. Materials Science & Engineering A 660 (2016) 241–250.
(29) Zhong, M.; Tran, K.; Min, Y.; Wang, C.; Wang, Z.; Dinh, C.-T.; De Luna, P.; Yu, Z.; Sedighian Rasouli, A.; Brodersen, P.; Sun, S.; Voznyy, O.; Tan, C.-S.; Askerka, M.; Che, F.; Liu, M.; Seifitokaldani, A.; Pang, Y.; Lo, S.-C.; Ip, A.; Ulissi, Z.; Sargent, E. H. Accelerated Discovery of CO 2 Electrocatalysts Using Active Machine Learning. | *Nat.* | **2020**, *581*.
(30) Qi, Z.; Biener, M. M.; Kashi, A. R.; Hunegnaw, S.; Leung, A.; Ma, S.; Huo, Z.; Kuhl, K. P.; Biener, J. Scalable Fabrication of High Activity Nanoporous Copper Powders for Electrochemical CO2 Reduction via Ball Milling and Dealloying. *J. CO2 Util.* **2021**, *45*, 101454.

(31) Simon, F. Deposition of Gold without External Current Source. Gold 8ull., 1993, 26 (1)
(32) Lapeire, L.; Martinez Lombardia, E.; Verbeken, K.; De Graeve, I.; Terryn, H.; Kestens, L. A. I. Structural dependence of gold deposition by nanoplating in polycrystalline copper. *J Mater Sci* (2014) 49:3909–3916
(33) Cui, S.; Zhai, P.; Yang, W.; Wei, Y.; Xiao, J.; Deng, L.; Gong, Y. Large-Scale Modification of Commercial Copper Foil with Lithiophilic Metal Layer for Li Metal Battery. Small 2020, 1905620
(34) Ai, J.H.; Liu, S. P.; Widharta, N.A.; Adhikari, S.; Anderegg, J. W.; Hebert, K. R. Copper Layers Deposited on Aluminum by Galvanic Displacement. J. Phys. Chem. C, 2011, 115, 22354–22359
(35) Jeon, Y.; Choi, I.; Kim, J. Facile electrochemical fabrication of Ag/Cu bi-metallic catalysts and the dependence of their selectivity for electrochemical CO_2 reduction on the surface composition. *Thin Solid Films* 726 (2021) 138674
(36) Kim, J.; Woo, H.; Yun, S.; Jung, H.; Back, S.; Jung, Y.; Kim, Y. Highly active and selective Au thin layer on Cu polycrystalline surface prepared by galvanic displacement for the electrochemical reduction of CO2 to CO. *Appl. Catal.* 213 (2017) 211–215
(37) Chu, M. Z.; Qin, Y. Z.; Xiao, T.; Shen, W.; Su, T.; Hu, C.H.; Tang, C. Thermodynamic reassessment of the Ag–Cu phase diagram at nano-scale. Calphad 72 (2021) 102233
(38) Ravi, R. Paul, A. Diffusion mechanism in the gold-copper system. J Mater Sci: Mater Electron (2012) 23:2152–215
(39) Jhong, H-R. M.; Brushett, F. R.; Kenis, P. J. A. The Effects of Catalyst Layer Deposition Methodology on Electrode Performance. *Advanced Energy Materials* **2013**, *3* (5), 589-599.
(40) Lees, E. W.; Mowbray, B. A. W.; Salvatore, D. A.; Simpson, G. L.; Dvorak, D.; Ren, S.; Chau, J.; Milton, K. L.; Berlinguette, C. P. Linking gas diffusion electrode composition to CO_2 reduction in a flow cell. *J. Mater. Chem. A* **2020**, *8*, 19493-19501.
(41) Gastón, G.; Larrazábal, O. L.; Strøm-Hansen, P.; Heli, J. P.; Zeiter, K.; Therkildsen, K. T.; Chorkendorff, I.; Seger, B. Analysis of Mass Flows and Membrane Cross-over in CO_2 Reduction at High Current Densities in an MEA-Type Electrolyzer. 2019.
(42) Shankar, A.; Chatterjee, A. Nanoporosity evolution during dealloying: Interplay between chemical dissolution, material defects, coarsening and local structural rearrangements over long timescales. Acta Materialia 213 (2021) 116974
(43) Liu, W. B.; Zhang, S. C.; Li, N.; Zheng, J. W.; Xing, Y. L. A facile one-pot route to fabricate nanoporous copper with controlled hierarchical pore size distributions through chemical dealloying of Al–Cu alloy in an alkaline solution. Microporous and Mesoporous Materials 138 (2011) 1–7
(44) Cave, E. R.; Montoya, J. H.; Kuhl, K.; Abram, D. N.; Hatsukade, T.; Shi, C.; Hanh, C.; Nørskov, J. K.; Jaramillo, T. F. Electrochemical CO_2 reduction on Au surfaces: mechanistic aspects regarding the formation of major and minor products. Phys. Chem. Chem. Phys., 2017, 19, 15856—15863.
(45) Hatsukade, T.; Kuhl, K. P.; Cave, E. R.; Abram, D. N.; Jaramillo, T. F. Insights into the electrocatalytic reduction of CO_2 on metallic silver surfaces. Phys. Chem. Chem. Phys., 2014, 16, 13814—13819

APPENDIX A

Supplementary Information for Chapter 2: Quantitatively Designing Porous Copper Current Collectors for Lithium Metal Anodes

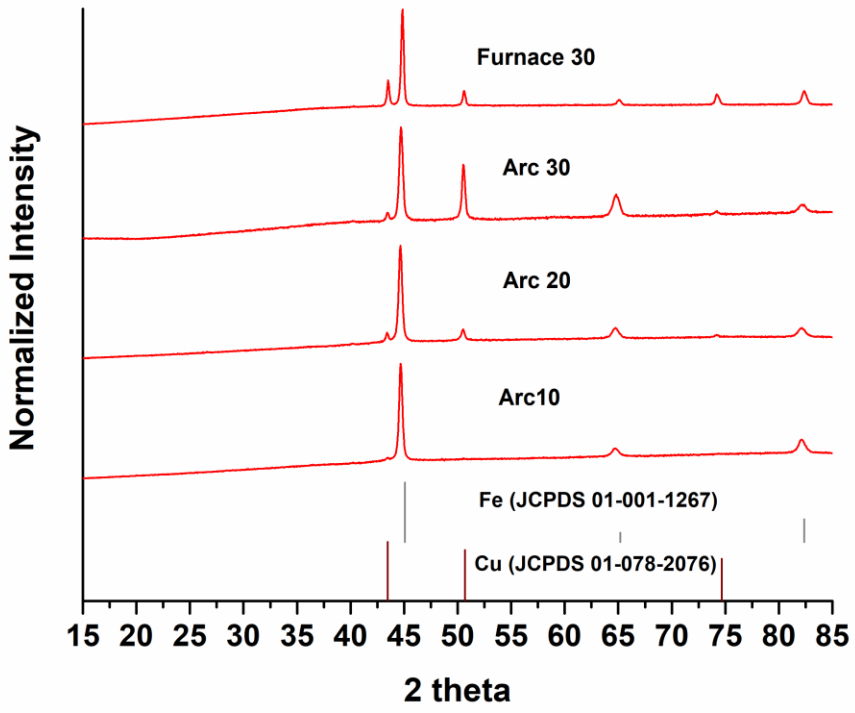

Figure S1. X-ray diffraction of the four Cu-Fe composites used in this work: 10Arc, 20Arc, 30Arc and 30Furnace. Also included are reference patters for Cu and Fe metal. All samples are composed of a combination of pure Fe and pure Cu.

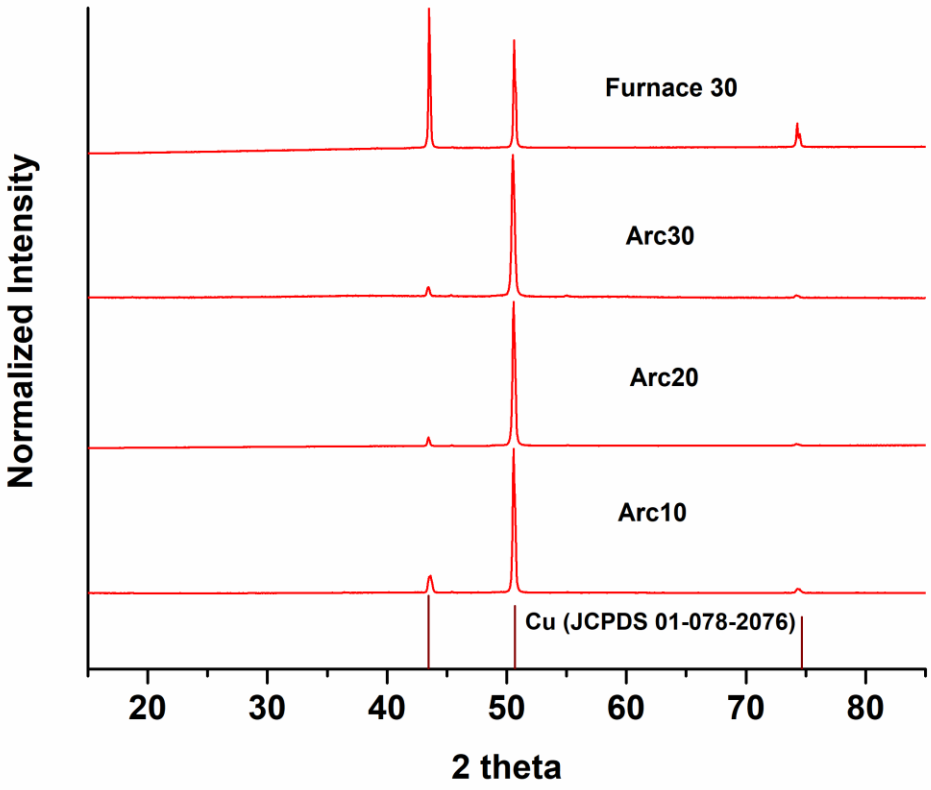

Figure S2. X-ray diffraction patterns of the four porous Cu samples used in this work after acid etching and cleaning. A Cu reference pattern is also included. The sample prepared using furnace derived Cu-Fe composites showed minimal preferential grain orientation, while the arc melted samples showed significant preferred orientation.

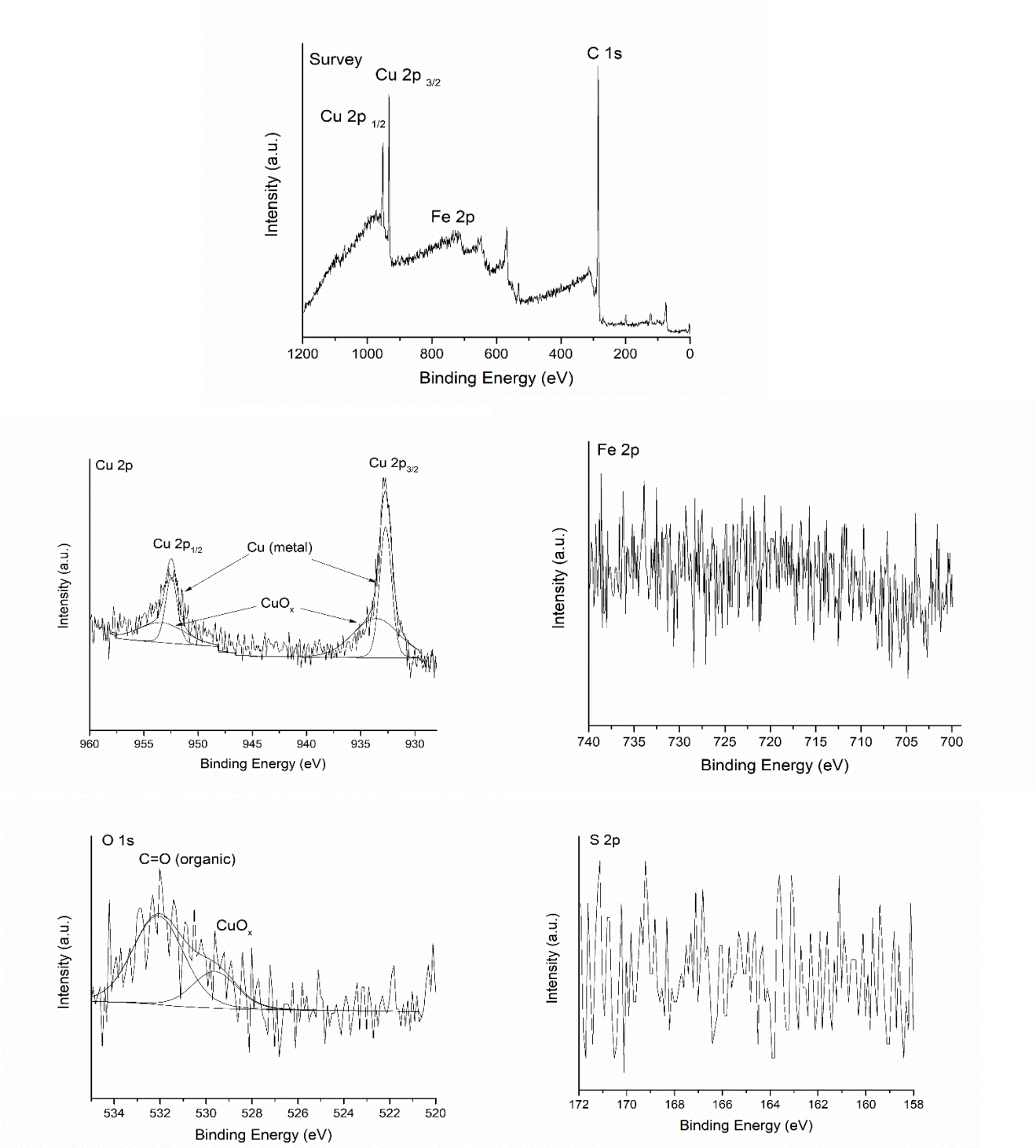

Figure S3. XPS of the 30Furnace sample after acid etching and cleaning. The sample was etched using argon ion sputtering at 4kV for 1min. The sample is composed of Cu with a small amount of surface CuO_x, as evidenced by the Cu 2p and O 1s spectra. The additional low intensity peak in the O 1s spectrum at 532 eV is associated with low levels of surface adsorbed species such as CO_2. No Fe or S were detected.

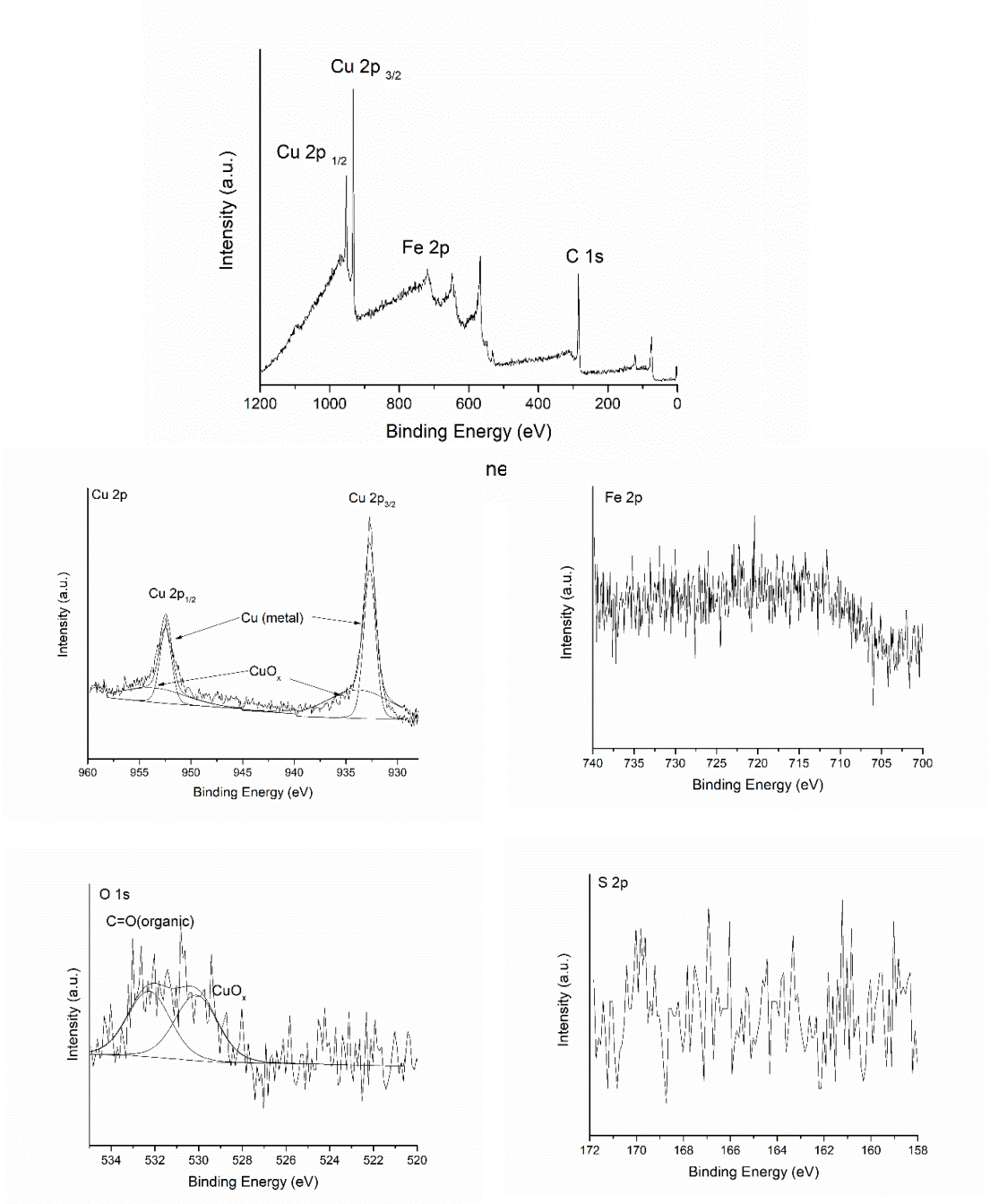

Figure S4. XPS of the 30Arc sample after acid etching and cleaning. The sample was etched using argon ion sputtering at 4kV for 1min. The sample is composed of Cu with a small amount of surface CuO_x, as evidenced by the Cu 2p and O 1s spectra. The additional low intensity peak in the O 1s spectrum at 532 eV is associated with low levels of surface adsorbed species such as CO_2. No Fe or S were detected.

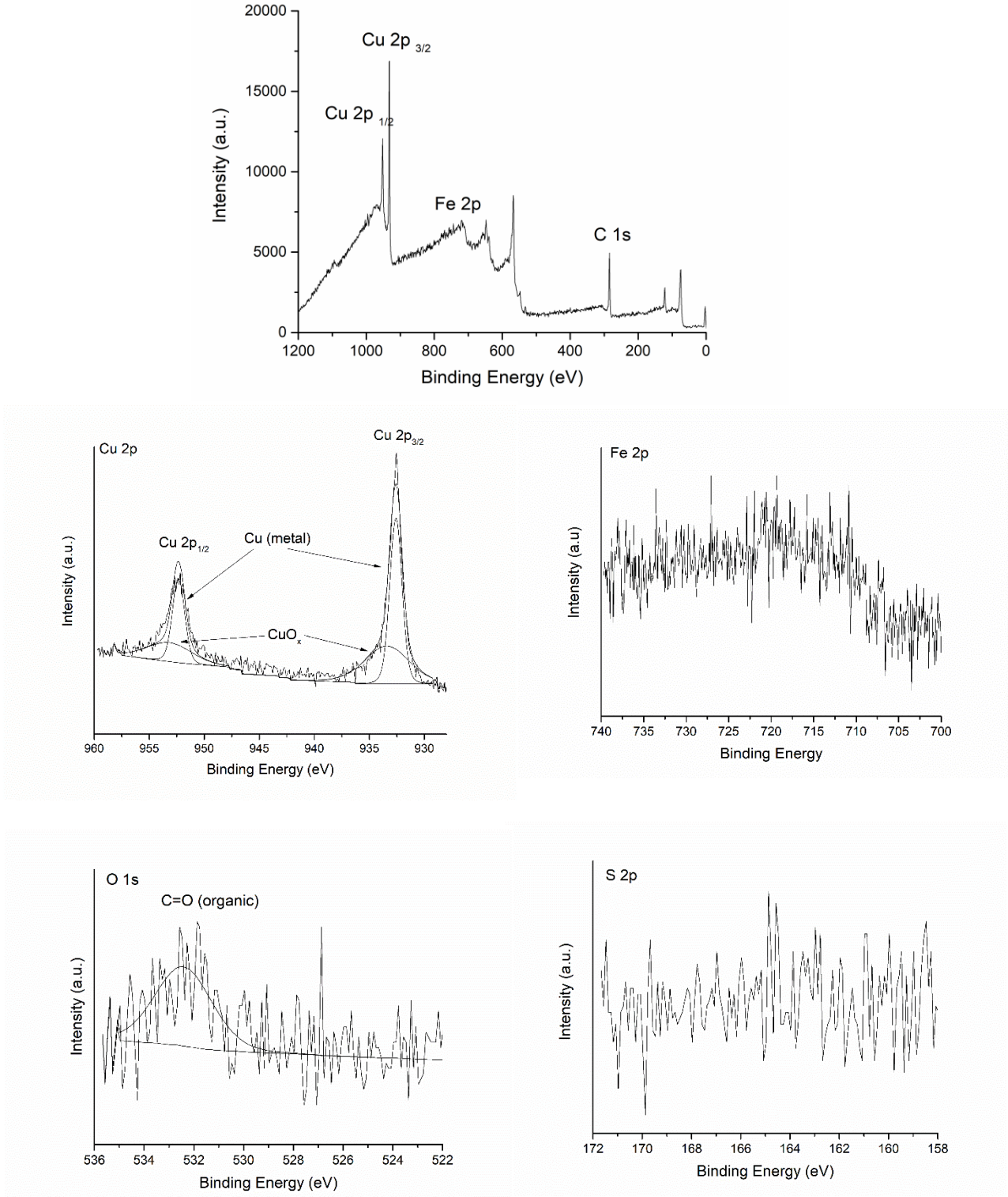

Figure S5. XPS of the 20Arc sample after acid etching and cleaning. The sample was etched using argon ion sputtering at 4 kV for 1 min. The sample is composed of Cu with a small amount of surface CuO_x, as evidenced by the Cu 2p and O 1s spectra. No Fe or S were detected.

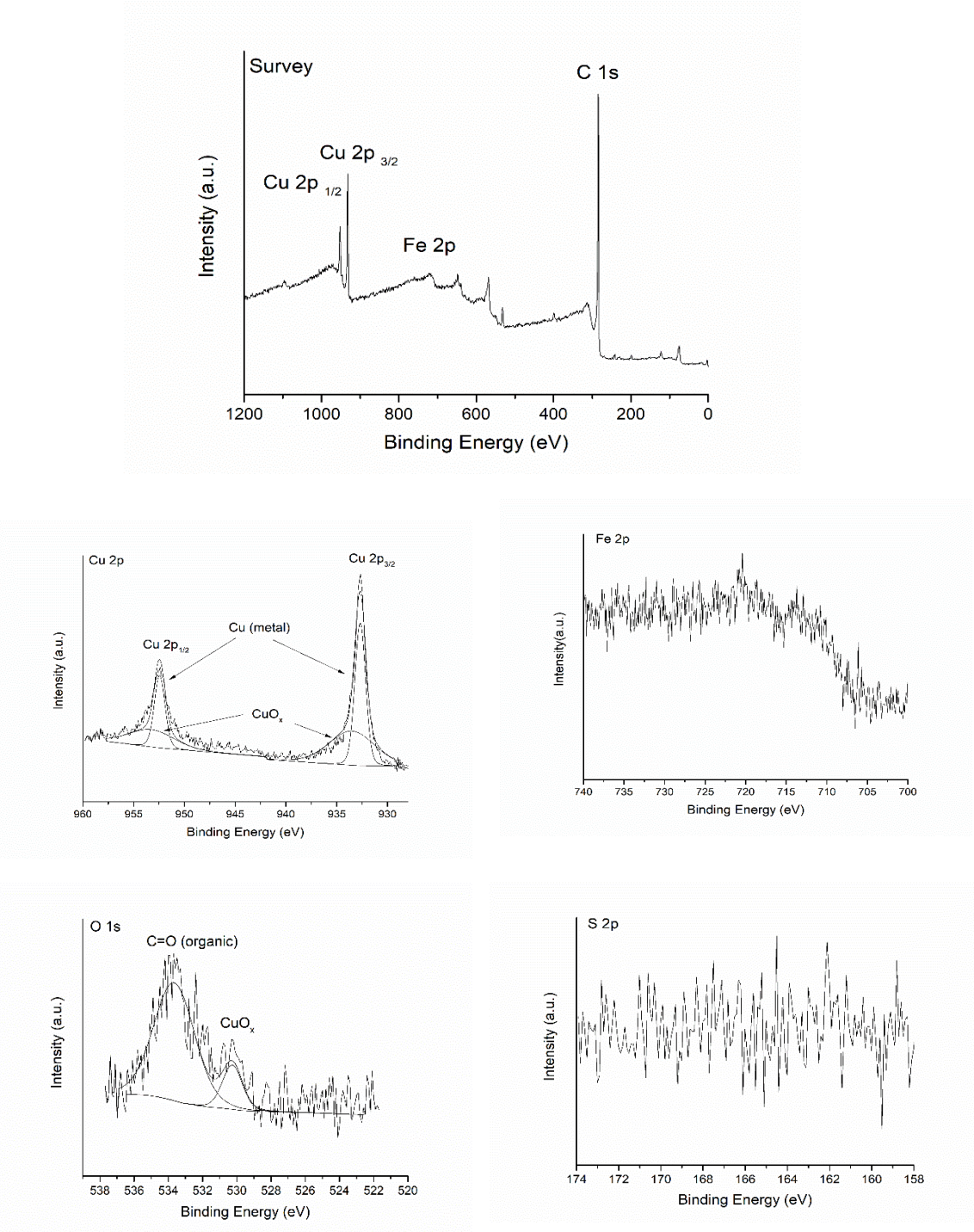

Figure S6. XPS of the 10Arc sample after acid etching and cleaning. The sample was etched using argon ion sputtering at 4 kV for 1 min. The sample is composed of Cu with a small amount of surface CuO_x, as evidenced by the Cu 2p and O 1s spectra. The additional low intensity peak in the O 1s spectrum at 532 eV is associated with low levels of surface adsorbed species such as CO_2. No Fe or S were detected.

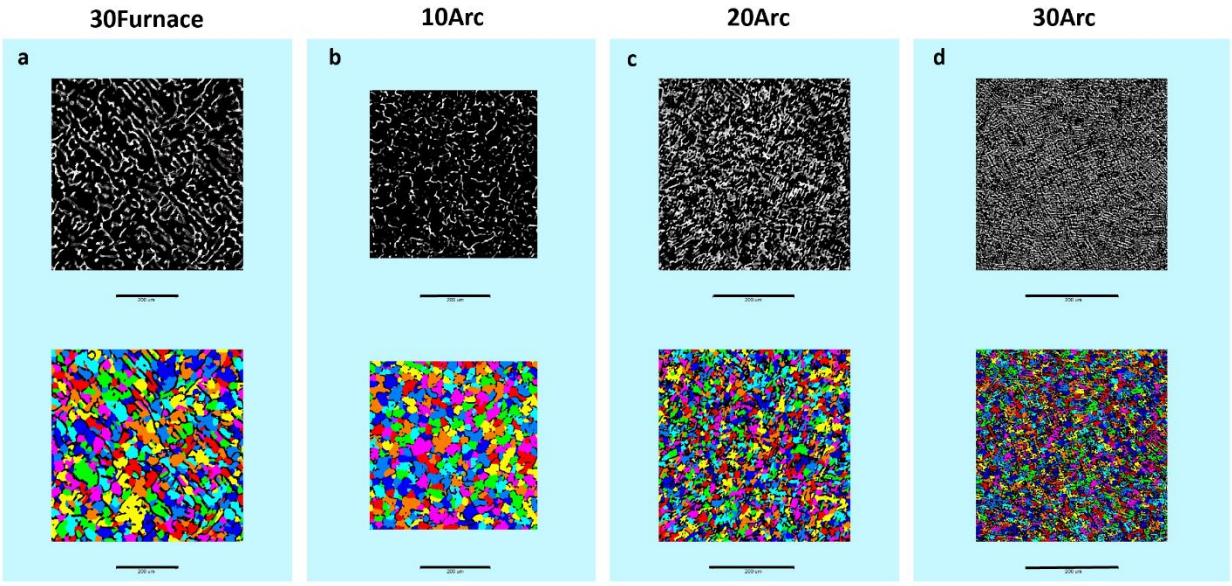

Figure S7. Examples of 2D slices from the X-ray tomography study and the separation of the image into pores. Samples shown are a) 30Furnace, b) 10Arc, c) 20Arc, and d) 30Arc.

Sample	Li deposition rate on top
30Arc	15 %
20Arc	10 %
10Arc	5 %
30Furnace	5 %

Table S1. Percentage of Li deposited on top of the copper current collector for each porous Cu sample.

Copper Height (%)	Li deposition rate in the foam
0 %→ 16.6 %	33 %
16.6 %→ 33.3 %	27 %
33.3 % → 50 %	18.75 %
50 % → 66.6 %	10.5 %
66.6 % → 83.3 %	6.25 %
83.3 % → 100 %	4.5 %

Table S2. Percentage of Li deposited in each sub-volume in the porous copper samples for simulation. Here, 0 % in thickness corresponds to the porous Cu surface closest to the separator.

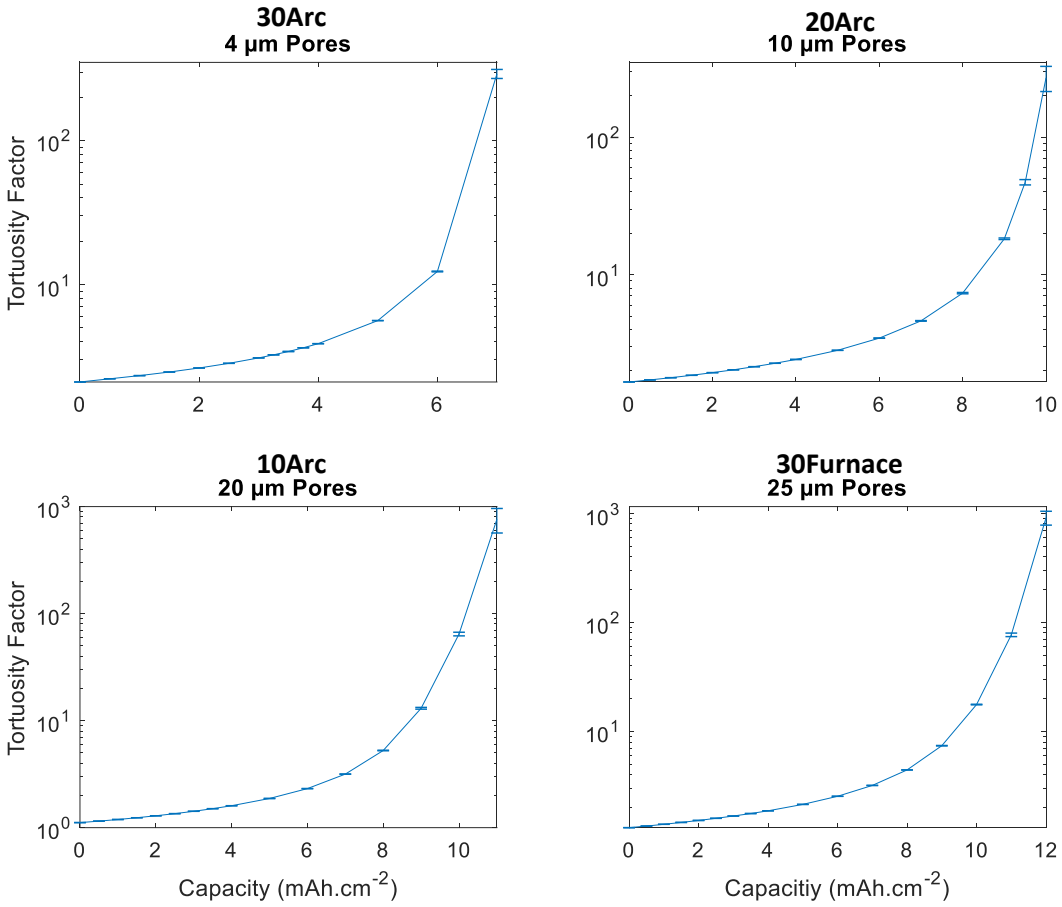

Figure S8. Tortuosity factor as a function of capacity with the associated error for each current collector. Samples names are listed on the figure.

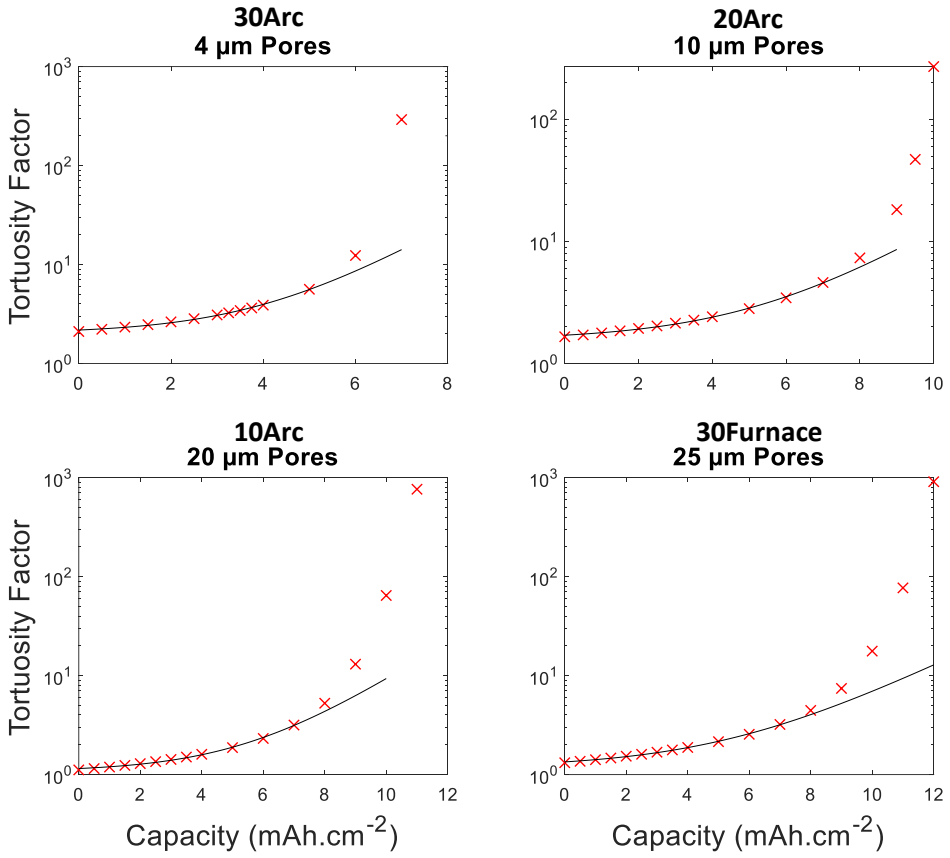

Figure S9. The evolution of the tortuosity factor as a function of the capacity was fit using Eq. S1.

$$T(c) = \alpha_0 + \alpha_1 e^{\alpha_2 c} \quad \text{(Eq.S1)}$$

Only the region before the sharp rise in tortuosity, *i.e.* 5 mA·cm^{-2} for the 4 µm pores and 7 mA·cm^{-2} for the rest, was used for the fits; the fit parameters can be found in Table S3. The second region could not be fitted using the same function. In the figure, the tortuosity factor from the simulations (same data as figure S8) is shown in red and the associated exponential fits to the data before the steep increase in tortuosity are shown with a solid black line. Samples names are listed on the figure.

	α_0	α_1	α_2	R^2
Arc30	2.0086	0.1702	0.6096	0.9980
Arc20	1.5513	0.1555	0.4239	0.9981
Arc10	1.0696	0.0816	0.4619	0.9979
Furnace30	1.1700	0.1730	0.3509	0.9988

Table S3. Fit parameters from the function given in Eq.S1 and the associated coefficients of determination R^2.

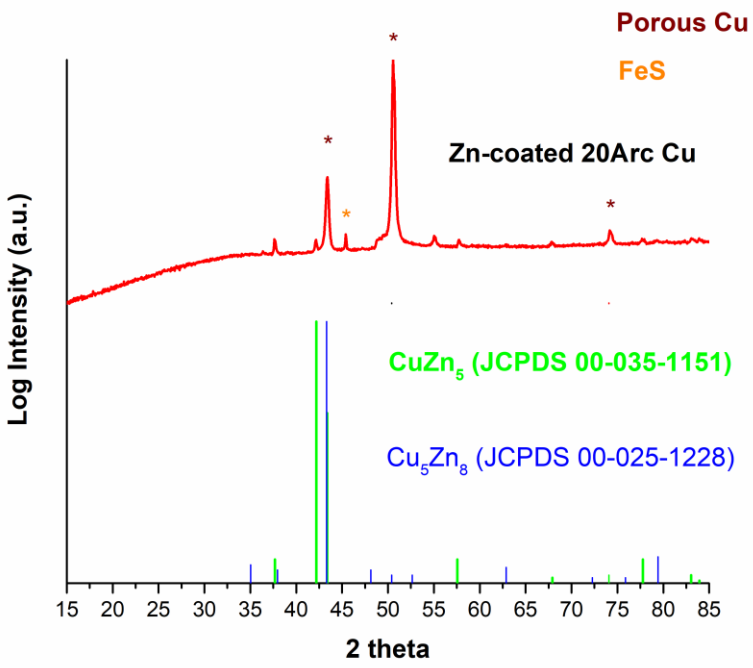

Figure S10. X-ray diffraction pattern of the Zn-coated 20Arc Cu sample after dealloying, coating, and cleaning. Diffraction peaks belonging to Cu metal for FeS are indicated with *.

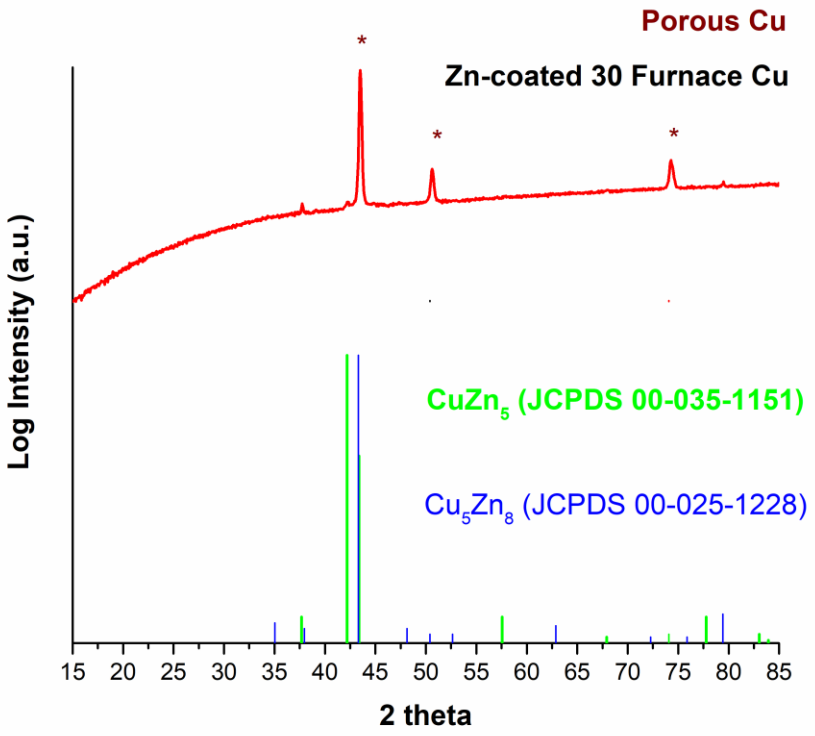

Figure S11. X-ray diffraction pattern of the Zn-coated 30Furnace Cu sample after dealloying, coating, and cleaning. Peaks corresponding to pure Cu are marked with *.

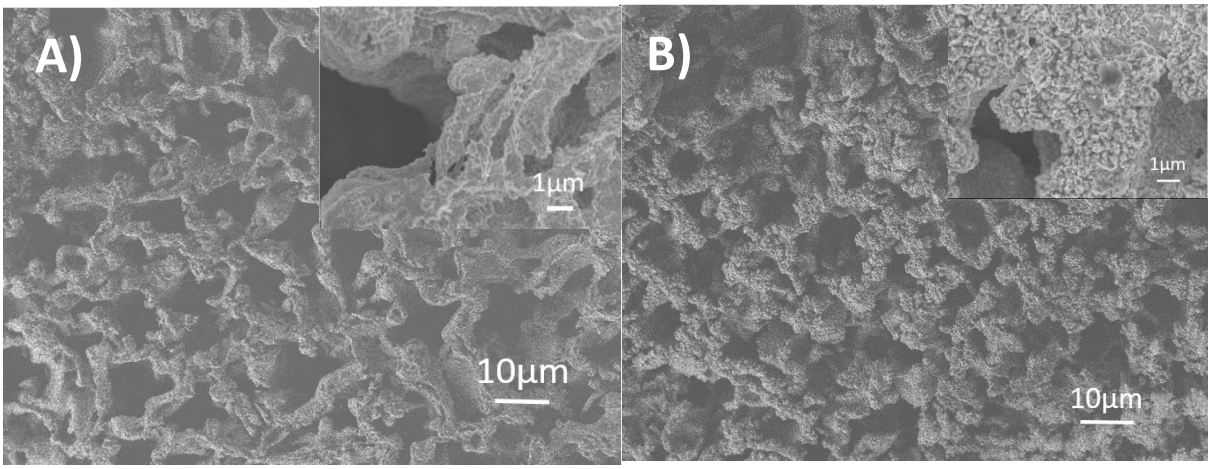

Figure S12. Top-view SEM images of the A) as made-20Arc Cu and B) Zn-coated 20Arc Cu samples. The images look very similar indicating the formation of a conformal coating.

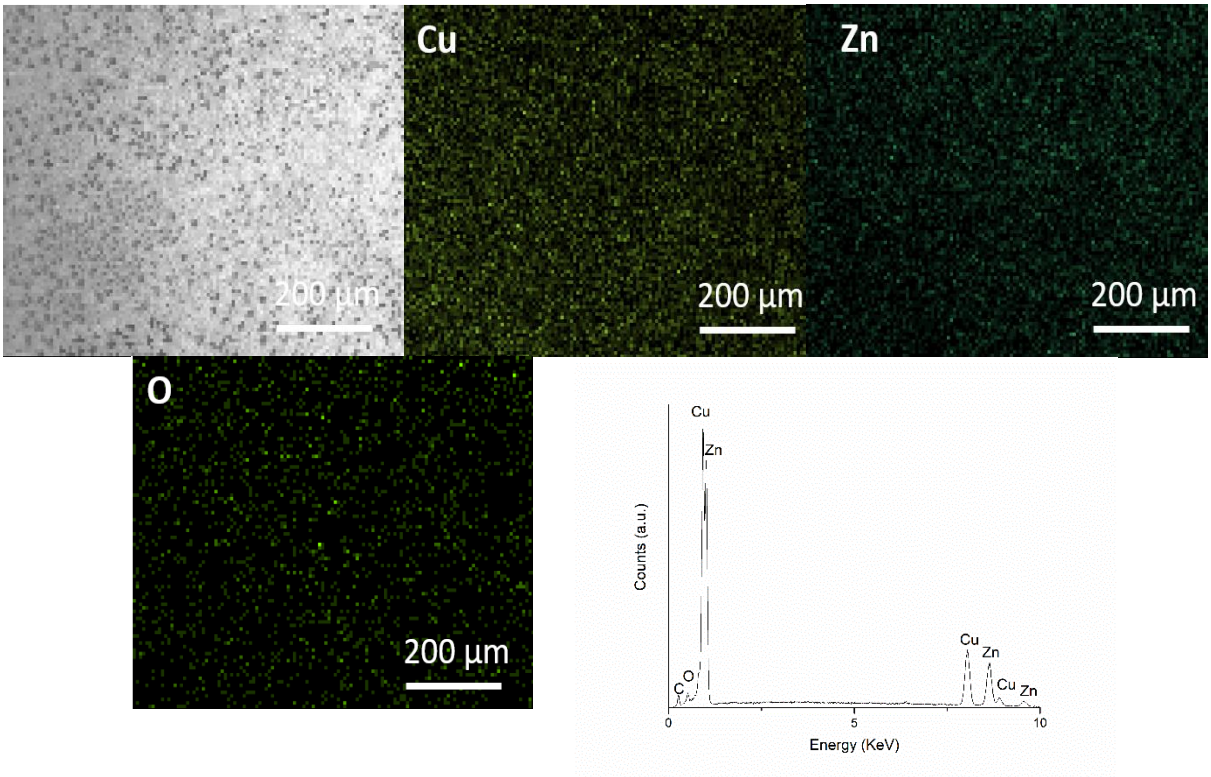

Figure S13. Top-view EDS mapping for the 20Arc Cu sample after Zn deposition showing the maps of Cu, Zn, O and the overall EDS energy spectrum. Uniform distributions of Cu and Zn indicate a homogeneous coating.

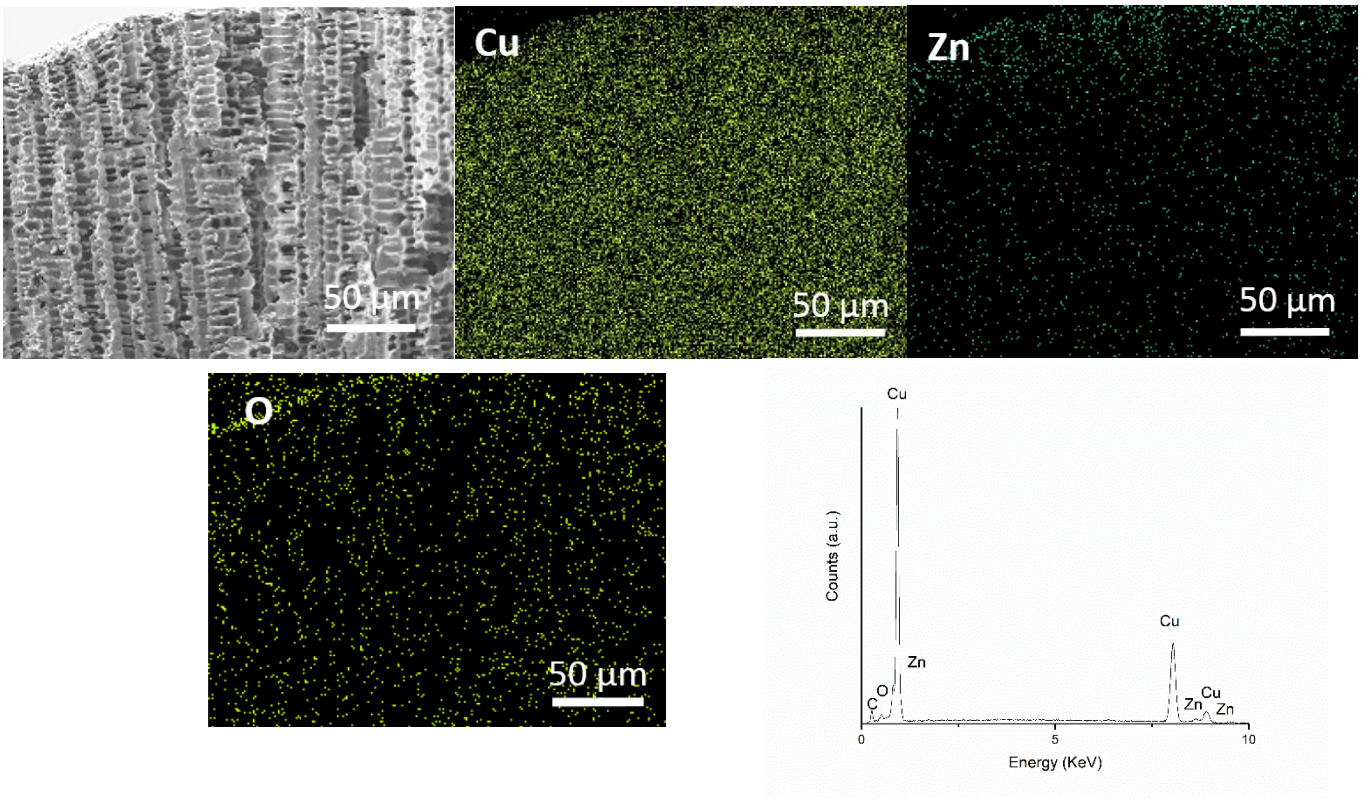

Figure S14. Cross-Sectional EDS mapping for the 20Arc Cu sample after Zn deposition showing the maps of Cu, Zn, O and the overall EDS energy spectrum. Uniform distributions of Cu and Zn indicate a homogeneous coating.

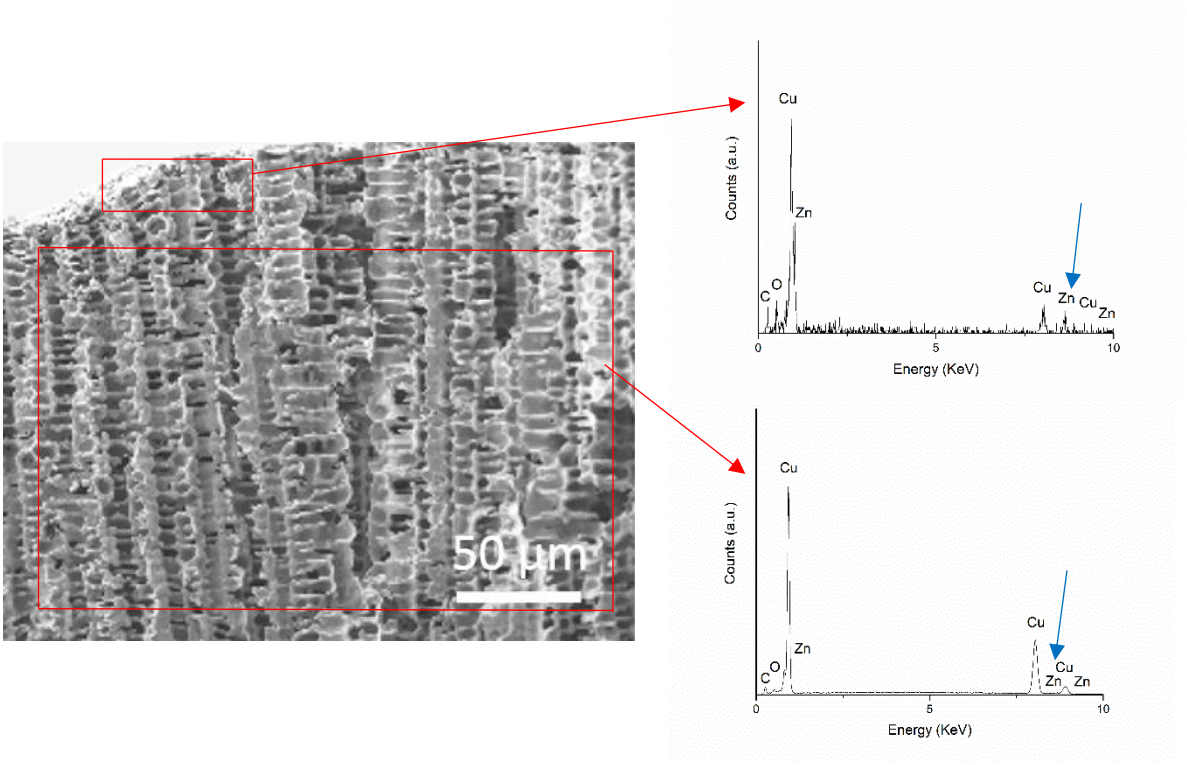

Figure S15. Cross-Sectional EDS mapping for the 20Arc Cu sample after Zn deposition showing EDS energy spectrum for the top part and middle part of the sample. There is a clear difference in Zn coating as reflected by the Zn k-α peak (blue arrows)

20 Arc	**Top (wt%)**	**Middle (wt%)**	**Top (vol %)**	**Middle (vol %)**
O (K-α)	5.75	0.64	8.3	0.9
Cu (K-α)	55.04	96.5	48.7	95.5
Zn (K-α)	**39.20**	**2.86**	**43.0**	**3.6**
Calculated Zn-Thickness (nm)			**425**	**35**

Table S4. Zn-coated 20Arc Cu weight % for the three main elements in the sample (O, Cu and Zn) from EDS mapping. The Zn-thickness in the middle of the cross-section is 33-40 nm based on the Zn weight % and the Zn-coating thickness observed in Figure S15 on the top of the sample.

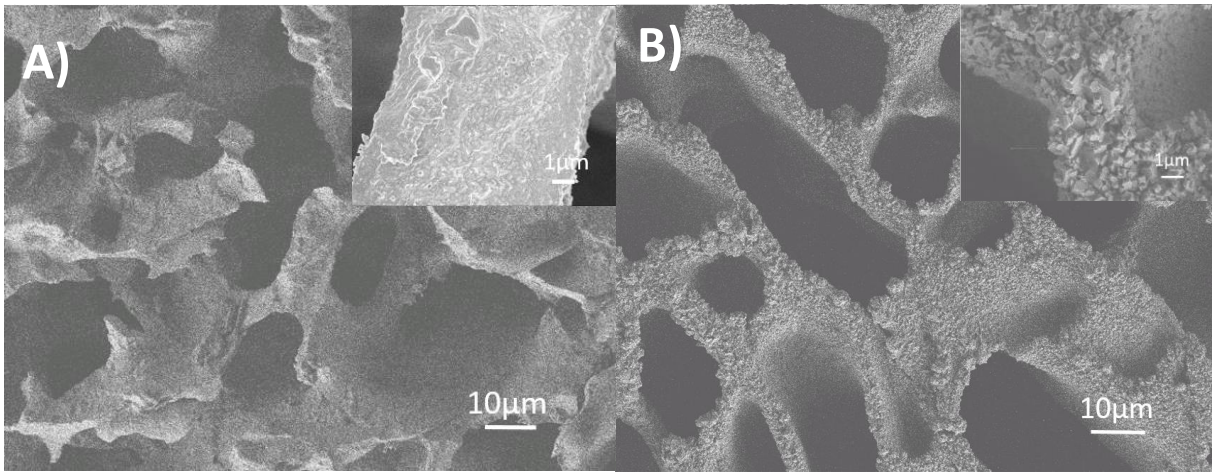

Figure S16. Top-view SEM images of the A) as made-30Furnace Cu and B) Zn-coated 30Furnace Cu samples. The images look very similar indicating the formation of a conformal coating.

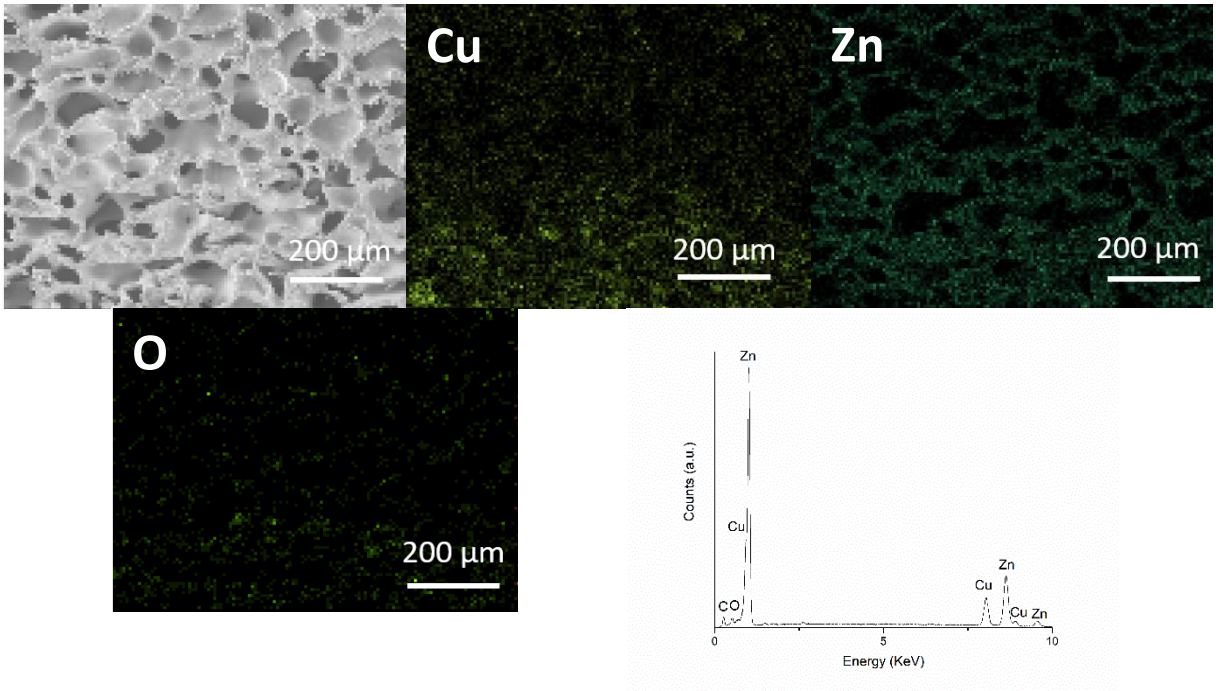

Figure S17. Top-view EDS mapping for the 30Furnace Cu sample after Zn deposition showing the maps of Cu, Zn, O and the overall EDS energy spectrum. Uniform distributions of Cu and Zn indication a homogeneous coating.

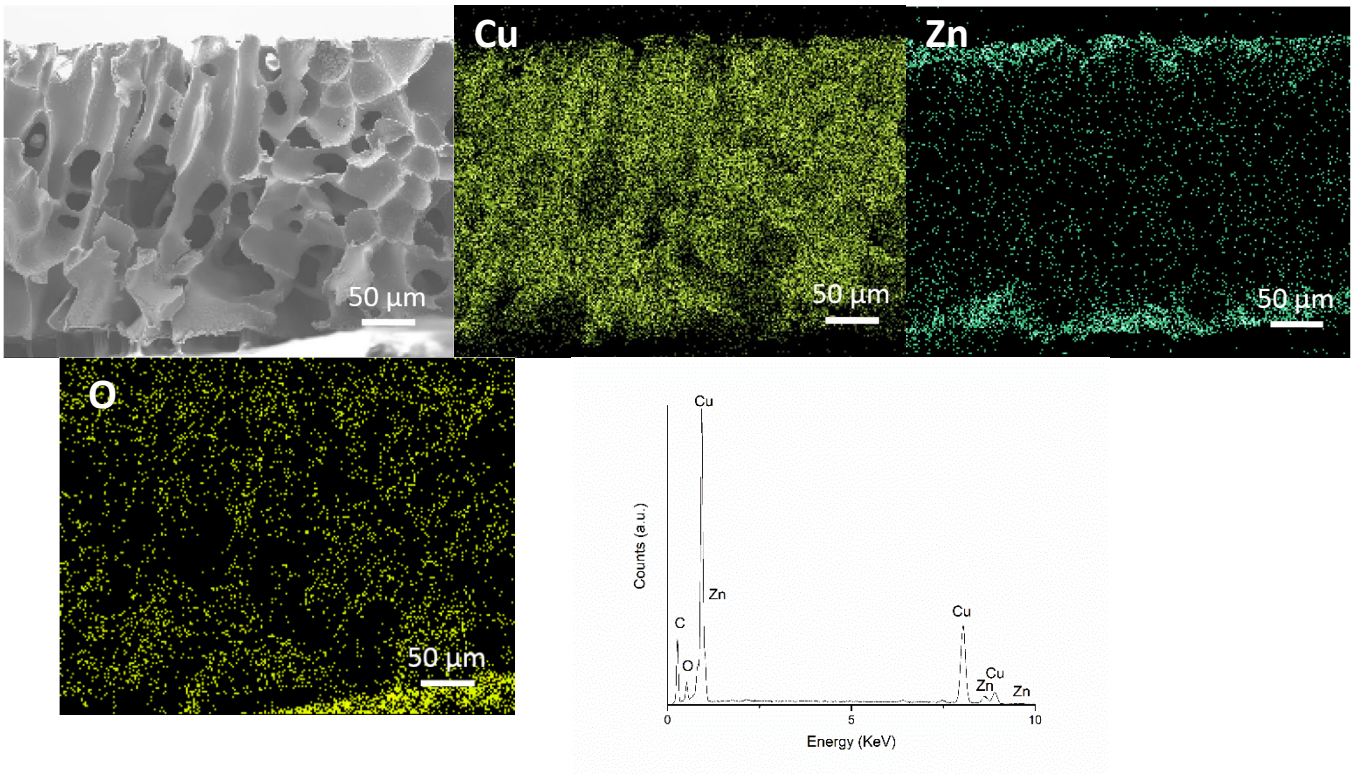

Figure S18. Cross-sectional EDS mapping for the 30Furnace Cu sample after Zn deposition showing the maps of Cu, Zn, O and the overall EDS energy spectrum. Uniform distributions of Cu and Zn indication a homogeneous coating.

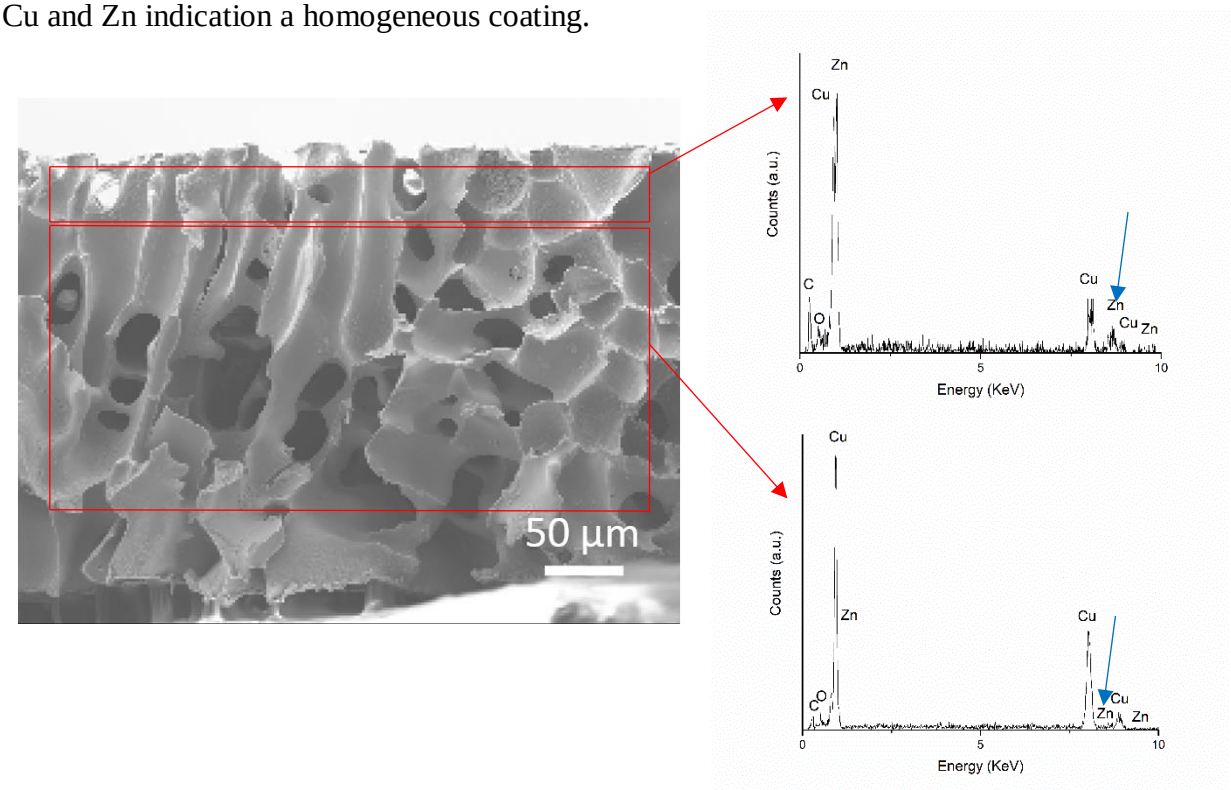

Figure S19. Cross-Sectional EDS mapping for the 30Furnace Cu sample after Zn deposition showing EDS energy spectrum for the top part and middle part of the sample. There is a clear difference in Zn coating as reflected by the Zn k-α peak (blue arrows)

30 Furnace	Top (wt. %)	Middle (wt. %)	Top (vol. %)	Middle (vol. %)
O (K-α)	1.26	0.74	1.7	1.1
Cu (K-α)	40.05	97.26	34.6	96.4
Zn (K-α)	**58.69**	**2.00**	**63.7**	**2.5**
Calculated Zn-Thickness (nm)			**1100**	**44**

Table S5. Zn-coated 30Furnace Cu weight % for the three main elements in the sample (O, Cu and Zn) from EDS mapping. The Zn-thickness in the middle of the cross-section is 15-18 nm based on the Zn weight % and the Zn-coating thickness observed in Figure S19 on the top of the sample.

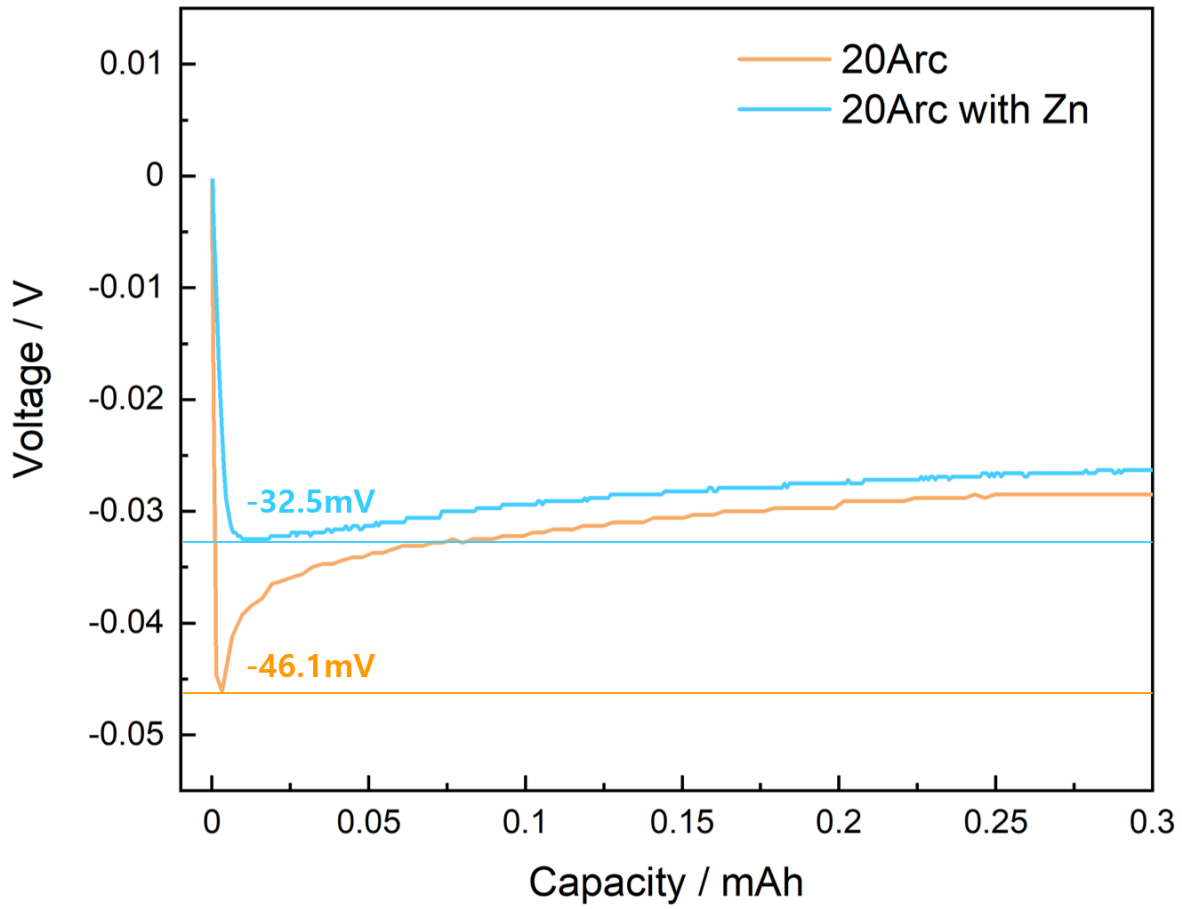

Figure S20. The voltage profile of Li deposition on the 20Arc and the Zn-coated 20Arc sample. The nucleation overpotential is labelled with a horizontal line for each sample. Zn coating results in a significant decrease in nucleation overpotential.

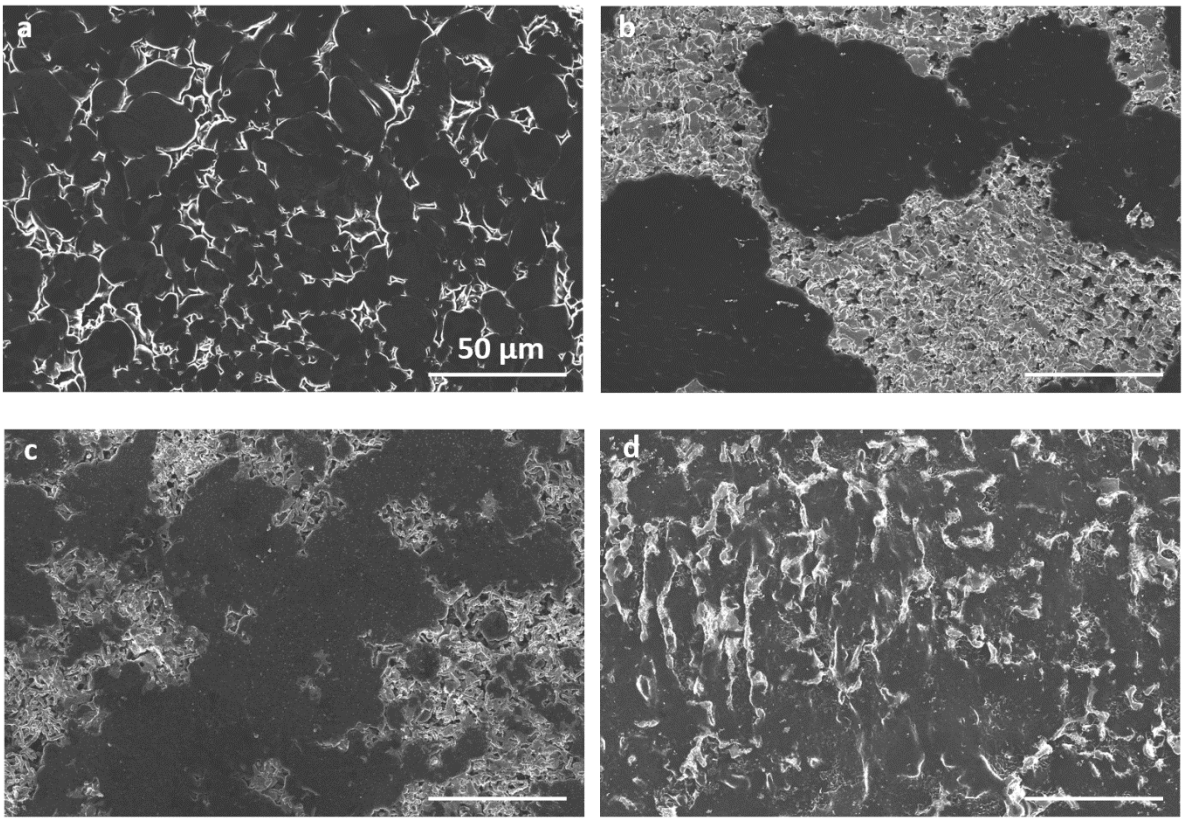

Figure S21. The top-view images of the Li morphology of Fig. 4 in the main text: a) 30Arc; b) 20Arc; c) 10Arc; d) 30Furnace.

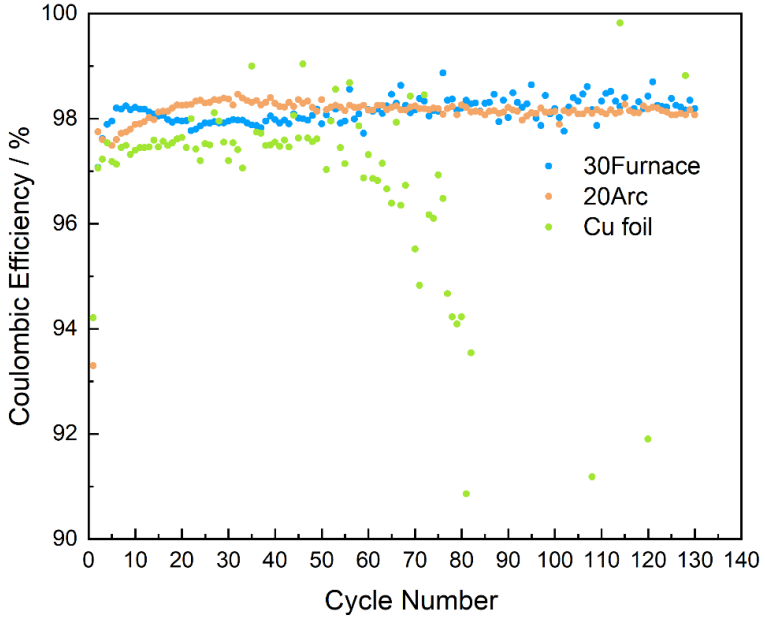

Figure S22. The Li plating/stripping coulombic efficiency of the 30Furnace, 20Arc and Cu foil. 1 M (LiTFSI) in DOL:DME (1:1 in volume) with 2% $LiNO_3$ is used. Current density of 0.5mA/cm^2 was used to plate 1mAh.cm^2 of Li in each cycle.

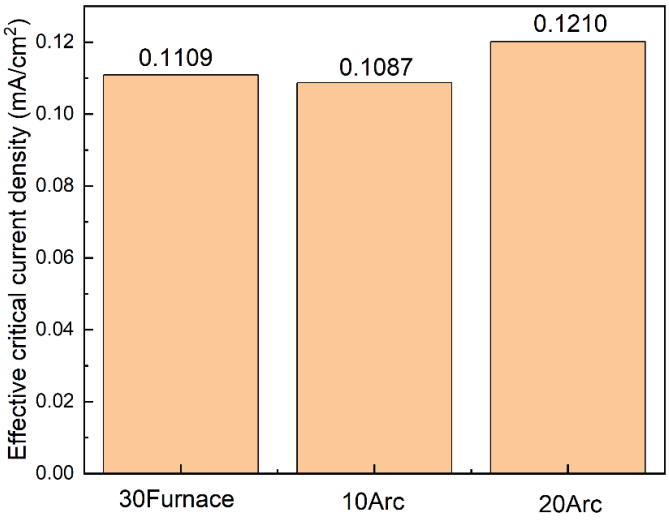

Figure S23. The effective critical current density of the porous coppers calculated based on effective surface area from CT quantification.

REFERENCES

(1) Cooper, S. J.; Bertei, A.; Shearing, P. R.; Kilner, J. A.; Brandon, N. P. TauFactor: An Open-Source Application for Calculating Tortuosity Factors from Tomographic Data. *SoftwareX* **2016**, *5*, 203–210. https://doi.org/10.1016/j.softx.2016.09.002.

APPENDIX B

Supplementary Information for Chapter 3: Increasing the lifetime of thick porous Cu current collectors for Lithium Metal Batteries via asymmetric lithiophilic coating

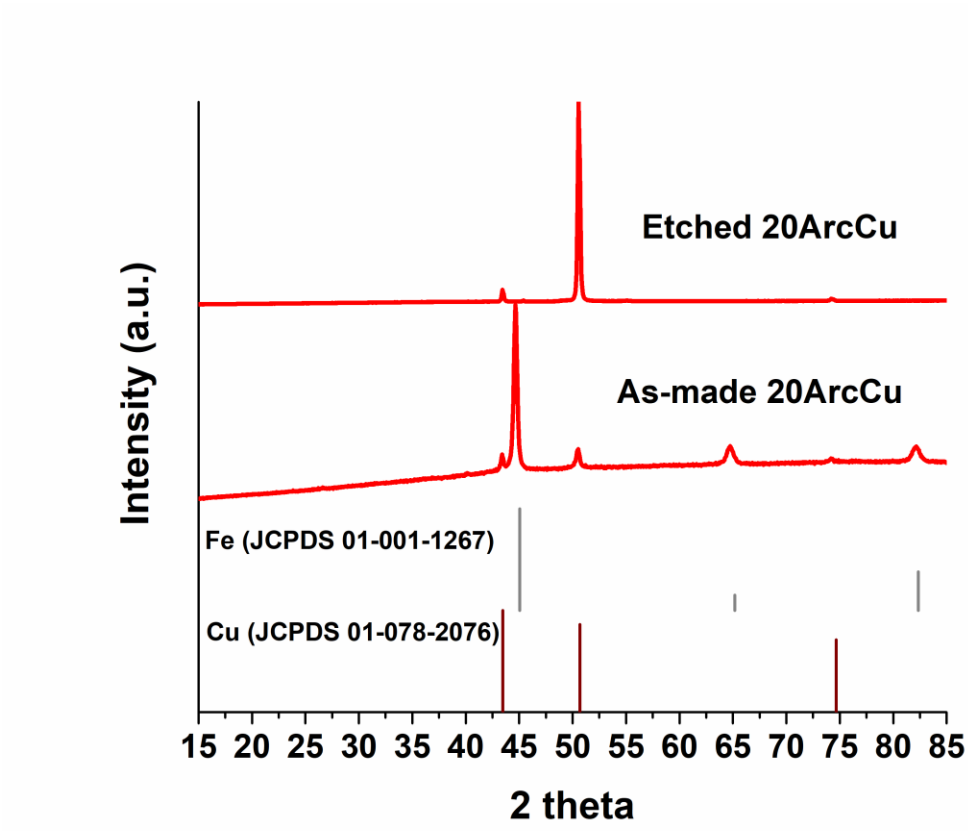

Figure S1. X-ray diffraction patterns of Cu-Fe phase separated metal with 20at%Cu-80at%Fe composition made using arc melting method before and after acid etching and cleaning. Cu and Fe reference pattern are included for metal identification.

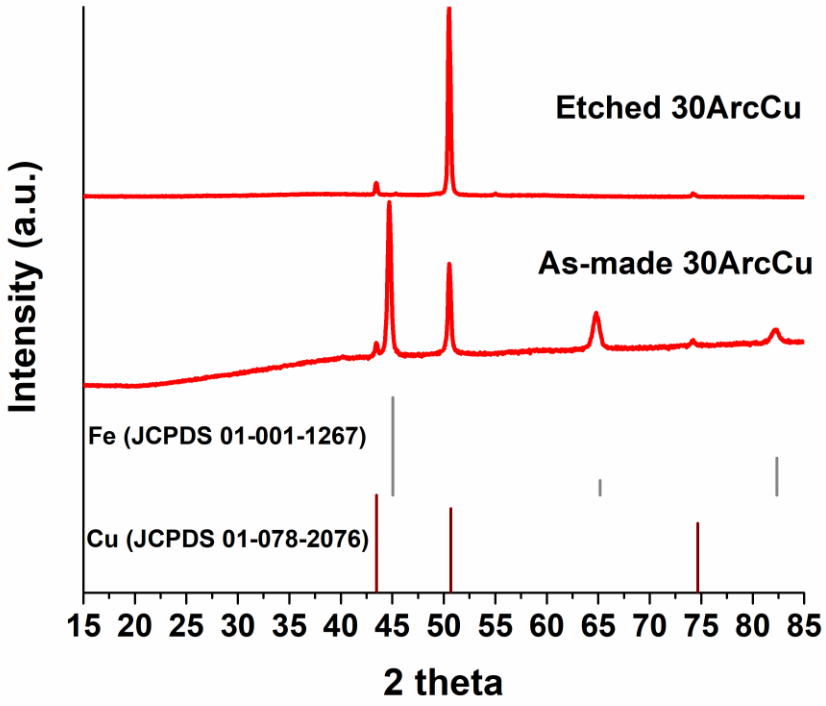

Figure S2. X-ray diffraction patterns of Cu-Fe phase separated metal with 30at%Cu-70at%Fe composition made using arc melting method before and after acid etching and cleaning. Cu and Fe reference pattern are included for metal identification.

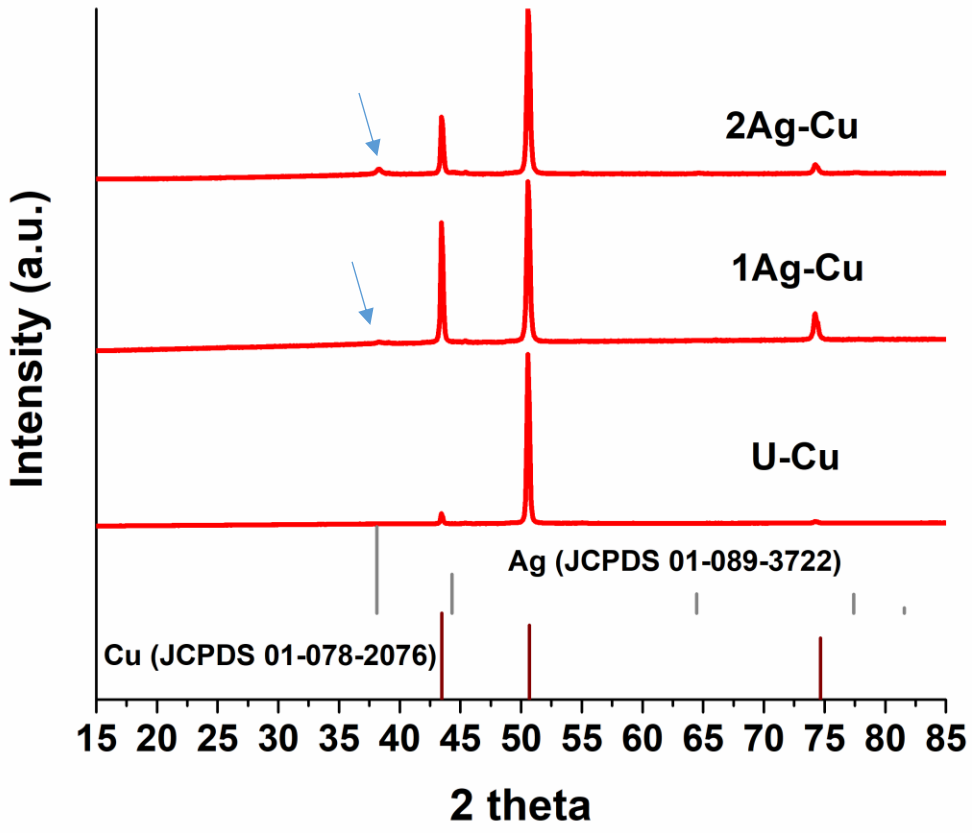

Figure S3. X-ray diffraction patterns of uncoated 3D porous Cu (U-Cu), after asymmetrically coating with Ag (1Ag-Cu) and after symmetrically coating with Ag composition(2Ag-Cu). For U-Cu sample only Cu metal is identified. For both the 1Ag-Cu and the 2Ag-Cu samples, only the most intense Ag peak at 38.1˚ can be observed (blue arrow), indicating the presence of Ag in the samples, and this peak is more intense for the homogenously coasted sample than for the gradient coated sample, as expected. Cu and Ag reference pattern are included for metal identification.

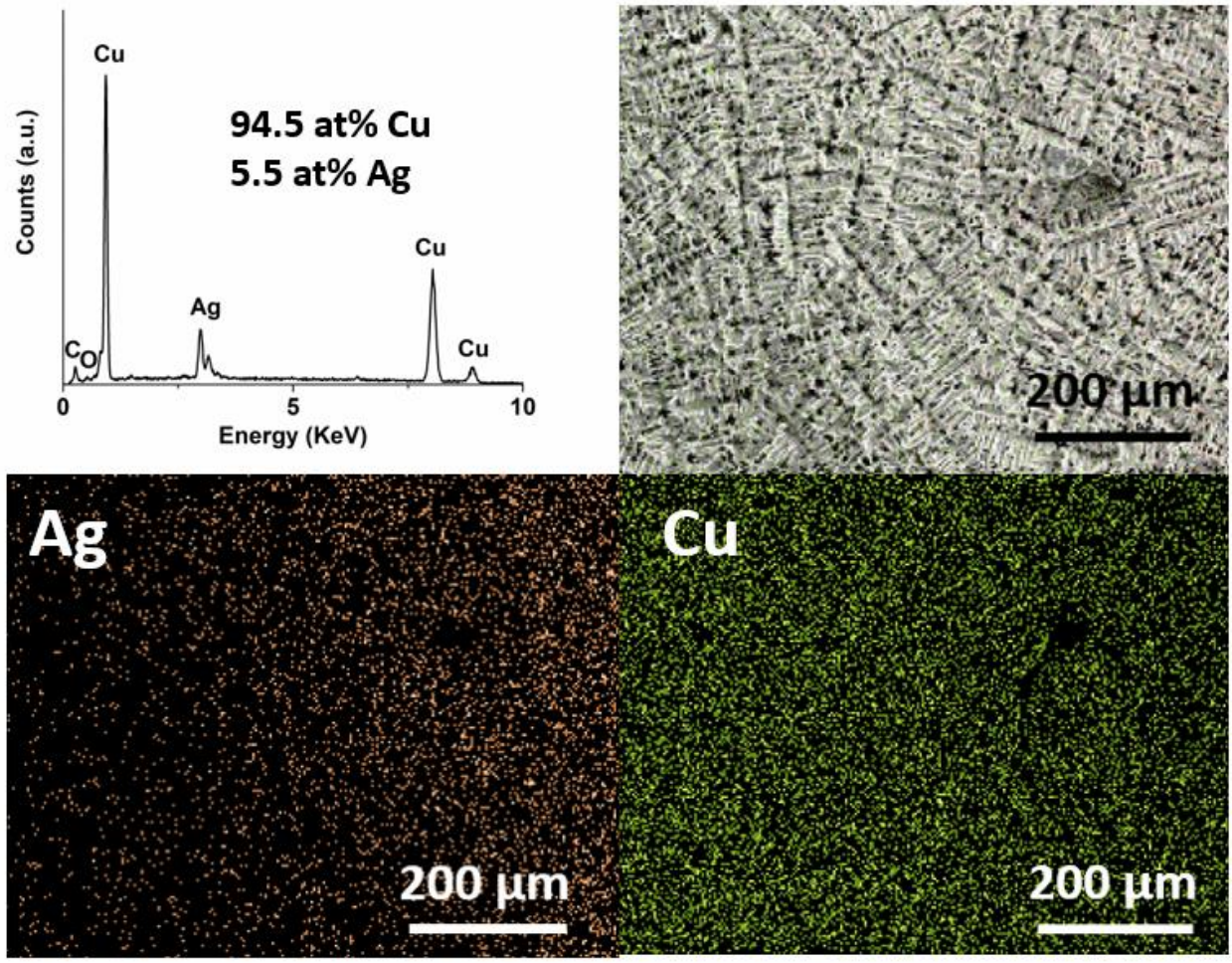

Figure S4. Top-View (top-left) EDS spectrum and top-view (top-right) image for the coated side of the asymmetrically Ag-coated Cu (1Ag-Cu). There is about 5 at% Ag uniformly distributed on this side of the Cu sample, as shown in the Ag (bottom-left) and Cu (bottom-right) mapping.

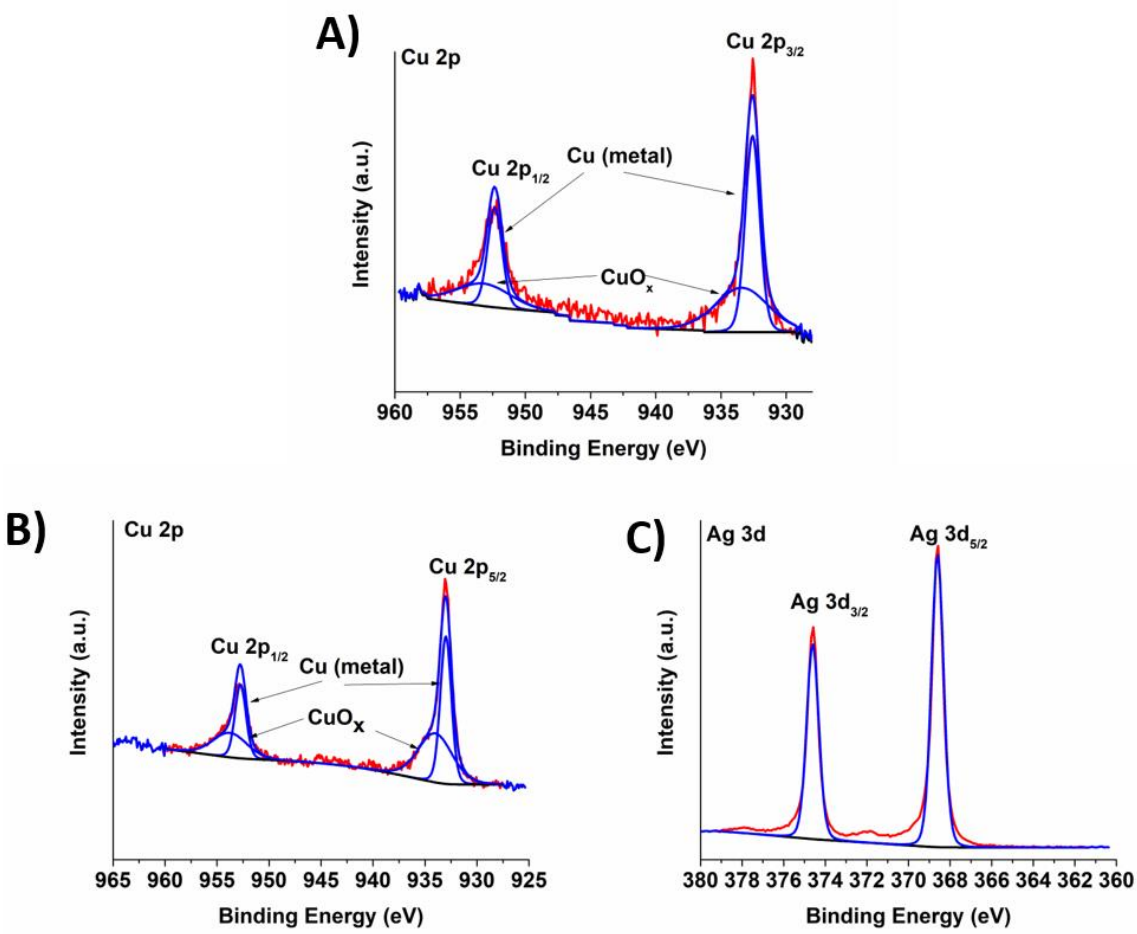

Figure S5. XPS of an (A) uncoated Cu (U-Cu) sample after acid etching and cleaning. The Cu2p spectrum shows that the sample is composed of Cu with a small amount of CuO_x. Figures S5B and S5C show the XPS for the coated side of the asymmetrically Ag-coated Cu (1Ag-Cu) sample. The Cu2p spectrum shows that the sample's surface is composed of Cu with a small amount of CuO_x and the Ag3d spectrum shows Ag metal peaks located at 368.3 eV and 374.4 eV.

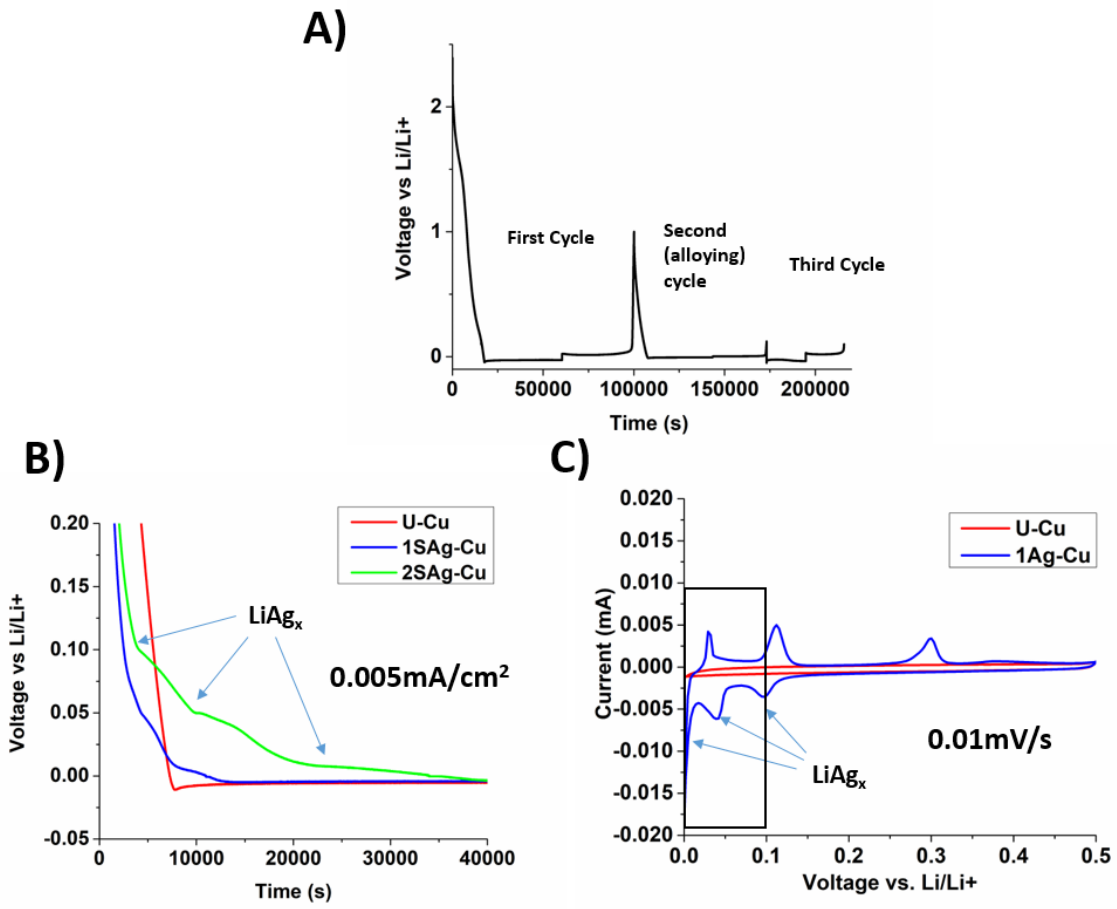

Figure S6. A) Electrochemical galvanostatic curves showing the protocol for the first three cycles used in all cells. The first cycle was run at 0.5mA/cm^2 with a stripping potential up to 1V vs. Li/Li$^+$. The second cycle was run at 0.005mA/cm^2 with a stripping potential up to 0.1 V vs. Li/Li$^+$. This low voltage cut-off was used to minimize the dissolution of $LiAg_x$ at every cycle (Fig. S6C). The third cycle (and following cycles) was ran at 1mA/cm^2 (6mAh/cm^2), 2mA/cm^2 (10mAh/cm^2) or 4mA/cm^2 (10mAh/cm^2) with a stripping potential up to 0.1 vs. Li/Li$^+$. B) Detailed deposition curve of the second (alloying) cycle ran at 0.005 mA/cm^2 for the three type of samples. The curves show that the Ag-coated samples have three $LiAg_x$ plateaus and the uncoated sample shows no alloy plateau and a higher nucleation overpotential. C) Cyclic voltammetry of the uncoated and Ag-coated Cu samples showing the three peaks of $LiAg_x$ alloy formation. The black frame contains the potentials below which galvanostatic cycling occurred after third cycle.

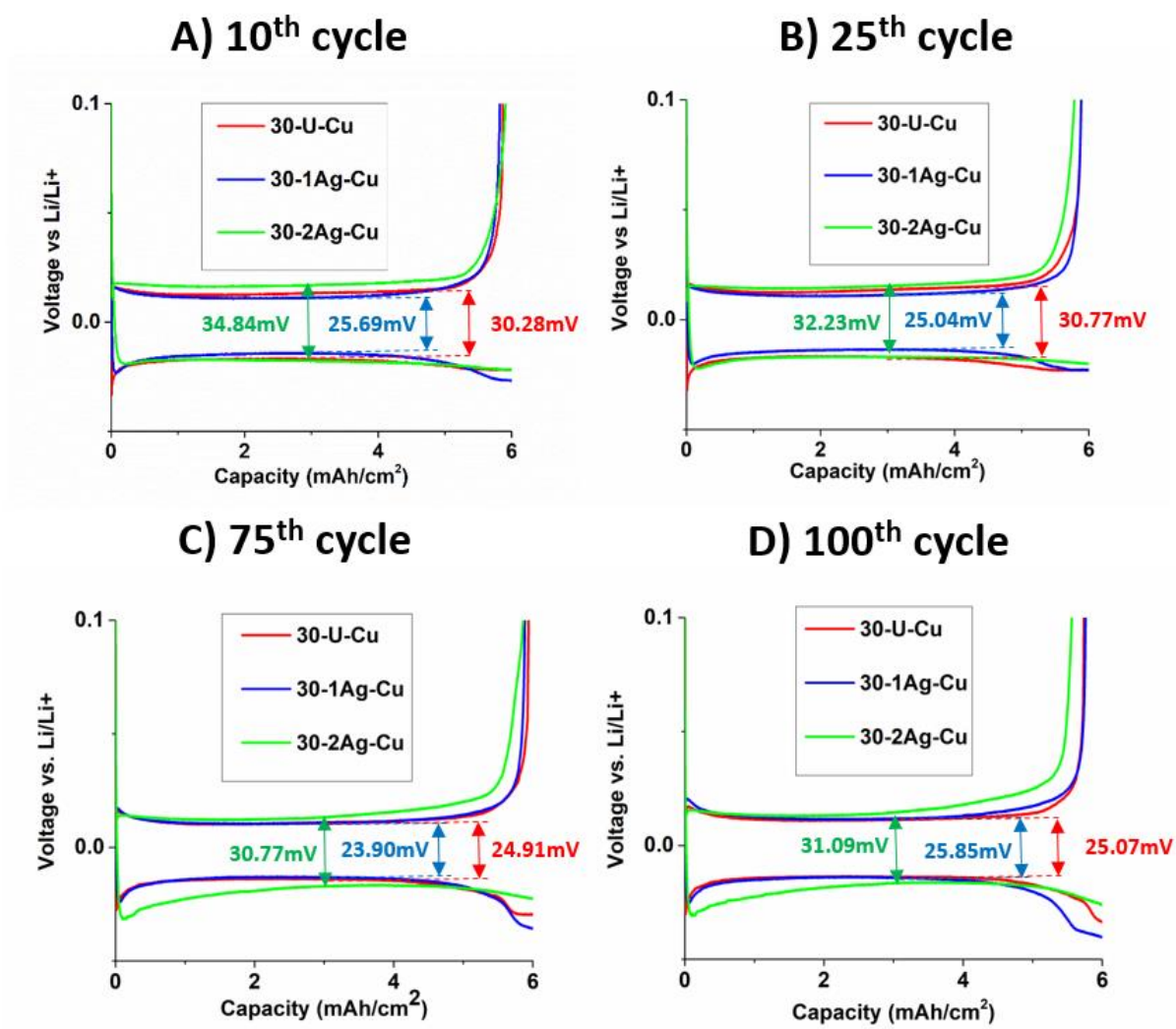

Figure S7. Galvanostatic potential curves for 30-U-Cu(red), 30-1Ag-Cu(blue) and 30-2Ag-Cu(green) materials cycled at the A)10th, B)25th, C)75th and D)100th cycle. The hysteresis overpotential values for each sample is shown in the graphs. The cycling parameters are 1mA/cm^2 and 6mAh/cm^2.

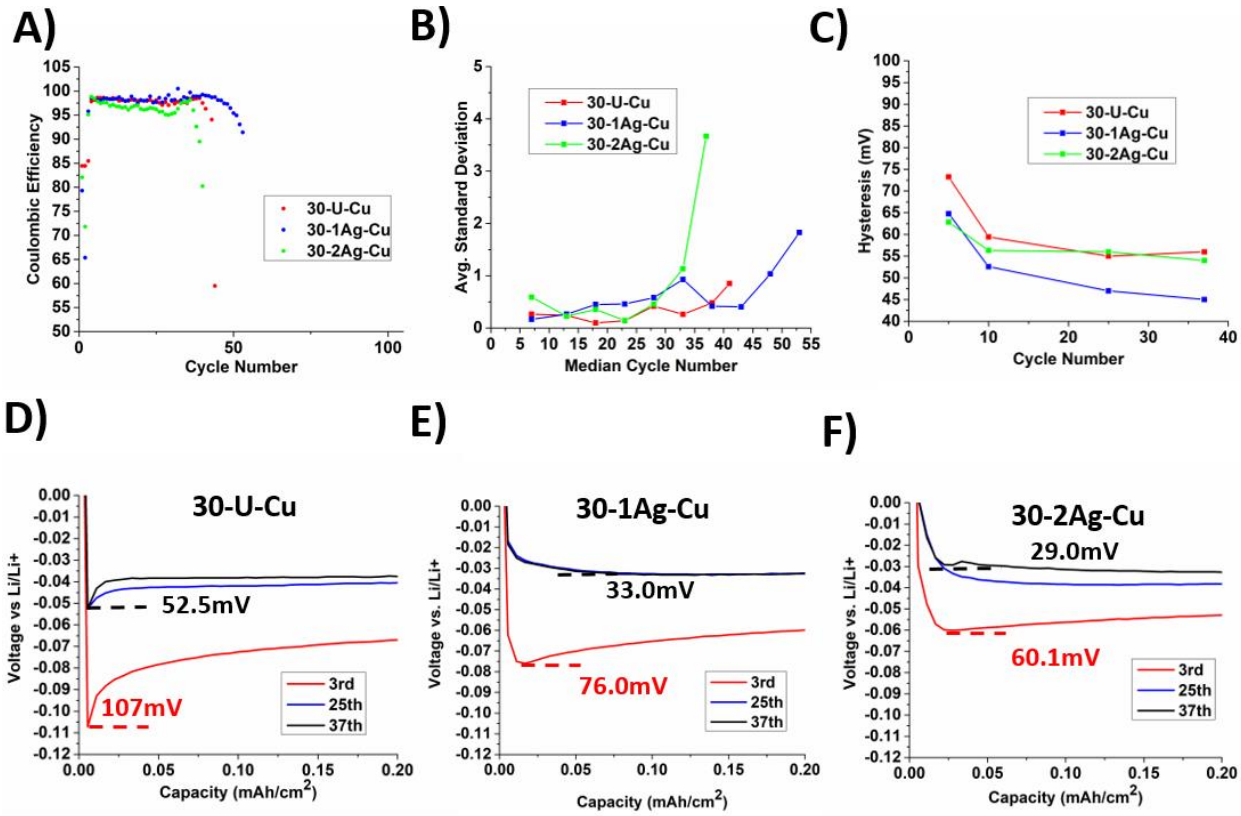

Figure S8. Electrochemical galvanostatic cycling of the 30-Cu samples cycled at 4mA/cm^2 and 10mAh/cm^2. Plots show the A) coulombic efficiency vs. cycle number, B) the standard deviation of the CE, averaged over every 5 cycles (excluding the first 3 cycles) and C) the hysteresis between plating and stripping at select cycles. For all measurements, the 30-1Ag-Cu materials show the best electrochemical performance, including longest cycle life, lowest fluctuations, and smallest hysteresis. The nucleation overpotential at various cycles for the D) 30-U-Cu, E) 30-1Ag-Cu and the F) 30-2Ag-Cu samples. Both of the Ag-coated samples showed a lower nucleation over potential than the bare Cu. In this case, the 30-2Ag-Cu sample actually showed the lowest nucleation overpotential. This is likely because lithium was plating on top of the pores which had a lithiophilic surface (Fig. S9D and Fig. S9E) during its short lifespam, and inside the pores for the case of the 30-1Ag-Cu material (Fig. S9G and Fig. S9H).

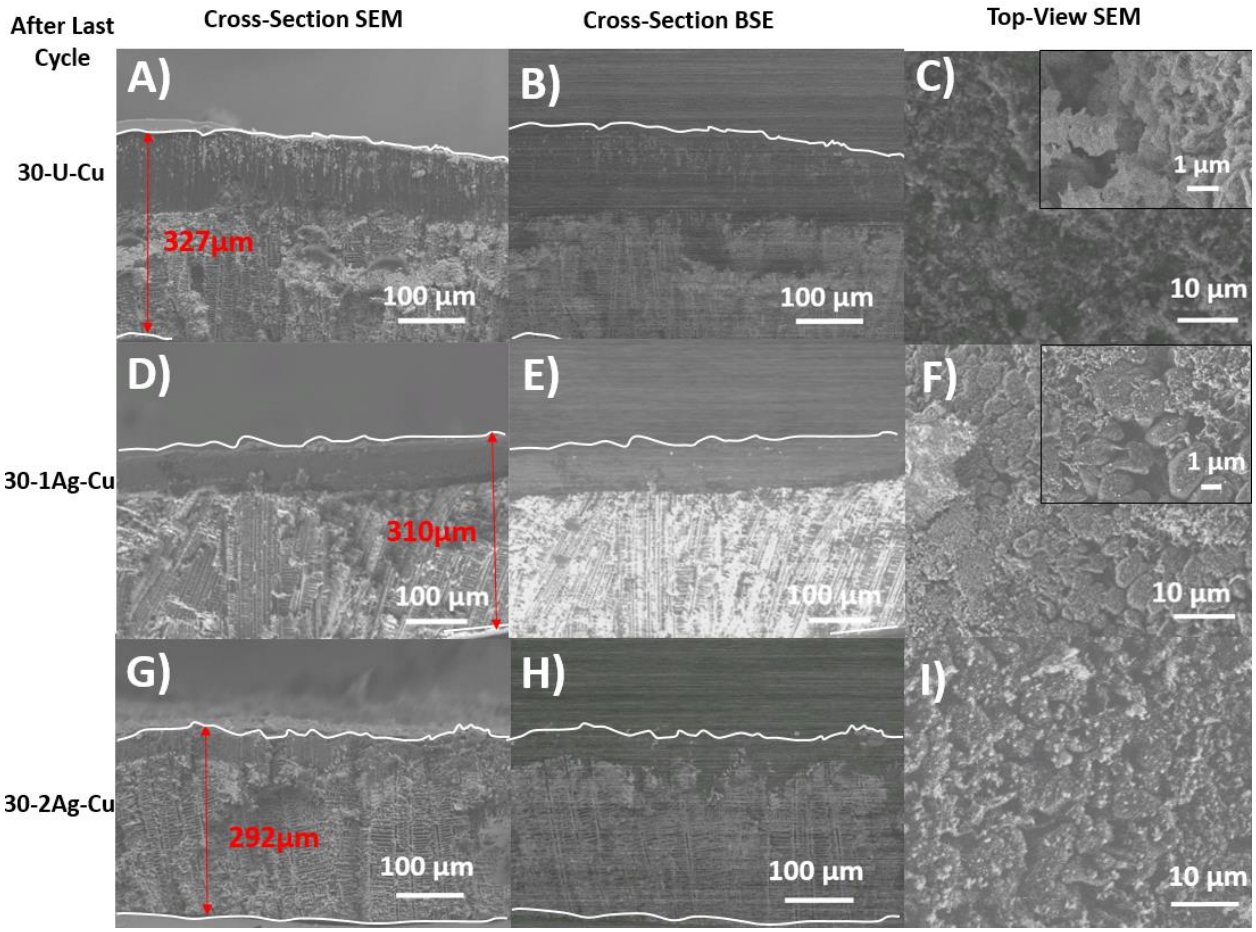

Figure S9. Cross-sectional secondary-electron SEM image (A,D,G), cross-sectional back-scattered electron (BSE) SEM images (B,E,H) and top-view secondary-electron SEM image (C,F,I) of 30-U-Cu materials (A,B,C), of 30-1Ag-Cu materials (D,E,F) and of 30-2Ag-Cu materials (G,H,I). The images for the 30-U-Cu sample were collected after a Li deposition post-44th cycle. The images for the 30-1Ag-Cu sample were collected after a Li deposition post-53rd cycle. The images for the 30-2Ag-Cu sample were collected after a Li deposition post-40th cycle. Cycling parameters were 4mA/cm^2 and 10mAh/cm^2 for all samples. White lines are traced on cross-sectional images to show the lower and upper edges of the sample. Lithium plates mostly on top of the uncoated sample, as shown by the dark strip in the BSE SEM image (B). The asymmetrically coated sample shows a small amount of Li deposition deposited inside the pores but a big amount still deposits on top (E). The symmetrically coated sample shows some Li deposition inside the pores and most of it deposited on top, but this sample had a short lifetime of 40 cycles (E). The overall electrode thickness of 20-U-Cu (327µm) after the 44th cycle is much higher than that of 20-1Ag-Cu (310 µm) after the 53rd cycle, which is representative of the superior electrochemical performance of the 20-1Ag-Cu sample under these testing parameters. The 20-2Ag-Cu sample had an overall electrode thickness of 292µm after the 40th cycle. This short lifespan was likely due to the uneven deposition on top of the pores which lead to quick dendritic growth.

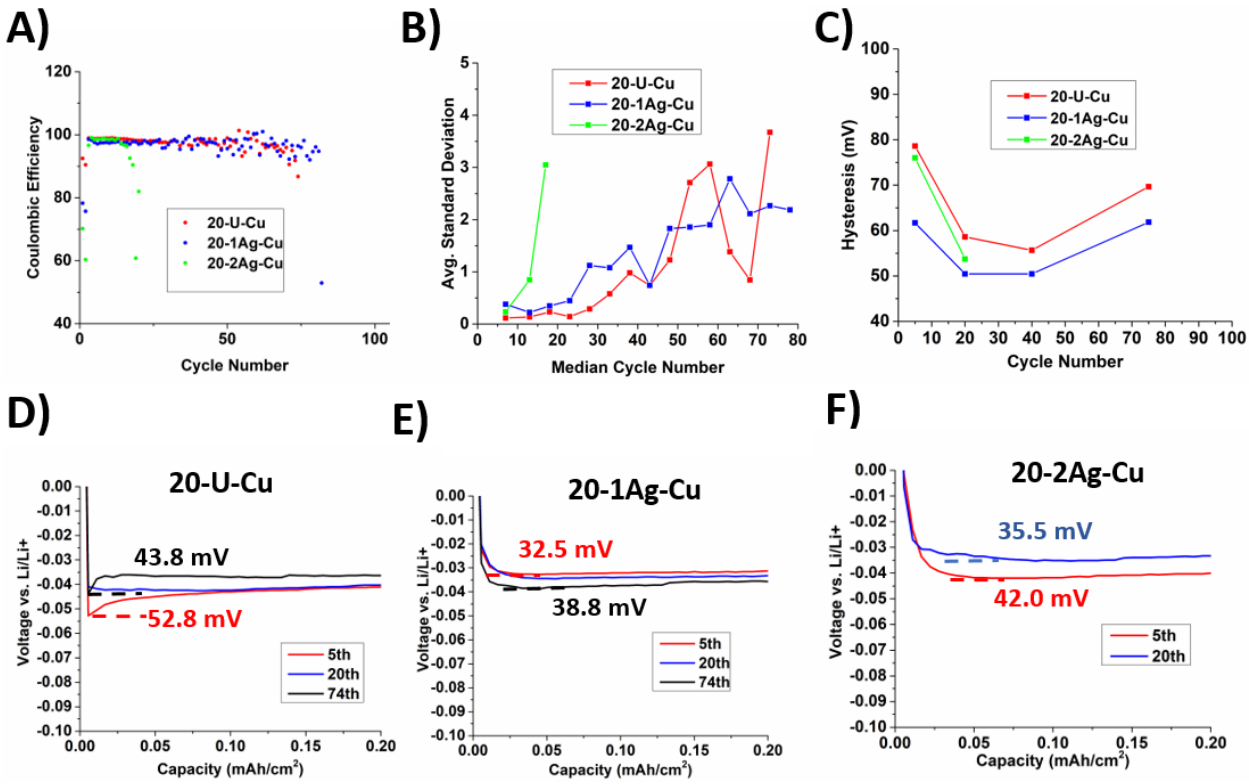

Figure S10. Electrochemical galvanostatic cycling of the 20-Cu samples cycled at 4mA/cm^2 and 10mAh/cm^2. Plots show the A) coulombic efficiency vs. cycle number, B) the standard deviation of the CE, averaged over every 5 cycles (excluding the first 3 cycles) and C) the hysteresis between plating and stripping at select cycles. For all measurements, the 20-1Ag-Cu materials show the best electrochemical performance, including longest cycle life, lowest fluctuations, and smallest hysteresis. The nucleation overpotential at various cycles for the D) 20-U-Cu, E) 20-1Ag-Cu and the F) 20-2Ag-Cu samples. In this case, the 20-1Ag-Cu sample possessed the lowest nucleation overpotential. This is likely because lithium plated inside the pores of the porous Cu current collector (Fig. S11D and Fig. S11E), while the other two samples had lithium plated on top of the pores during their shorter lifespam.

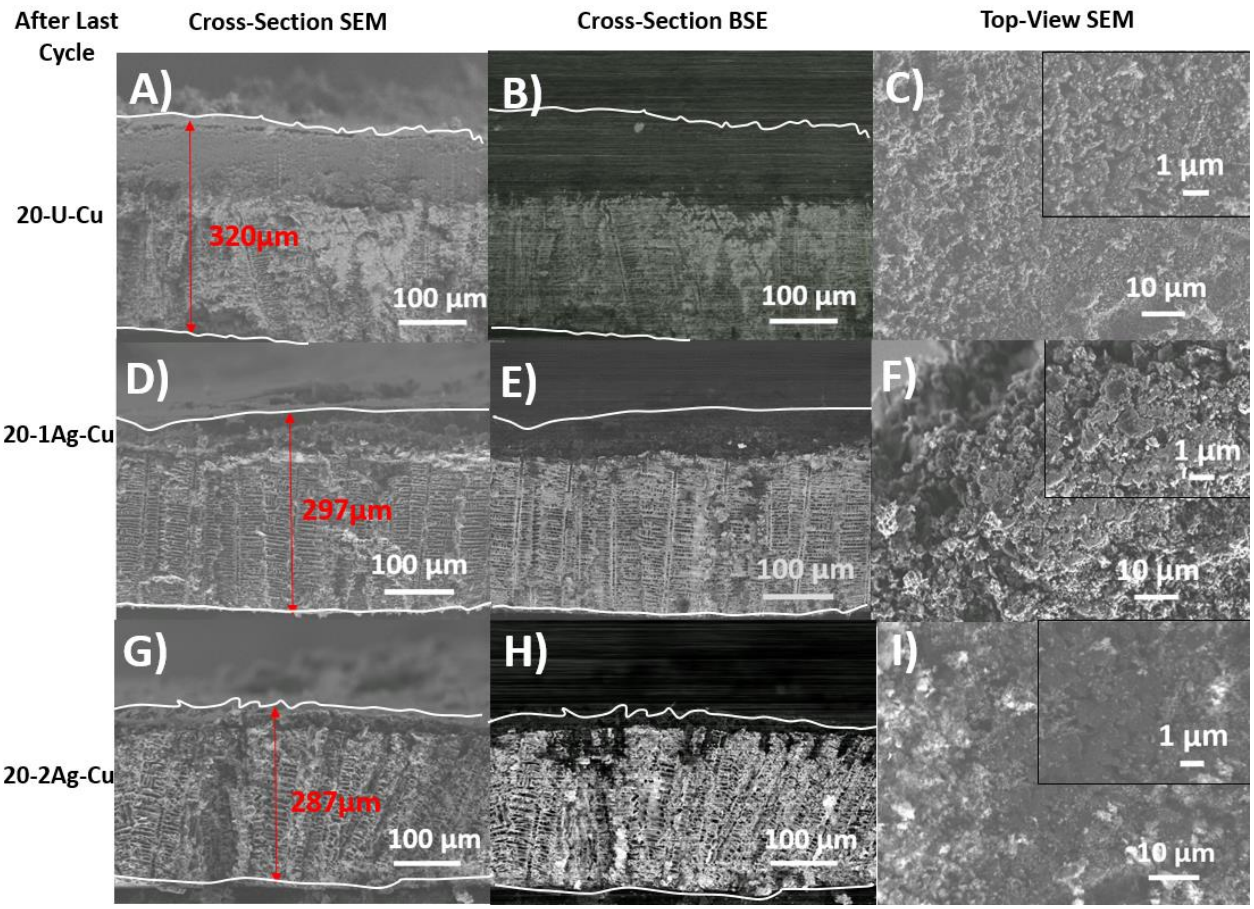

Figure S11. Cross-sectional secondary-electron SEM image (A,D,G), cross-sectional back-scattered electron (BSE) SEM images (B,E,H) and top-view secondary-electron SEM image (C,F,I) of 20-U-Cu materials (A,B,C), of 20-1Ag-Cu materials (D,E,F) and of 20-2Ag-Cu materials (G,H,I). The images for the 20-U-Cu sample were collected after a Li deposition post-74th cycle. The images for the 20-1Ag-Cu sample were collected after a Li deposition post-82nd cycle. The images for the 20-2Ag-Cu sample were collected after a Li deposition post-20th cycle. Cycling parameters were 4mA/cm^2 and 10mAh/cm^2 for all samples. White lines are traced on cross-sectional images to show the lower and upper edges of the sample. Lithium plates mostly on top of the uncoated sample, as shown by the dark strip in the BSE SEM image (B). The asymmetrically coated sample shows Li deposition a little bit further inside the pores but a big amount still deposits on top (E). The symmetrically coated sample shows some Li deposition inside the pores and most of it deposited on top, but this sample had a rather short lifetime of 20 cycles (E). The overall electrode thickness of 20-U-Cu (320µm) after the 74th cycle is much higher than that of 20-1Ag-Cu (297 µm) after the 82nd cycle, which is representative of the superior electrochemical performance of the 20-1Ag-Cu sample under these testing parameters. The 20-2Ag-Cu sample had an overall electrode thickness of 287µm after the 20th cycle. This short lifespan was likely due to the uneven deposition on top of the pores which lead to quick dendritic growth.

APPENDIX C

Supplementary Data for Chapter 4: Studying the CO2RR products and selectivity of mesoporous Cu with varying surface area and bimetallic surface coating

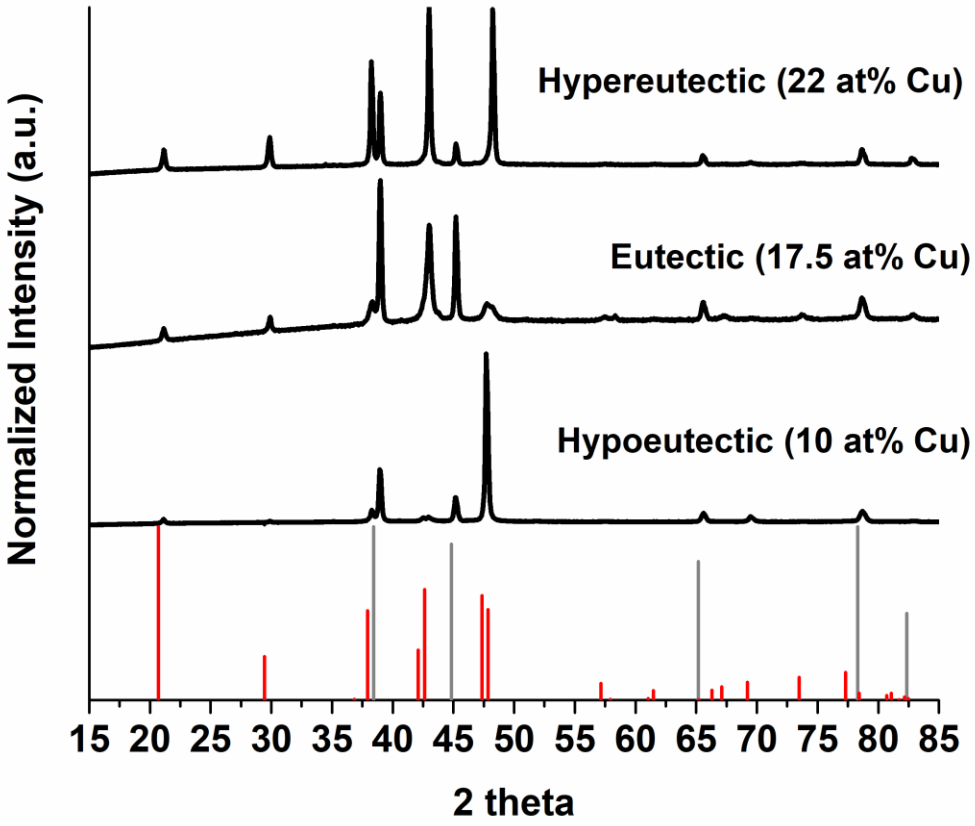

Figure S1. X-ray diffraction patterns of as-made Cu-Al alloys with hypoeutectic (10at%Cu), eutectic (17.5at%Cu) and hypereutectic (22at%Cu) compositions. $CuAl_2$ (red, JCPDS 03-065-2695) and Al (gray, JCPDS 00-001-1176) reference patterns are included for phase identification.

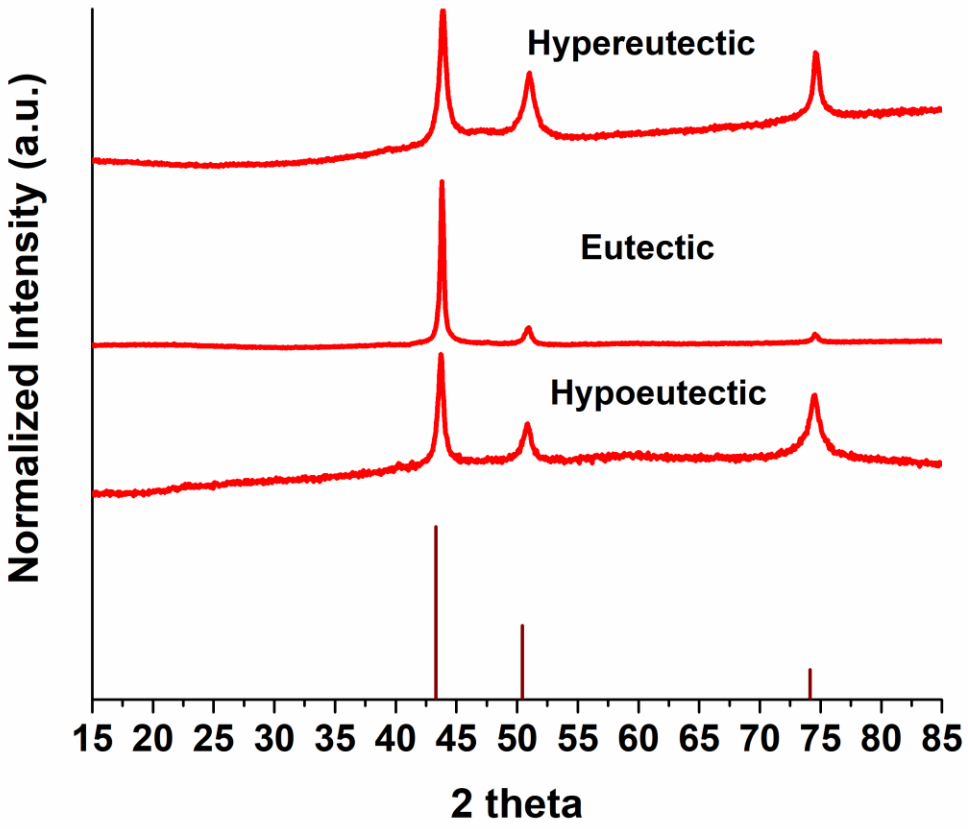

Figure S2. X-ray diffraction patterns of dealloyed Cu for hypoeutectic-derived Cu, eutectic-derived Cu and hypereutectic-derived Cu. Cu (JCPDS 01-078-2076) reference pattern is included for metal identification.

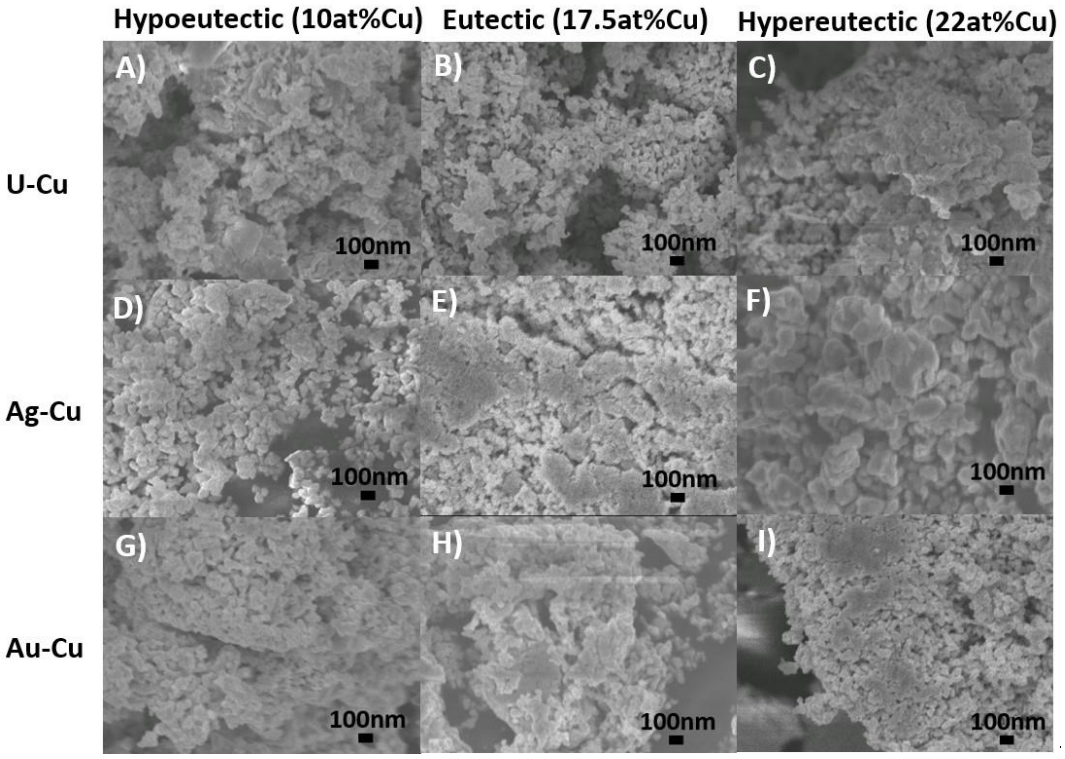

Figure S3. SEM images for uncoated (A) hypoeutectic, (B) eutectic and (C) hypereutectic powdered samples. Also shown are the same samples after coating with Ag (D-F) or with Au (G-I)

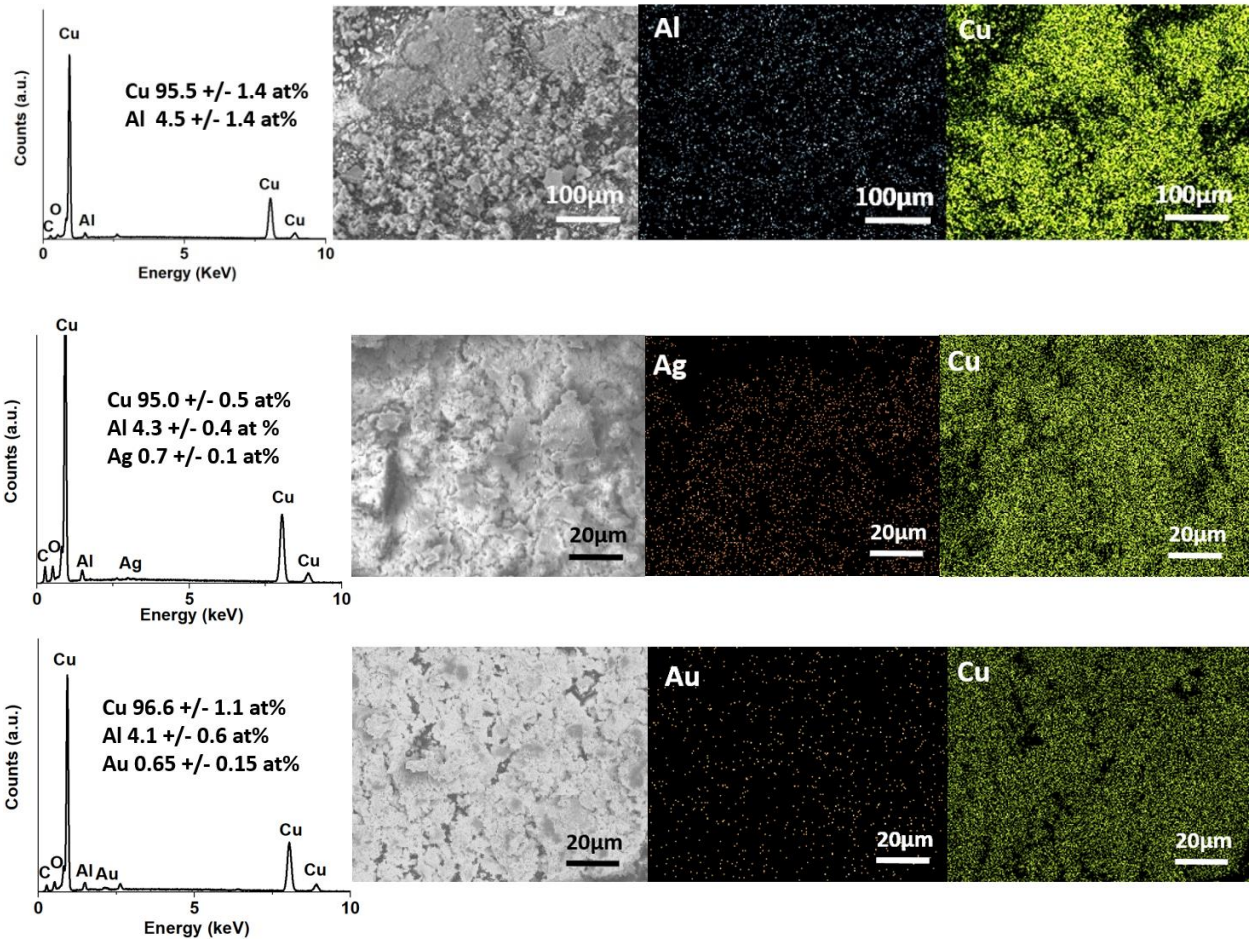

Figure S4. EDS spectrum, image and chemical mapping for (top row) uncoated hypoeutectic Cu, (middle row) Ag-coated hypoeutectic Cu and (bottom-row) Au-coated hypoeutectic Cu. Each row shows the EDX mapping, elemental composition, microstructure and elemental mapping.

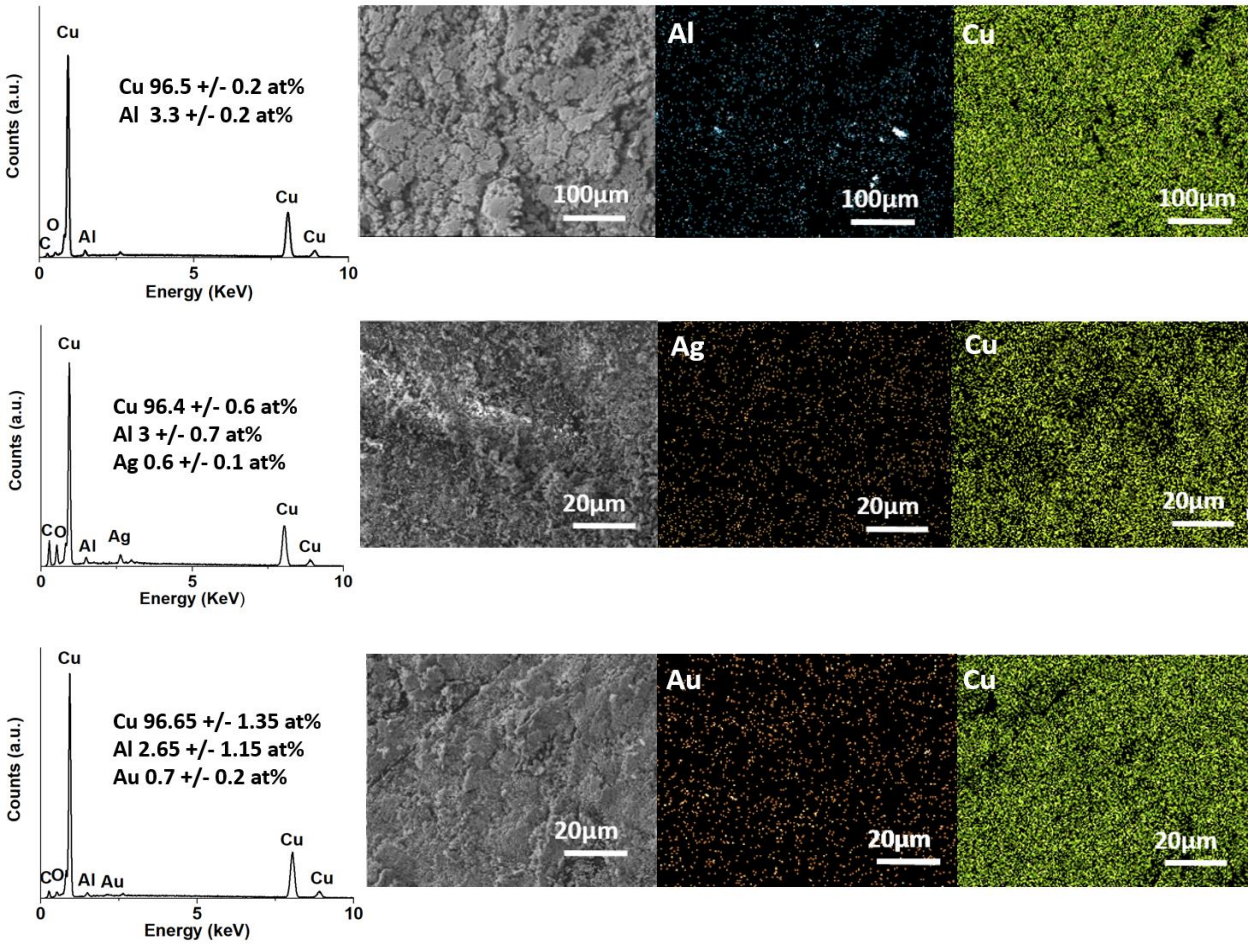

Figure S5. EDS spectrum, image and chemical mapping for (top row) uncoated eutectic Cu, (middle row) Ag-coated eutectic Cu and (bottom-row) Au-coated eutectic Cu. Each row shows the EDX mapping, elemental composition, microstructure and elemental mapping.

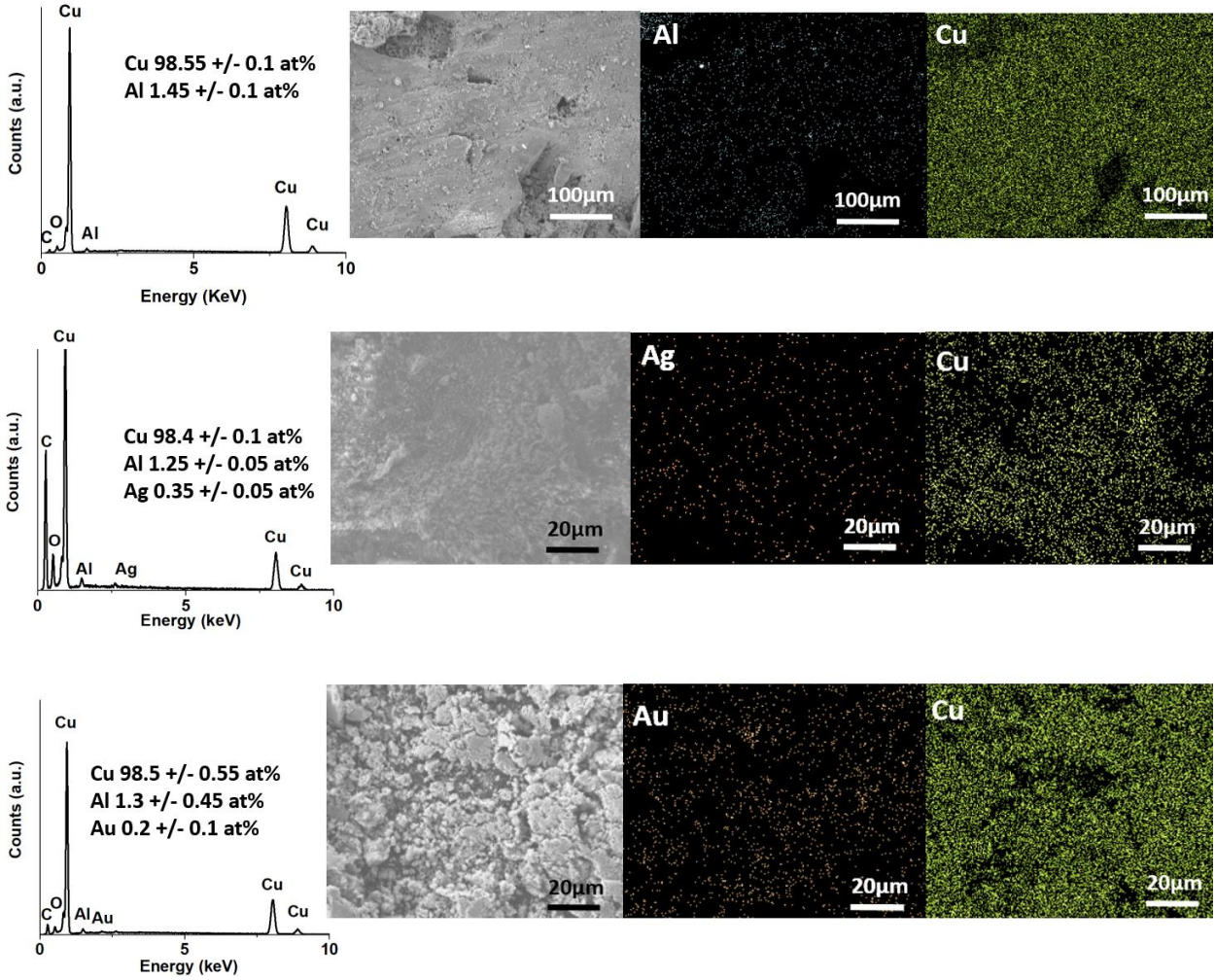

Figure S6. EDS spectrum, image and chemical mapping for (top row) uncoated hypereutectic Cu, (middle row) Ag-coated hypereutectic Cu and (bottom-row) Au-coated hypereutectic Cu. Each row shows the EDX mapping, elemental composition, microstructure and elemental mapping.

Table S1: EDS elemental composition extracted from the EDS mapping from Figs. S3-S5 for each of the nine samples used. There is a decreasing trend in Al and Ag content going from the hypoeutectic samples down the hypereutectic samples. The error corresponds to one standard deviation for a set of at least 2 separate measurements.

EDX-Composition	Cu at%	Al at%	Ag at%	Au at%
U-Hypo-Cu	95.5 +/- 1.4	4.5 +/- 1.4		
Ag-Hypo-Cu	95.0 +/-0.5	4.3 +/- 0.4	0.7 +/- 0.1	
Au-Hypo-Cu	95.6 +/- 1.1	4.1 +/- 0.6		0.65 +/- 0.15
U-E-Cu	96.5 +/- 0.2	3.3 +/- 0.2		
Ag-E-Cu	96.4 +/- 0.6	3 +/- 0.7	0.6 +/- 0.1	
Au-E-Cu	96.65 +/- 1.35	2.65 +/- 1.15		0.7 +/- 0.2
U-Hyper-Cu	98.55 +/- 0.1	1.45 +/- 0.1		
Ag-Hyper-Cu	98.4 +/- 0.1	1.25 +/- 0.05	0.35 +/- 0.05	
Au-Hyper-Cu	98.5 +/- 0.55	1.3 +/- 0.45		0.2 +/- 0.1

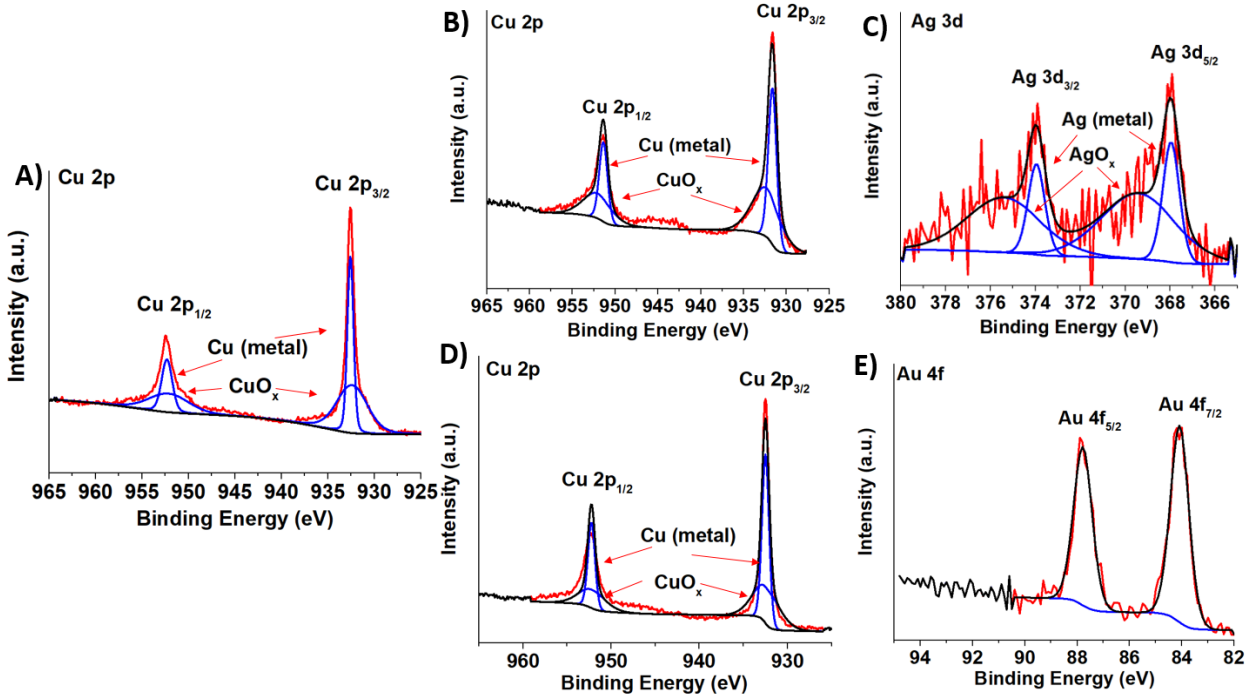

Figure S7. (A) Shows XPS of the Cu 2p core level signals for the uncoated hypoeutectic sample. (B) Shows the XPS of the Cu 2p and the Ag 3d core level signals for the Ag-coated hypoeutectic sample. (C) Shows the XPS of the Cu 2p and Au 4f core level signals for the Au-coated hypoeutectic sample. For each spectrum, the red line represents raw measured data and the blue lines represents fitted curves.

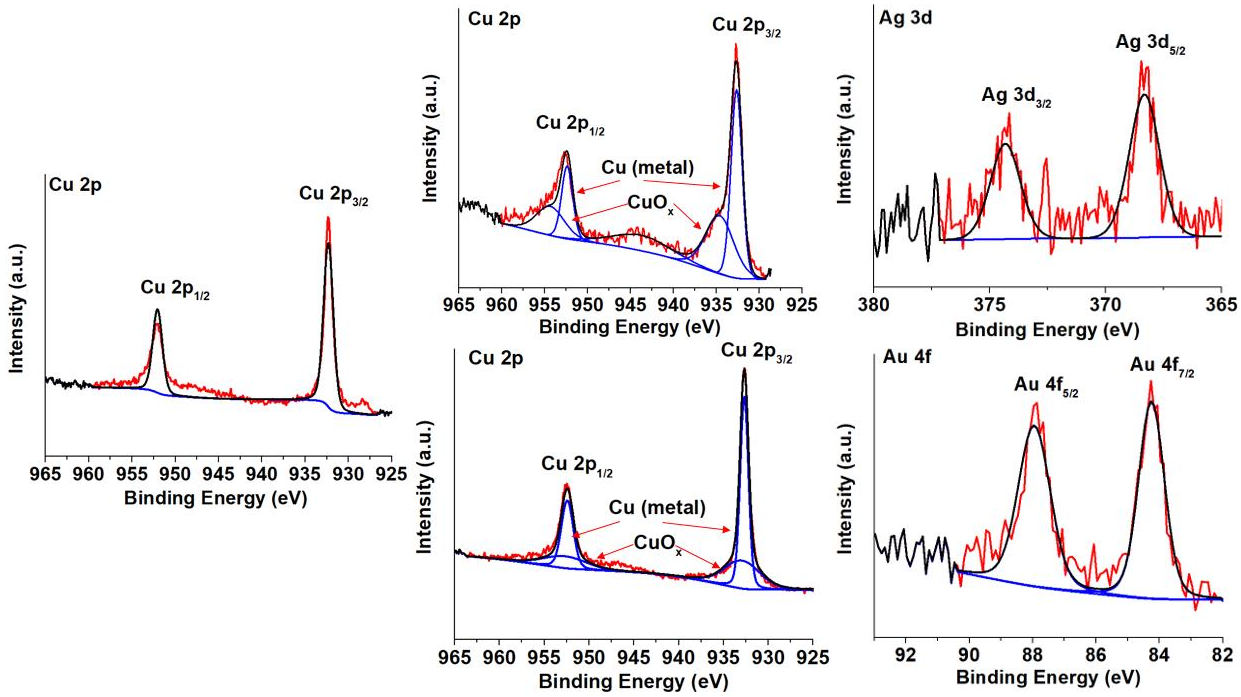

Figure S8. (A) Shows XPS of the Cu 2p core level signals for the uncoated eutectic sample. (B) Shows the XPS of the Cu 2p and the Ag 3d core level signals for the Ag-coated eutectic sample. (C) Shows the XPS of the Cu 2p and Au 4f core level signals for the Au-coated eutectic sample. For each spectrum, the red line represents raw measured data and the blue lines represents fitted curves.

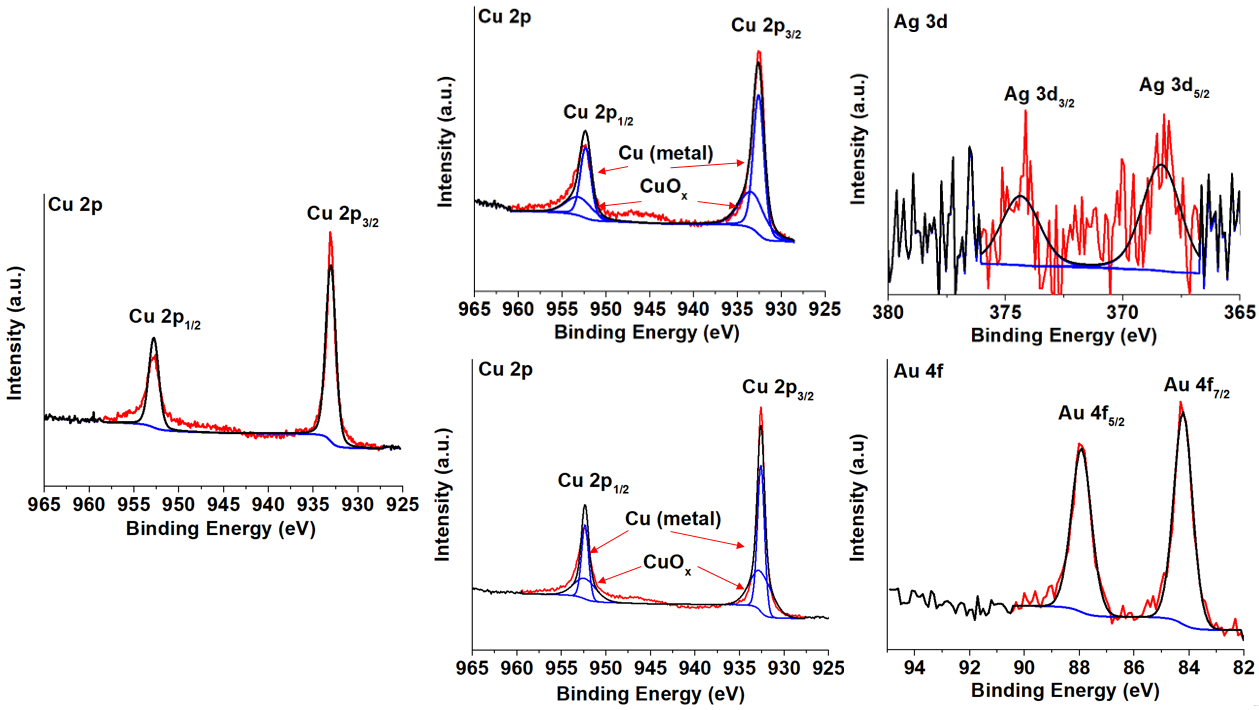

Figure S9. (A) Shows XPS of the Cu 2p core level signals for the uncoated hypereutectic sample. (B) Shows the XPS of the Cu 2p and the Ag 3d core level signals for the Ag-coated hypereutectic sample. (C) Shows the XPS of the Cu 2p and Au 4f core level signals for the Au-coated hypereutectic sample. For each spectrum, the red line represents raw measured data and the blue lines represents fitted curves.

Table S2: XPS peak position for different uncoated and coated porous powdered Cu samples

XPS Peak Positions	Cu $2p_{3/2}$ (eV)	Cu $2p_{1/2}$ (eV)	Ag $3d_{5/2}$ (eV)	Ag $3d_{3/2}$ (eV)	Au $4f_{7/2}$ (eV)	Au $4f_{5/2}$ (eV)
U-Hypo-Cu	932.5	952.3				
Ag-Hypo-Cu	931.6	951.4	367.9	373.9		
Au-Hypo-Cu	932.5	952.3			84.1	87.8
U-E-Cu	932.3	952.0				
Ag-E-Cu	932.7	952.5	368.3	374.3		
Au-E-Cu	932.7	952.5			84.3	88.0
U-Hyper-Cu	933.0	952.8				
Ag-Hyper-Cu	932.6	952.3	368.3	374.3		
Au-Hyper-Cu	932.6	952.4			84.2	87.9

Table S3: XPS peak ratio obtained from Cu2p, Ag 3d and Au4f core level signal peaks from Figs. S6-S8.

XPS-Peak Ratios	Cu (%)	Ag (%)	Au (%)
Ag-Hypoeutectic	99	1	
Au-Hypoeutectic	98.75		1.25
Ag-Eutectic	99.3	0.7	
Au-Eutectic	98.24		1.76
Ag-Hypereutectic	99.24	0.76	
Au-Hypereutectic	98.67		1.33

Table S4: Surface area measurements of three different batches for the uncoated samples and of two different batches for the coated samples. Average surface area measurement, standard deviation, standard error of the mean (SEM) and error of the mean (2xSEM) are calculated and included in this table. The units of all numbers are m^2/g.

Surface Area Measurements	U-Hypo-Cu	U-E-Cu	U-Hyper-Cu	Ag-Hypo-Cu	Ag-E-Cu	Ag-Hyper-Cu	Au-Hypo-Cu	Au-E-Cu	Au-Hyper-Cu
Trial 1	2.0	7.3	5.3	8.8	6.4	7.8	5.4	7.6	8.8
Trial 2	4.0	7.0	8.38	14.1	7.8	7.6	10.1	6.9	10.4
Trial 3	2.5	5.9	14.7						
Average	**2.8**	**6.8**	**9.5**	**11.4**	**7.1**	**7.7**	**7.8**	**7.2**	**9.6**
Std. Dev.	1.0	0.8	4.8	3.7	1.0	0.2	3.3	0.5	1.1
SEM	0.6	0.4	2.8	2.2	0.6	0.1	1.9	0.3	0.6
Error of the mean	**1.2**	**0.9**	**5.5**	**4.3**	**1.1**	**0.2**	**3.8**	**0.5**	**1.3**

Table S5: Average pore size obtained from the differential dV/dW pore size distribution plots (D, E and F in Fig. 4) from N_2 porosimetry measurements of the nine samples used in this work.

	U-Hypo-Cu	U-E-Cu	U-Hyper-Cu	Ag-Hypo-Cu	Ag-E-Cu	Ag-Hyper-Cu	Au-Hypo-Cu	Au-E-Cu	Au-Hyper-Cu
Avg. Pore Size	**57.4 nm**	**46.9 nm**	**13.1 nm**	**61.4 nm**	**54.2 nm**	**25.5 nm**	**68.7 nm**	**45.5 nm**	**30.9 nm**

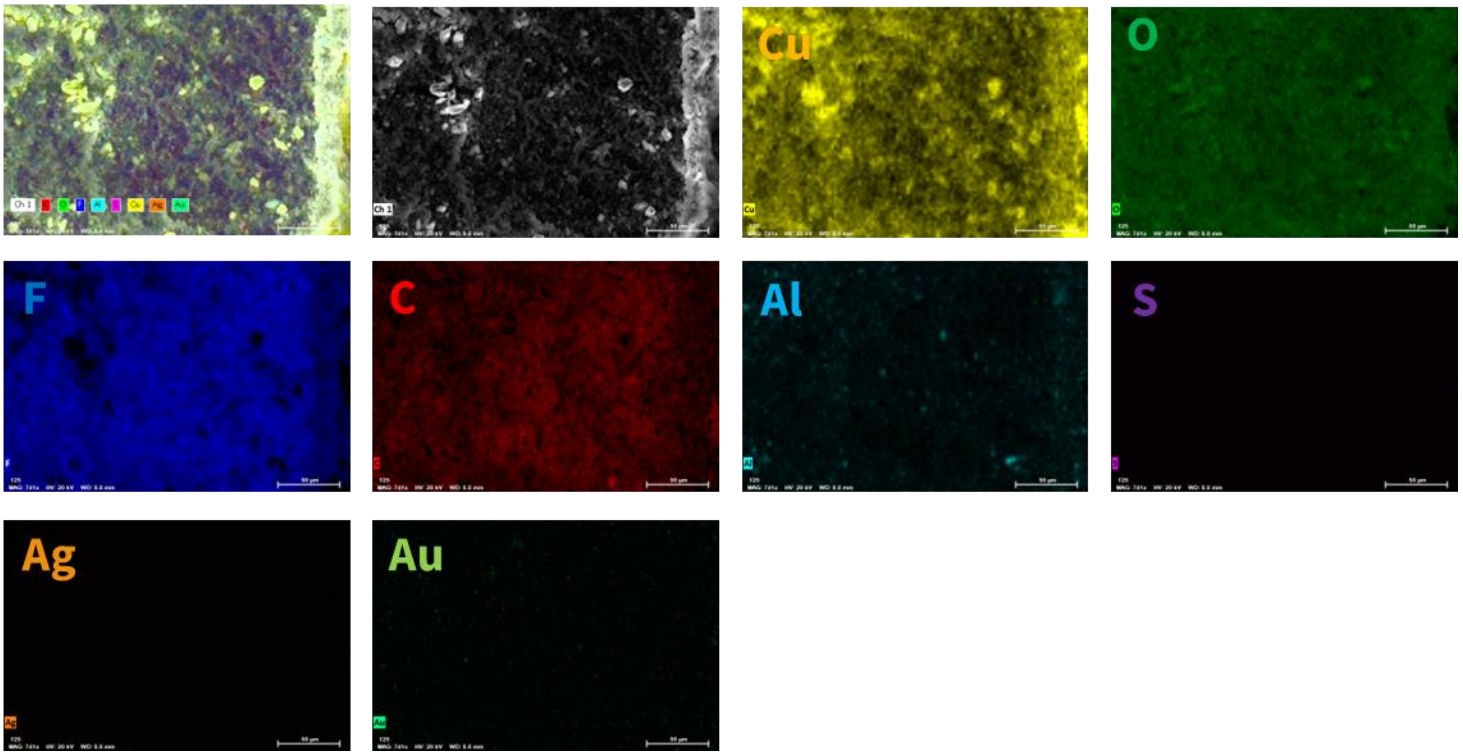

Figure S10. SEM-EDS images for the uncoated hypoeutectic sample integrated into gas diffusion electrode.

Table S6: Quantified elemental composition for the uncoated hypoeutectic sample integrated into gas diffusion electrode.

Element	Atom [%]	Rel. Error [%, 1 sigma]
Fluorine	35.53	4.7
Copper	8.97	1.3
Oxygen	30.75	5.4
Carbon	21.55	4.9
Aluminum	2.84	3.2
Sulfur	0.35	2.4
Silver	0.00	999.0
Gold	0.00	999.0

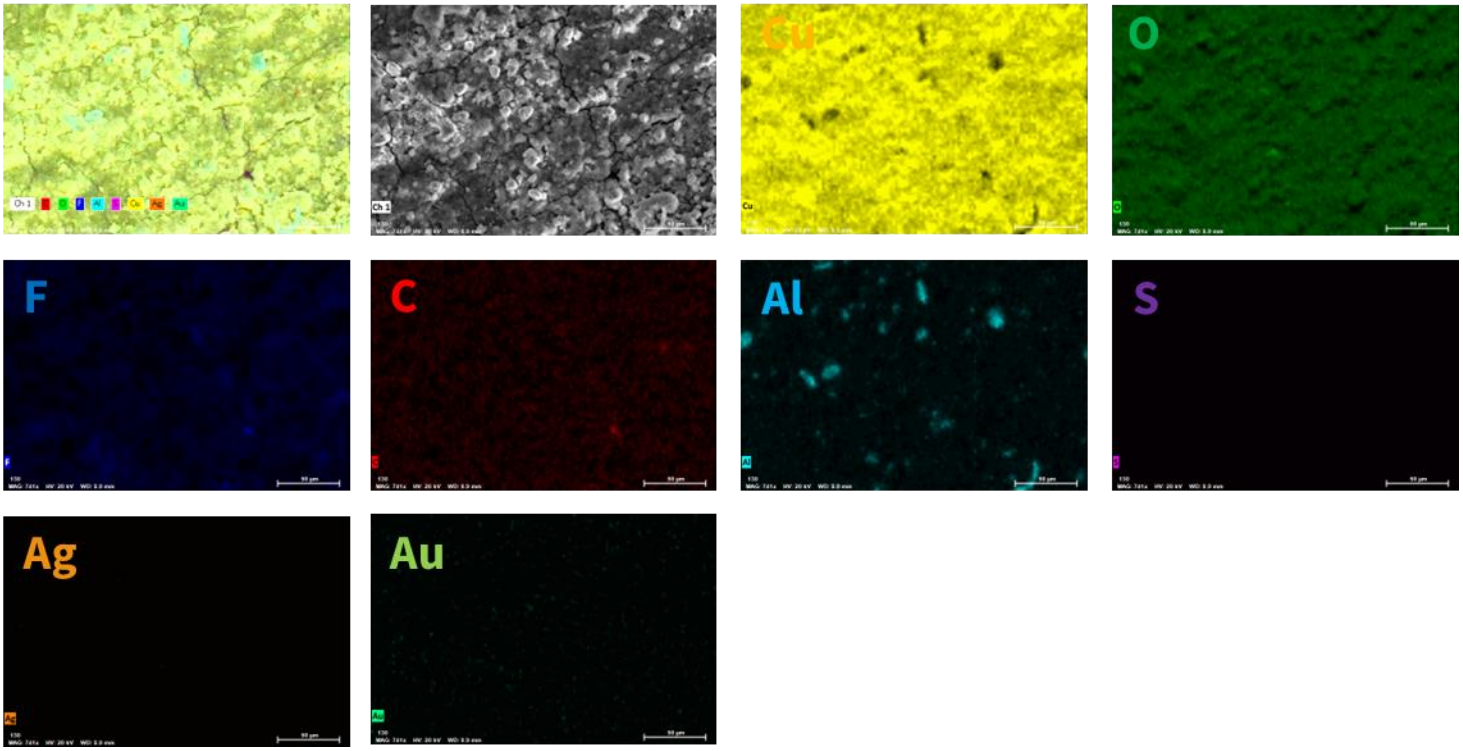

Figure S11. SEM-EDS images for the uncoated eutectic sample integrated into gas diffusion electrode.

Table S7: Quantified elemental composition for the uncoated eutectic sample integrated into gas diffusion electrode.

Element	Atom [%]	Rel. Error [%, 1 sigma]
Copper	26.76	1.1
Oxygen	34.31	4.8
Fluorine	13.82	4.9
Carbon	20.23	5.6
Aluminum	4.60	3.2
Sulfur	0.28	2.9
Gold	0.01	42.2
Silver	0	999

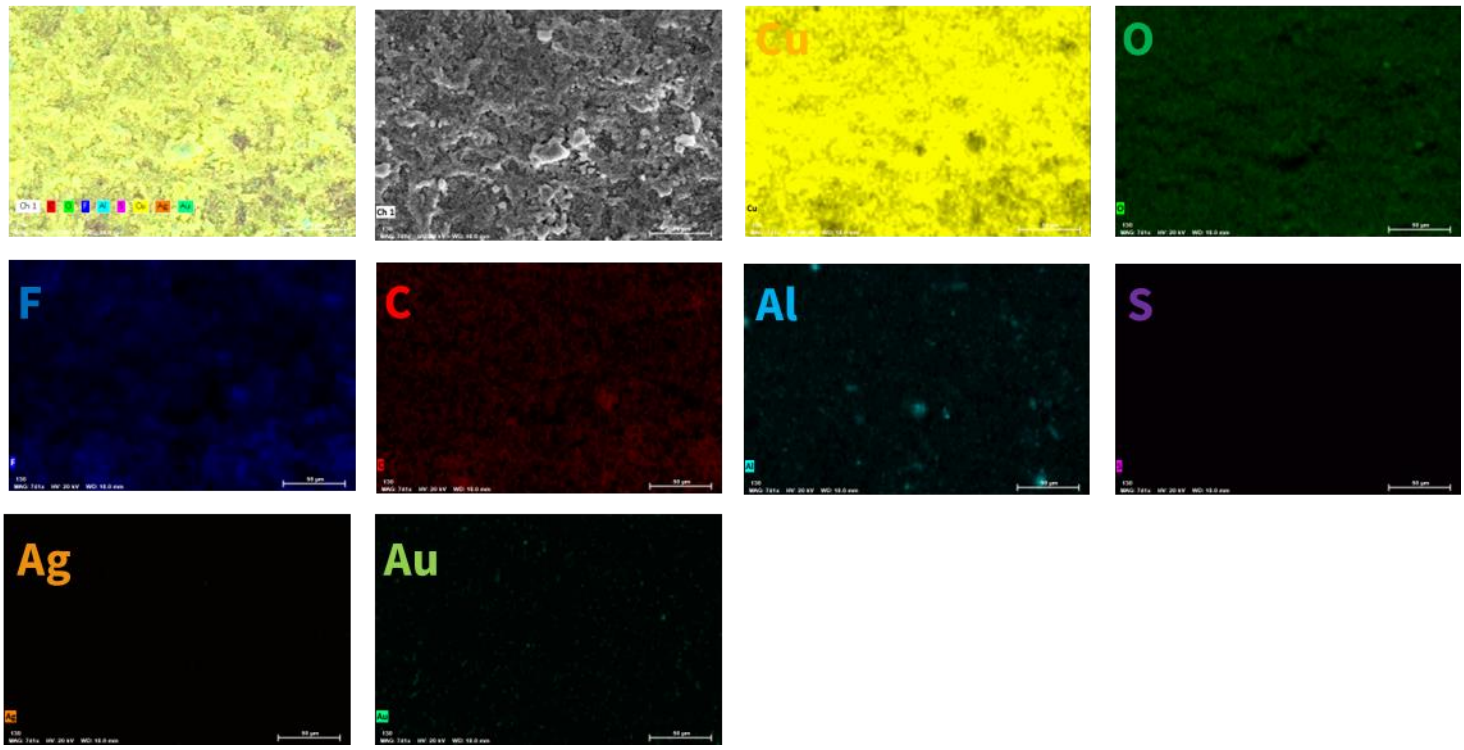

Figure S12. SEM-EDS images for the uncoated hypereutectic sample integrated into gas diffusion electrode.

Table S8: Quantified elemental composition for the uncoated hypereutectic sample integrated into gas diffusion electrode.

Element	Atom [%]	Rel. Error [%, 1 sigma]
Copper	32.55	1.1
Oxygen	21.14	5.0
Fluorine	17.02	4.6
Carbon	24.57	5.6
Aluminum	4.56	3.2
Sulfur	0.16	4.1
Silver	0.00	42.3
Gold	0	999

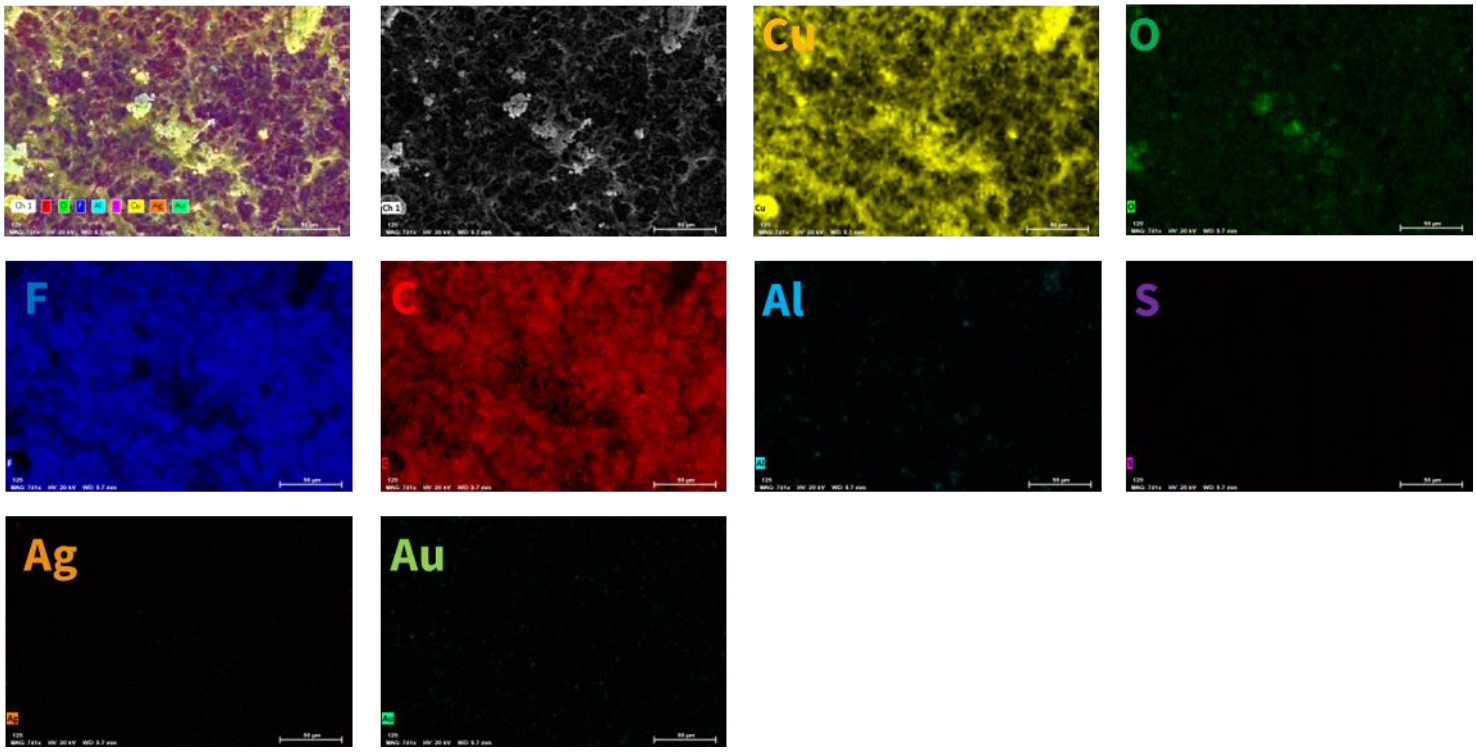

Figure S13. SEM-EDS images for the Ag-coated hypoeutectic sample integrated into gas diffusion electrode.

Table S9: Quantified elemental composition for the Ag-coated hypoeutectic sample integrated into gas diffusion electrode.

Element	Atom [%]	Rel. Error [%, 1 sigma]
Fluorine	33.56	4.7
Carbon	49.73	5.2
Copper	8.11	1.3
Oxygen	7.84	5.0
Aluminum	0.54	3.5
Silver	0.11	2.4
Sulfur	0.11	3.4
Gold	0.00	999.0

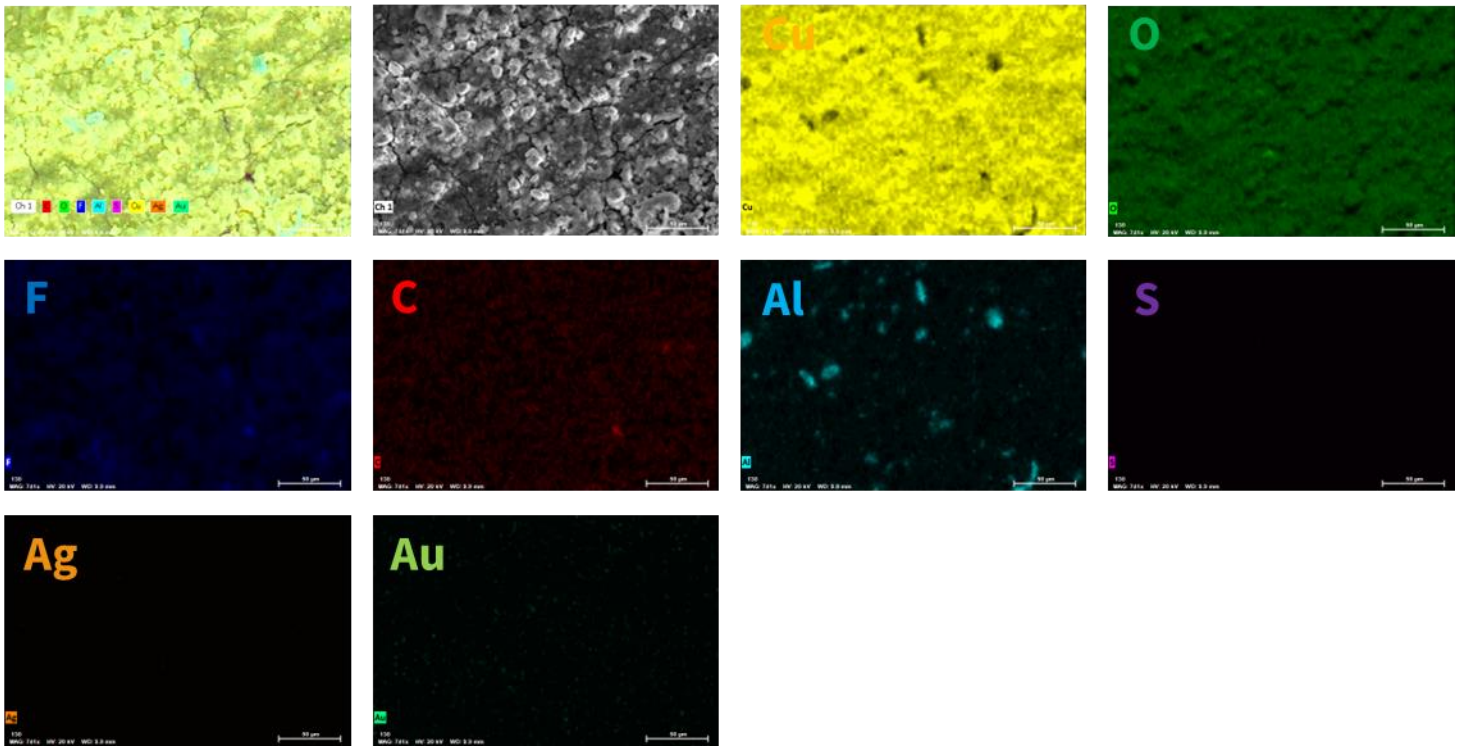

Figure S14. SEM-EDS images for the Ag-coated eutectic sample integrated into gas diffusion electrode.

Table S10: Quantified elemental composition for the Ag-coated eutectic sample integrated into gas diffusion electrode.

Element	Atom [%]	Rel. Error [%, 1 sigma]
Copper	31.30	1.1
Fluorine	23.20	4.7
Carbon	26.31	5.4
Oxygen	15.23	4.9
Silver	0.88	1.7
Aluminum	2.42	3.3
Sulfur	0.66	2.5
Gold	0	999

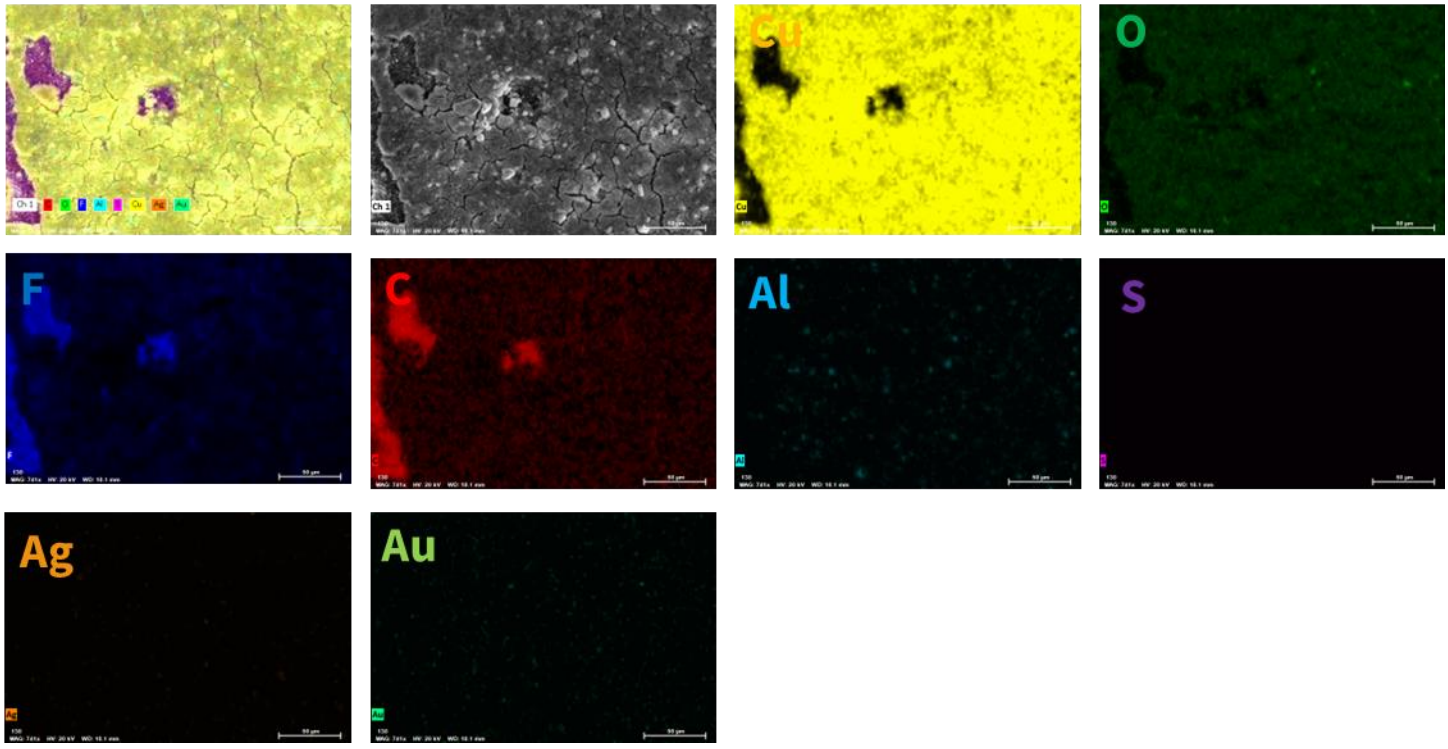

Figure S15. SEM-EDS images for the Ag-coated hypereutectic sample integrated into gas diffusion electrode.

Table S11: Quantified elemental composition for the Ag-coated hypereutectic sample integrated into gas diffusion electrode.

Element	Atom [%]	Rel. Error [%, 1 sigma]
Copper	28.26	1.1
Carbon	33.88	5.4
Fluorine	16.24	4.8
Oxygen	19.27	4.9
Silver	0.47	1.8
Aluminum	1.68	3.3
Sulfur	0.19	3.4
Gold	0.01	60.1

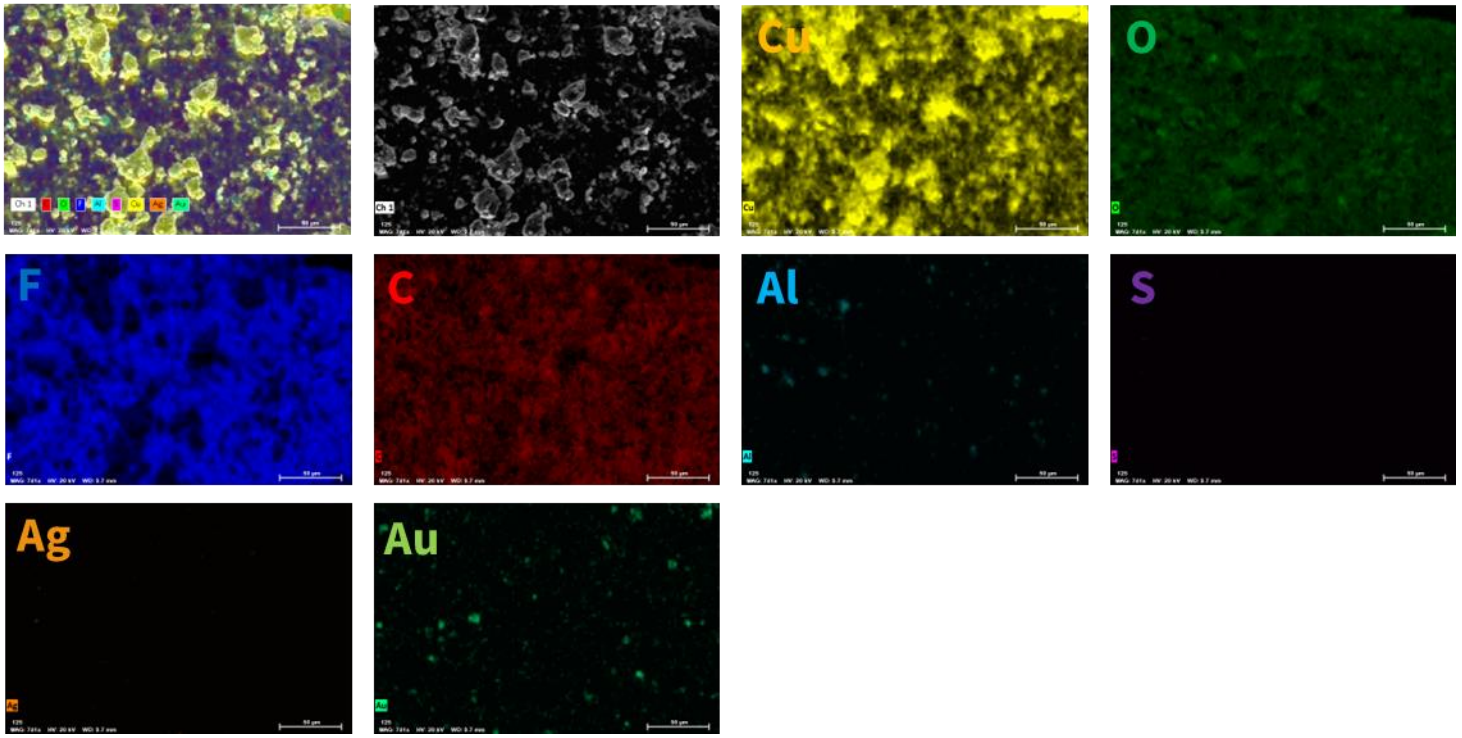

Figure S16. SEM-EDS images for the Au-coated hypoeutectic sample integrated into gas diffusion electrode.

Table S12: Quantified elemental composition for the Au-coated hypoeutectic sample integrated into gas diffusion electrode.

Element	Atom [%]	Rel. Error [%, 1 sigma]
Fluorine	39.88	4.7
Copper	10.42	1.3
Carbon	32.34	5.4
Oxygen	16.18	4.8
Gold	0.13	3.5
Aluminum	0.74	3.5
Sulfur	0.32	2.6
Silver	0	999

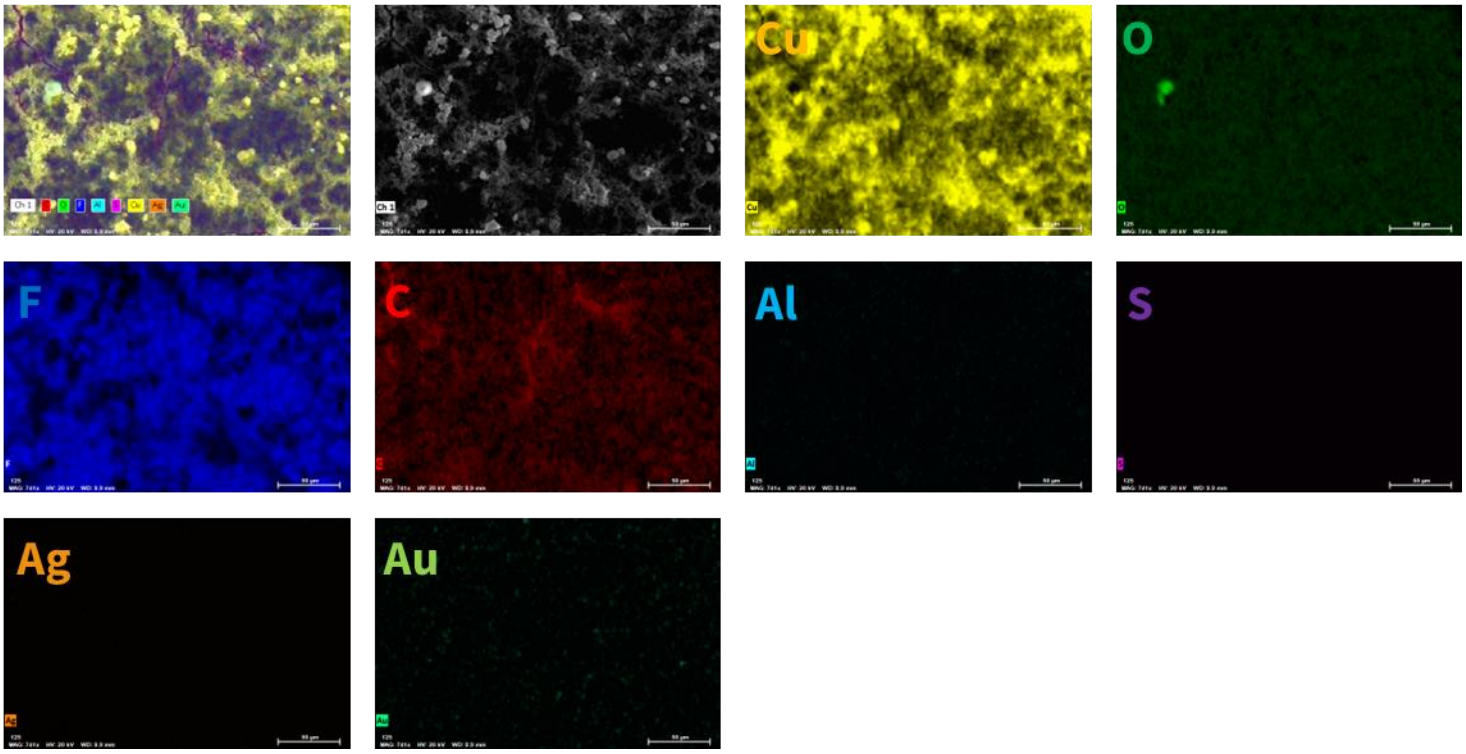

Figure S17. SEM-EDS images for the Au-coated eutectic sample integrated into gas diffusion electrode.

Table S13: Quantified elemental composition for the Au-coated eutectic sample integrated into gas diffusion electrode.

Element	Atom [%]	Rel. Error [%, 1 sigma]
Copper	13.46	1.2
Fluorine	42.42	4.6
Carbon	29.48	5.4
Oxygen	13.25	5.0
Aluminum	0.88	3.4
Sulfur	0.44	2.4
Gold	0.06	6.6
Silver	0.00	999.0

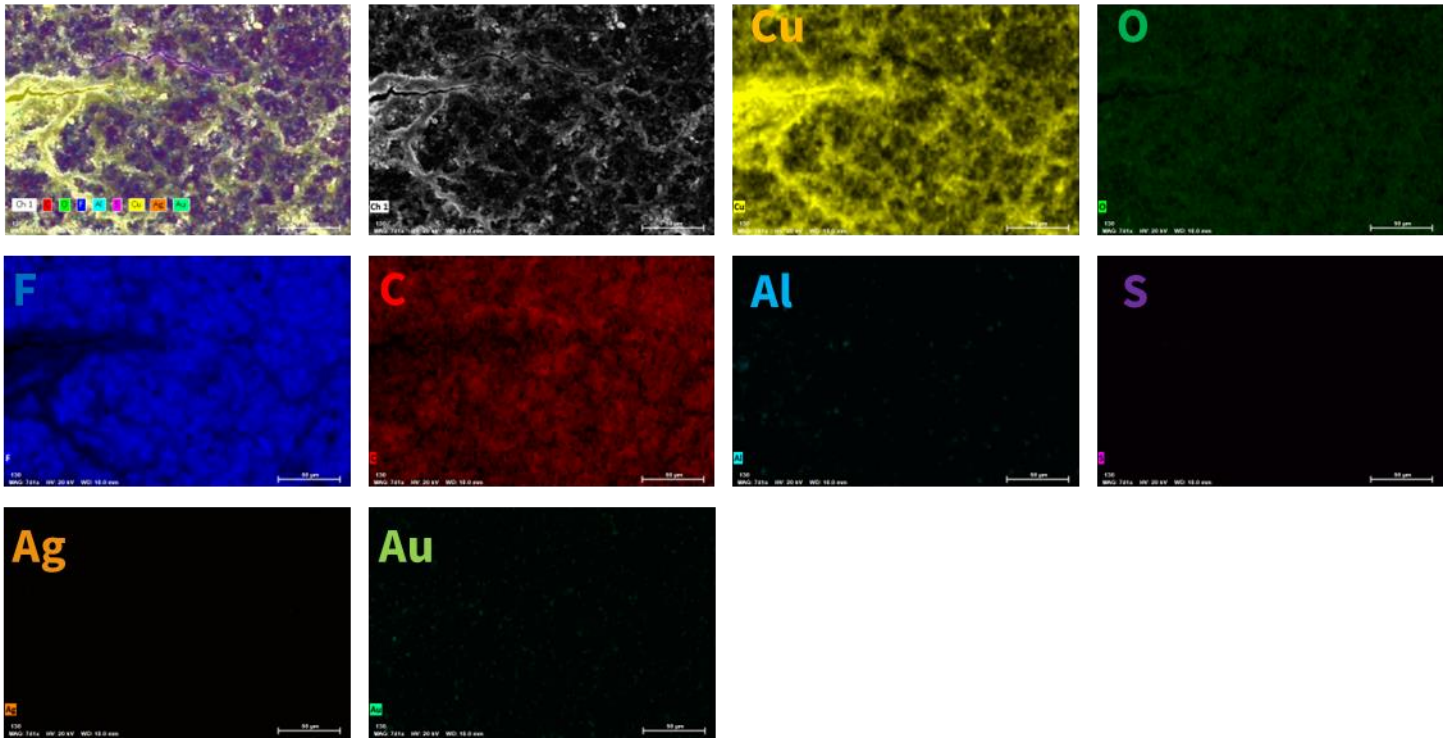

Figure S18. SEM-EDS images for the Au-coated hypereutectic sample integrated into gas diffusion electrode.

Table S14: Quantified elemental composition for the Au-coated hypereutectic sample integrated into gas diffusion electrode.

Element	Atom [%]	Rel. Error [%, 1 sigma]
Fluorine	41.71	4.7
Copper	9.59	1.3
Carbon	36.32	5.3
Oxygen	11.48	5.0
Aluminum	0.61	4.0
Sulfur	0.28	2.9
Gold	0.01	66.8
Silver	0.00	999.0

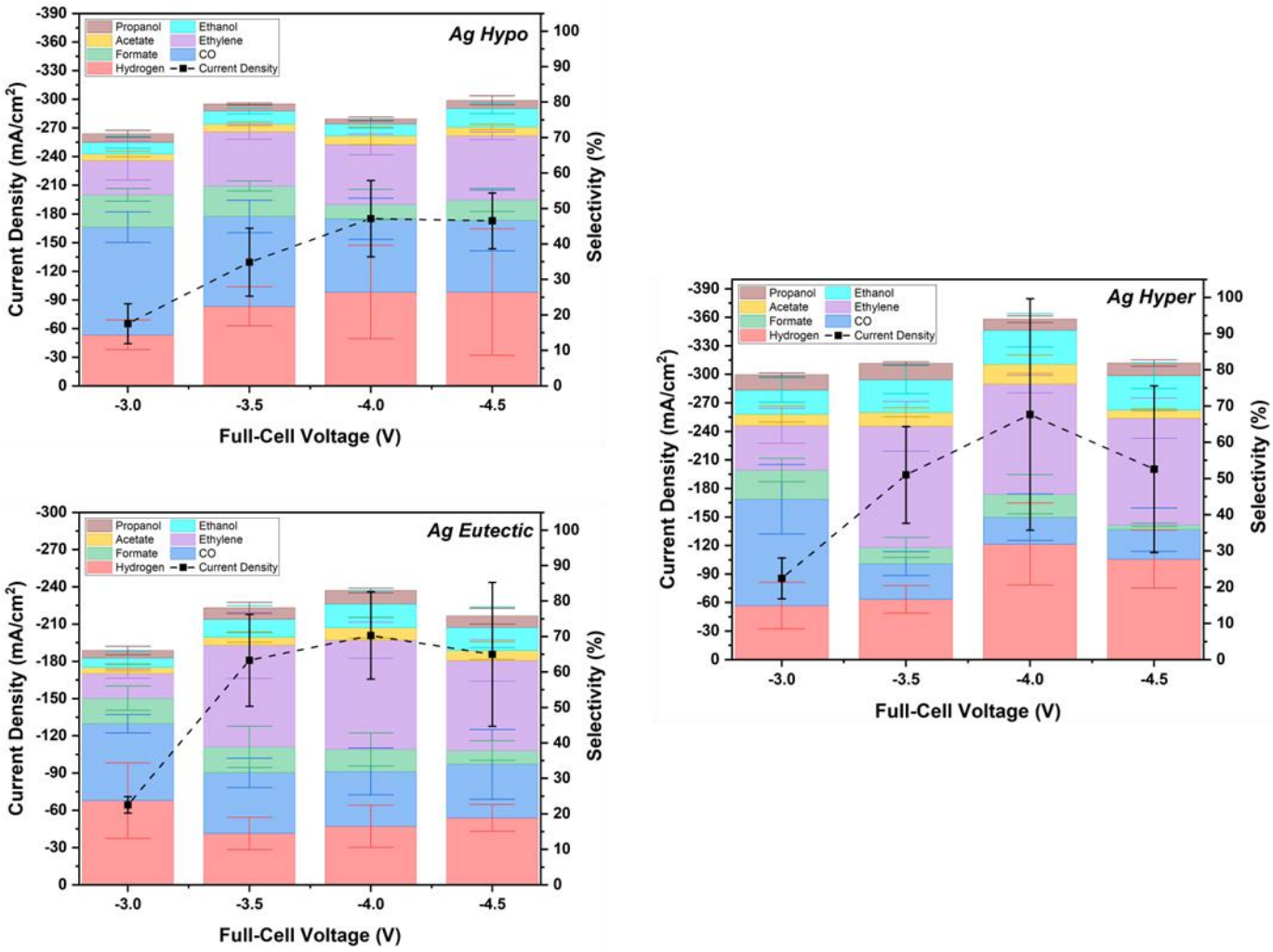

Figure S19. Measured selectivity and current density of different CO_2 reduction products for Ag-coated Cu samples impregnated in gas diffusion electrodes using a membrane electrode assembly (MEA) electrolyzer. Error bars indicate the result of triplicate experiments.

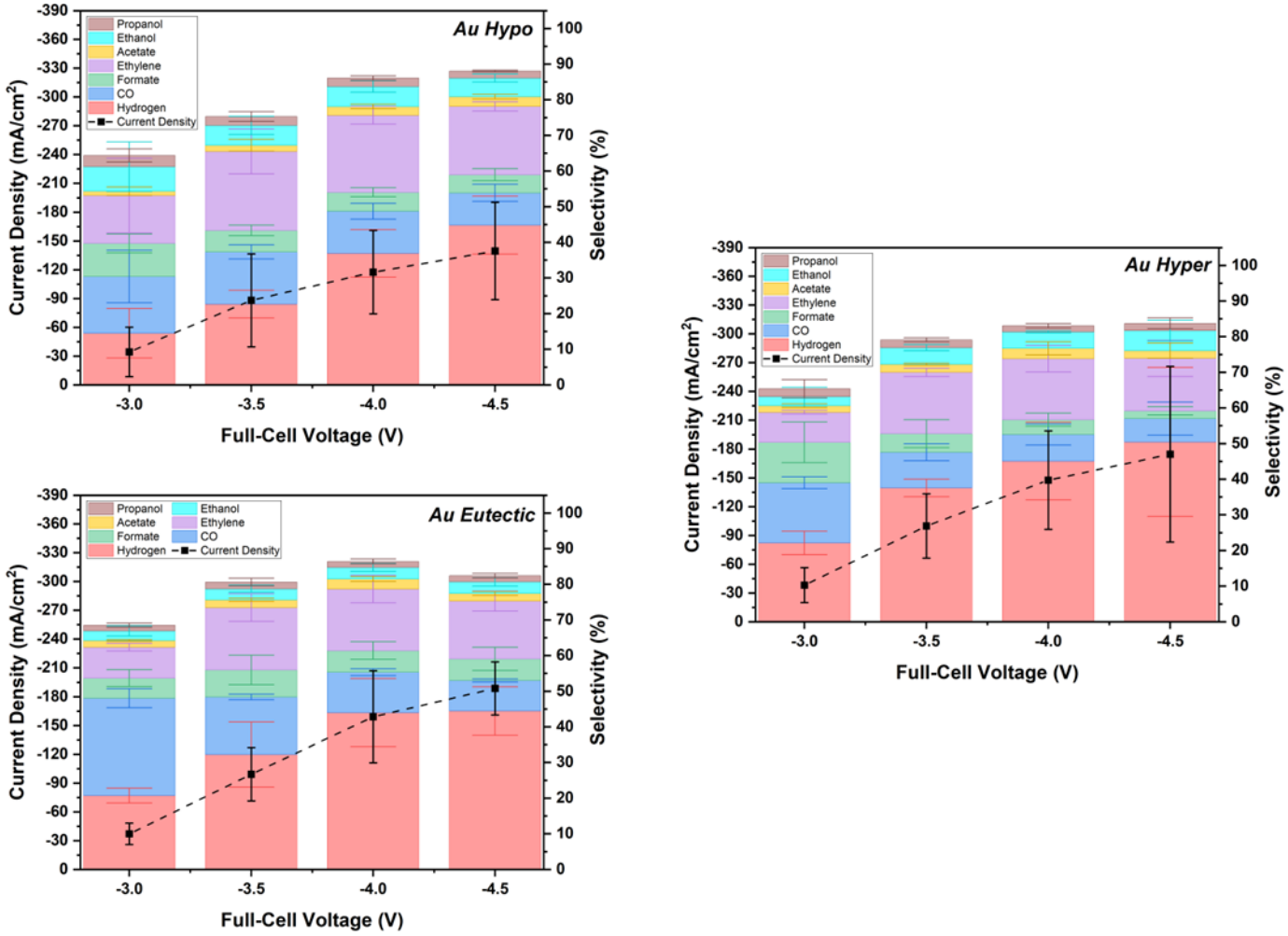

Figure S20. Measured selectivity and current density of different CO_2 reduction products for Au-coated Cu samples impregnated in gas diffusion electrodes using a membrane electrode assembly (MEA) electrolyzer. Error bars indicate the result of triplicate experiments.